Soft and Accurate Norm Conserving Pseudopotentials and their Application for Structure Prediction

Inauguraldissertation
zur
Erlangung der Würde eines Doktors der Philosophie
vorgelegt der
Philosophisch-Naturwissenschaftlichen Fakultät
der Universität Basel

von

Santanu Saha
aus Indien

Basel, 2017

Genehmigt von der Philosophisch-Naturwissenschaftlichen Fakultät

auf Antrag von:

Prof. Dr. Stefan Goedecker

Prof. Dr. Joost VandeVondele

Basel, 21. March 2017

Prof. Dr. Martin Spiess
Dekan

To my family

Acknowledgements

First of all I would like to thank my supervisor Prof. Dr. Stefan Goedecker for giving me the opportunity to work in this exciting field of computational physics. I am grateful to him for providing a pleasant environment for work through constant encouragement, support and guidance. I have learned a lot from him, particularly his simplistic approach to problems. I would also like to thank Prof. Dr. Joost VandeVondele for accepting to be the co-referee of this thesis.

Furthermore, I would also like to thank Dr. Luigi Genovese for providing instant solutions related to the problems of BigDFT without which a part of my thesis work would not have been possible. I am thankful to Barbara Kammermann and Astrid Kalt, the secretaries of the Physics Department, for providing kind support.

I would like to thank Migle, Bastian and Daniele for proof reading my thesis and providing valuable suggestion. I am thankful to José and Deb for intriguing discussions. I would like to thank all of my friends and colleagues for making my stay in Basel memorable.

I am thankful to my teachers and professors for inspiring and motivating me to pursue my interest. Finally, I would like to thank my parents, my brother Aion and Dipanwita Ghanti for their love and support.

Abstract

Structure prediction and discovery of new materials are essential for the advancement of new technologies. This have been possible due to the developments in Density Functional Theory (DFT) and increase in computational power of the supercomputers. One of the key aspect is the reliability of the structures predicted by the DFT codes. In this regard pseudopotentials are essential for both fast and accurate predictions. Through the addition of softness constraints on the pseudo valence orbitals along with the non-linear core correction and semicore states, new soft and accurate dual space Gaussian type pseudopotentials have been generated for the Perdew Burke Ernzerhof (PBE) and PBE0 functionals. Despite being soft, these pseudopotentials were able to achieve chemical accuracy necessary for the production runs. These pseudopotentials have been benchmarked against the most accurate all-electron (μHa accuracy) reference data of molecular systems till date which has been obtained using the Multi-Wavelets as implemented in the MRCHEM. In addition the pseudopotentials for the PBE functional show remarkable accuracy in the Delta tests. These new soft and accurate pseudopotentials have been used for structure prediction of large clusters.

Contents

1 Density Functional Theory - Basic Outline

With the fast development of hardware infrastructure in the last few decades, Density Functional Theory (DFT) has become an essential tool in the study of condensed matter systems. DFT provides the framework via which the laws of quantum mechanics can be used to study electronic and structural properties of a real large system instead of toy models in an efficient way. In order to understand the basic formalism of DFT, lets try to understand the basic principles arising from the Schrödinger equation.

Consider a system consisting of N atoms which have m electrons. There exists 3N ($\mathbf{R_1}, ..., \mathbf{R_N}$) variables for the nuclei and 3m ($\mathbf{r_1}, ..., \mathbf{r_m}$) variables for the electrons. The Schrödinger equation provides a quantum mechanical description of the system where the wave function is dependent on the 3N and 3m variables. However, according to the Born Oppenheimer [1] approximation the wave function can be written as a product of two terms (1.1) where the first term is a function of nuclei coordinates and the second term of electronic coordinates.

$$\Psi_{total}(\mathbf{r},\mathbf{R}) = \Psi_{nuclear}(\mathbf{R})\Psi_{electronic}(\mathbf{r}) \tag{1.1}$$

$$H\Psi_{total} = \Big\{H_n\Psi_{nuclear}(\mathbf{R})\Big\}\Psi_{electronic}(\mathbf{r}) + \Big\{H_e\Psi_{electronic}(\mathbf{r})\Big\}\Psi_{nuclear}(\mathbf{R}) \tag{1.2}$$

$$H_n\Psi_{nuclear}(\mathbf{R}) = -\sum_{i=1}^{N}\frac{1}{2M_A}\nabla_i^2\Psi_{nuclear}(\mathbf{R}) \tag{1.3}$$

$$H_e\Psi_{electronic}(\mathbf{r}) = \Big\{-\sum_{i}^{m}\frac{1}{2}\nabla_i^2 + \frac{1}{2}\sum_{i<j}^{m}\frac{1}{|\mathbf{r}_i-\mathbf{r}_j|} - \sum_{i,A}^{m,N}\frac{Z_A}{|\mathbf{r}_i-\mathbf{R}_A|} + \sum_{A>B}^{N}\frac{Z_AZ_B}{|\mathbf{R}_A-\mathbf{R}_B|}\Big\}\Psi_{electronic}(\mathbf{r}) \tag{1.4}$$

Under this approximation, the Schrödinger equation can be split into two parts (1.2), i.e. the first part which has only the contribution from the nuclei (H_n) where M_A represents the mass of the nucleus in atomic units and the second part from the electrons (H_e) where Z_A and Z_B represents the nuclear charge of atom A and atom B. The nuclei part has only the contribution of kinetic energy (1.3) due to the nuclei. As the nuclei are much heavier than the electrons (by a factor of ~1000), the motion of the nuclei can be considered as static with respect to that of electrons. Hence, the nuclei part (H_n) can be removed from the Schrödinger equation and one is left with an electronic problem (1.4) where the coordinates of the nuclei act only as simple parameters.

This time independent Schrödinger equation is the starting point of most of the electronic structure calculations. The terms in eq. (1.4) represents the kinetic energy due to electrons, Coulombic repulsion between the electrons, nuclei-electron interaction and the nuclear-nuclear interaction respectively. Here in the above equation and in all future expressions, atomic units are used where the Planck's constant h, the charge of the electron e, the rest mass of electron m_e and the Coulomb force constant $1/4\pi\epsilon_0$ are set equal to 1.

Though eq. (1.4) looks very simplistic, an analytical solution has been found only for a few cases such as that of the hydrogen atom. Numerical methods can be used for its solution instead. But it is too expensive in practice and is strongly limited by the system size. As an alternative approach, DFT in particular the Kohn Sham (KS-DFT) formalism provides a simple, elegant and efficient solution to this problem. The KS-DFT is used in most of the electronic structure codes. In this chapter the origin of DFT, KS-DFT and incorporation of relativistic and spin polarized effects are discussed.

1.1 Pillars of Density Functional Theory

The pillars of DFT are the Hohenberg-Kohn [2] theorems. The first theorem states that the total energy of a system consisting of electrons in an external potential is uniquely defined by its charge density, i.e. the total energy is the functional of the charge density. The second theorem states that the true ground state density is the density which minimizes the total energy. The total energy for a system consisting of electrons in an external potential can be written as a sum of the energy arising from the electronic density and other external terms (1.5), where the second and third term represents the energy due to an external (nuclear) potential (1.6) and internuclear interactions (1.7). Here, the nuclei are assumed to be point charges.

$$E_{total} = E_e(\rho) + E_{ext}(\rho) + E_{n-n} \tag{1.5}$$

$$E_{ext}(\rho) = \sum_{A}^{N} \int \frac{\rho(\mathbf{r}) Z_A}{|\mathbf{r} - \mathbf{R}_A|} d^3\mathbf{r} \tag{1.6}$$

$$E_{n-n} = \sum_{A<B}^{N} \frac{Z_A Z_B}{|\mathbf{R_A} - \mathbf{R_B}|} d^3\mathbf{r} \tag{1.7}$$

In principle, the total energy can be minimized by variation of the charge density which would give the true ground state. But, the exact form of the energy functional on which the variational principle is to be applied is unknown. The Hohenberg-Kohn theorems do not provide any clue to this problem.

In practice the total energy is expressed as a sum of different contributions (1.8) with an additional term called the exchange correlation functional. Eq. (1.5) and (1.8) are similar except that in (1.8), $E_e(\rho)$ is split into a kinetic energy term and a Hartree term (1.9) and an exchange correlation term is added. The idea of introducing the exchange correlation term is to include additional unknown interaction terms which have not been accounted for in other terms.

$$E_{total} = \underbrace{E_{kin}(\rho) + E_H(\rho)}_{:=E_e(\rho)} + E_{ext}(\rho) + E_{n-n} + E_{xc}(\rho) \tag{1.8}$$

$$E_H(\rho) = \iint \frac{1}{2} \frac{\rho(\mathbf{r})\rho(\mathbf{r}')}{|\mathbf{r} - \mathbf{r}'|} d^3\mathbf{r} d^3\mathbf{r}' \tag{1.9}$$

1.2 Introduction to Kohn Sham Formalism of DFT

The wave function approach to the solution of the Schrödinger equation is computationally expensive and its application is strongly limited by the system size. The Kohn Sham(KS) [3] formalism of DFT evolved into state of the art method which could be applied to large system. In this approach the motion of correlated and interacting electrons under an external potential is modeled as fictitious non-interacting particles moving under an effective potential called the Kohn Sham potential. The eigensolutions of the Hamiltonian of this modeled system are known as the Kohn Sham orbitals which are orthonormal to each other. In this scheme the expression for energy remains the same as in eq. (1.8).

$$\rho(\mathbf{r}) = \sum_{occ} \phi_i^*(\mathbf{r})\phi_i(\mathbf{r}) \tag{1.10}$$

The electronic charge density (1.10) in KS-DFT is defined as the summation over the squares of the KS orbitals where the summation runs over all the occupied states. Here, $\phi_i(\mathbf{r})$ represents the KS orbital of the i^{th} eigenstate.

$$E_{kin} = -\frac{1}{2} \sum_{occ} \int \phi_i^*(\mathbf{r}) \nabla^2 \phi_i(\mathbf{r}) d^3\mathbf{r} \tag{1.11}$$

The kinetic energy is simply defined as the sum over all the kinetic energies of the occupied KS orbitals(1.11). The expression for kinetic energy (1.11) and charge density (1.10) holds true if the occupied states only have integer occupations. An example of such case is a closed shell atom where the both spin states have equal integer occupancy. But, fractional occupations can be set and are necessary in certain cases like that of a metal or a spherically symmetric atom which has odd number of electrons. In case of fractional occupation the charge density and kinetic energy gets modified to eq. (1.12) and (1.13) respectively, where f_i represents the fractional occupation.

$$\rho(\mathbf{r}) = \sum_{occ} f_i \phi_i^*(\mathbf{r})\phi_i(\mathbf{r}) \tag{1.12}$$

$$E_{kin} = -\frac{1}{2}\sum_{occ} f_i \int \phi_i^*(\mathbf{r})\nabla^2\phi_i(\mathbf{r})d^3\mathbf{r} \tag{1.13}$$

Eq. (1.8) represents the integral form of the total energy functional. In order to obtain the charge density which minimizes this functional a variation with respect to the charge density has to be applied (1.14). But since the charge density is expressed as the square of the orbitals (1.10) it can be considered equivalent to a variation with respect to the KS orbitals.

$$\frac{\delta E(\rho)}{\delta\phi_i(\mathbf{r})} = \frac{\delta E(\rho)}{\delta\rho}\frac{\delta\rho}{\delta\phi_i(\mathbf{r})} = \frac{\delta E(\rho)}{\delta\rho}2f_i\phi_i(\mathbf{r}) \tag{1.14}$$

In general the potential associated with any given energy functional can be obtained by using eq. (1.15).

$$\frac{\delta E(\rho)}{\delta\rho(\mathbf{r})} = V(\mathbf{r}) \tag{1.15}$$

The variation of the kinetic energy term (E_{kin}) with respect to the KS orbitals results in eq. (1.16)

$$\frac{\delta E_{kin}}{\delta\phi_i(\mathbf{r})} = -f_i\nabla^2\phi_i(\mathbf{r}) \tag{1.16}$$

In the multielectron system considered here the external energy is due to the nucleus of the atoms. Using eq. (1.15) on $E_{ext}(\rho)$, the expression for the external potential is found to be eq. (1.17).

$$V_{ext}(\mathbf{r}) = \sum_{A=1}^{N}\frac{Z_A}{|\mathbf{r}-\mathbf{R}_A|} \tag{1.17}$$

where $\mathbf{R}_A$ is the position of the nucleus A. Similarly, applying eq. (1.15) on E_H, the Hartree potential is given by eq. (1.18)

$$V_H(\mathbf{r}) = \int \frac{\rho(\mathbf{r}')}{|\mathbf{r}-\mathbf{r}'|} d^3\mathbf{r}' \tag{1.18}$$

However, highly accurate Hartree potentials can be obtained by converting the integral form (1.18) into differential form, resulting in the Poisson's equation (1.19). Efficient and accurate numerical methods can be employed to obtain the Hartree potential for a given charge density.

$$\nabla^2 V_H(\mathbf{r}) = -4\pi\rho(\mathbf{r}) \tag{1.19}$$

The exchange correlation potential is defined in eq. (1.20). The analytical form used in calculations depends on the choice of the exchange correlation functional.

$$V_{xc}(\mathbf{r}) = \frac{\delta E_{xc}(\rho)}{\delta\rho(\mathbf{r})} \tag{1.20}$$

Applying the variational method to the total energy expression(1.8) with respect to charge density and using the potentials in eq (1.16,1.17,1.18,1.20), a Hamiltonian (1.21) is obtained for this fictitious system of independent particles. For simplicity lets assume the system to have integer occupation($f_i = 1$ for all i) and the solution is the ground state. So, the variation will be zero (1.22).

$$H_{KS} = -\frac{1}{2}\nabla^2 + V_H(\rho) + V_{ext}(\rho) + V_{xc}(\rho) \tag{1.21}$$

$$H_{KS}\phi(\mathbf{r}) = 0 \tag{1.22}$$

But as the KS orbitals are orthonormal (1.23) to each other, this constraint needs to be incorporated in the variation which can be done through the use of Lagrange multipliers (1.24).

$$\langle\phi_i|\phi_j\rangle = \delta_{i,j} \tag{1.23}$$

$$H_{KS}\phi_i(\mathbf{r}) - \sum_j \Lambda_{i,j}\phi_j(\mathbf{r}) = 0 \tag{1.24}$$

Lagrange multipliers $\Lambda_{i,j}$ are symmetric as the constraint in eq. (1.23) is symmetric. As the $\Lambda_{i,j}$ is a Hermitian matrix, a set of canonical orbitals can be chosen such that $\Lambda_{i,j}$ is diagonalized.

The diagonalization is possible as the charge density and the kinetic energy are invariant under unitary transformations of the KS orbitals. The resultant simpler form becomes eq. (1.25) where ϵ_i are the eigenvalues and $\phi_{c,i}$ are the canonical KS orbitals.

$$H_{KS}\phi_{c,i}(\mathbf{r}) = \epsilon_i \phi_{c,i}(\mathbf{r}) \tag{1.25}$$

This form (1.25) of KS equation is commonly used in standard DFT codes where H_{KS} is the resultant Hamiltonian of the fictitious system, representing the real system. Going back to the total energy functional (1.8), the total energy can be obtained from H_{KS} via eq. (1.26) which is basically the sum of all the eigenvalues . This is known as band structure energy.

$$E_{BS} = \sum_i f_i \epsilon_i = \sum_i f_i \int \phi^*_{c,i}(\mathbf{r}) H_{KS} \phi_{c,i}(\mathbf{r}) d^3\mathbf{r} \tag{1.26}$$

Rearrangement of individual terms in E_{BS} gives rise to eq. (1.27).

$$E_{BS} = -\sum_i \frac{f_i}{2} \int \phi^*_{c,i}(\mathbf{r}) \nabla^2 \phi_{c,i}(\mathbf{r}) d^3\mathbf{r} + \int \{V_H(\mathbf{r}) + V_{ext}(\mathbf{r}) + V_{xc}(\mathbf{r})\} \rho(\mathbf{r}) d^3\mathbf{r} \tag{1.27}$$

Following eq. (1.8) the total KS energy can be expressed as (1.28). The total KS energy can also be expressed as (1.29) where the kinetic energy is replaced by the sum of the eigenvalues and other terms.

$$E_{KS} = E_{kin} + E_{ext}(\rho) + E_{xc}(\rho) + E_{n-n} + \frac{1}{2} \int V_H(\mathbf{r}) \rho(\mathbf{r}) d^3\mathbf{r} \tag{1.28}$$

$$E_{KS} = \sum_i f_i \epsilon_i + E_{xc}(\rho) + E_{n-n} - \int \{V_{xc}(\mathbf{r}) + \frac{1}{2} V_H(\mathbf{r})\} \rho(\mathbf{r}) d^3\mathbf{r} \tag{1.29}$$

1.3 The Jungle of Exchange Correlation Functional

In real, non-fictitious system the motion of one electron is correlated to the motion of other electrons. The correction terms due to the independent particle approximation are included in the exchange correlation term ($E_{xc}(\rho)$). There exists a large number of ways in which the functional can be constructed which will lead to accurate results. For comparing accuracy, the experimental values are considered as reference. During the construction of the exchange correlation functionals two points are to be noticed, i.e. (i) the accuracy in the description of properties of the system by the functional and (ii) the numerical cost associated with its evaluation.

Based on the first point the functionals can be classified into families based on certain char-

acteristics. These families can be imagined as rungs of "Jacob's ladder" where climbing each rung brings one close to the 'heaven' of chemical accuracy as explained by Perdew [4]. The computational cost increases significantly as one climbs up the ladder. The lower rungs are numerically inexpensive, but inaccurate. The major classifications of the these functionals are Local Density Approximation(LDA), Generalized Gradient Approximation(GGA) [5], meta-GGA [6], hybrid and double hybrid functionals [7]. In most of the functionals, the exchange and the correlation part is separate as it allows easy construction and incorporation of different effects.

Local Density Approximation

The LDA (1.30) is the first rung of the Jacob's ladder which is only dependent on the charge density. For systems with homogeneous distribution of charge density such as metals, this works quite well. There exists different families of LDA functionals. One of the earliest used LDA-exchange functional is the Slater exchange [8]. The LDA correlation functional developed by Vosko et. al. [9] in 1980 was one of the most popular functional of the LDA family. The drawback of the LDA functionals is that they describe poorly the lattice parameters, binding energy, atomization energy to name a few.

$$E_{LDA}(\rho) = \int \epsilon_{xc}\{\rho(\mathbf{r})\} d^3\mathbf{r} \tag{1.30}$$

Generalized Gradient Approximation Functional

The GGA(1.31) which is the second rung of the Jacob's ladder includes the dependency on the gradient of the charge density along with the charge density. This provides a better description than LDA and improves the accuracy of lattice parameters, binding energy, energetic ordering etc.. PBE [10] is the most popular GGA functional used. However, in the chemistry community, BLYP [11, 12] is preferred as it works better for small systems like molecules and clusters. Though GGA gives better lattice parameters but it fails to improve band gaps and atomization energies.

$$E_{GGA}(\rho) = \int \epsilon_{xc}\{\rho(\mathbf{r}), |\nabla\rho(\mathbf{r})|\} d^3\mathbf{r} \tag{1.31}$$

meta-Generalized Gradient Approximation Functional

The third rung of the Jacob's ladder is the meta-GGA functional(1.32) which takes into account the second order derivative of charge density $\nabla^2\rho$ and also the kinetic energy density τ. One

of the popular meta-GGA functional is TPSS [13]. It is more accurate than GGA.

$$E_{mGGA}(\rho) = \int \epsilon_{xc}\{\rho(\mathbf{r}), |\nabla\rho(\mathbf{r})|, \nabla^2\rho(\mathbf{r}), \tau\} d^3\mathbf{r} \tag{1.32}$$

Hybrid Functional

The fourth rung on the Jacob's ladder is the hybrid functional (1.33)-where a fraction of the Hartree Fock exact exchange energy is mixed with the exchange part of the GGA/LDA functional. Here in eq. (1.33) α is the mixing fraction, $E_{x,GGA}$ is the exchange part of pure GGA and $E_{c,GGA}$ is the GGA correlation energy. E_{xx} represents the Hartree Fock exact exchange energy, which is obtained from eq.(1.34). In KS formalism, the wave functions in E_{xx} are replaced by the KS orbitals. Some of the popular hybrid functionals are PBE0 [14] and B3LYP [12, 15, 16].

$$E_{hybrid} = \alpha E_{xx} + (1-\alpha)E_{x,GGA} + E_{c,GGA} \tag{1.33}$$

$$E_{xx} = \frac{1}{2}\sum_{i,j}\iint \frac{\phi_i^*(\mathbf{r})\phi_j^*(\mathbf{r})\phi_i(\mathbf{r}')\phi_j(\mathbf{r}')}{|\mathbf{r}-\mathbf{r}'|} d^3\mathbf{r} d^3\mathbf{r}' \tag{1.34}$$

Double Hybrid Functional

The fifth rung is the double-hybrid functionals which take other parameters into account such as unoccupied orbitals along with the previously discussed parameters. New improved functionals that come close to the chemical accuracy are still being generated. The accuracy of the functional is limited to only certain types of systems.

In this jungle of functionals, it is a very difficult job to decide which functional is suitable for the study of a certain system and how it is going to influence the outcome. It is more or less only experience which aid the choosing process. In the work discussed in this thesis only LDA, PBE, PBE0 and B3LYP have been used. They have been used primarily for generation of the reference data and for benchmarking the newly constructed PBE and PBE0 pseudopotentials. For structure prediction of clusters and cages discussed in chapter 7, PBE, PBE0 and B3LYP functionals have been used.

1.4 Solving Kohn Sham Equation

In the previous sections the KS formalism was introduced and discussed. As the potential in eq. (1.29) is explicitly dependent on the charge density, which is the sum over squares (1.10) of KS orbitals, it needs to be solved self consistently. Two primary methods are used for the solution of the KS equation i.e. the minimization scheme and the mixing scheme.

Minimization Scheme

The solution of the KS equation can be considered as an minimization problem in n dimensional space where the energy is to be minimized. The input guess KS orbitals can be generated using random numbers or some other schemes. Starting from the input guess KS orbitals, the estimated gradient can be used as a feedback for the search of right direction of the minimization as shown in eq. (1.35) where P is the preconditioner and g_i is the gradient. The iteration continues until the norm of the gradient is below a certain threshold value.

$$\phi_i = \phi_i - P g_i \tag{1.35}$$

Mixing Scheme

The KS equation can also be solved through a mixing scheme. Starting from an input guess, the charge density is used to construct the KS potential and hence the KS equation. The resultant KS equation is solved which is basically an eigenvalue problem. A fraction of the charge density of the input guess is replaced with the charge density obtained from the eigensolutions of this KS equation. This mixing process is continued until the difference between the input and the output charge density is below a certain threshold. Many mixing scheme exists. One of the simplest is the linear mixing scheme(1.36) where α is the mixing fraction. Other efficient mixing scheme frequently used are Broyden's method [17] and Pulay mixing [18] scheme.

$$\rho_{in} = (1-\alpha)\rho_{in} + \alpha\rho_{out} \tag{1.36}$$

1.5 Spin Polarized DFT

Upto this point only closed shell or neutral systems have been considered. No spin dependence was introduced in the KS equations. Spin treatment becomes important for systems which have odd number of electrons or where the systems are magnetic e.g. ferromagnetic cases. In this section the generalization of KS equation to spin polarized [19] treatment is discussed.

For the treatment of spin polarization, an additional variable vectorial magnetic density $m(\mathbf{r})$ is introduced. The total energy functional (1.8) in this case becomes eq. (1.37), where only the exchange correlation energy depends on both ρ and m.

$$E_{total}(\rho, m) = E_{kin}(\rho) + E_H(\rho) + E_{ext}(\rho) + E_{xc}(\rho, m) + E_{n-n} \tag{1.37}$$

The charge density ρ and magnetization vector m is constructed from the KS orbitals. In a non-spin system, the KS orbitals are independent of electronic spin and therefore each KS orbital has double degeneracy. However, in case of spin system, the KS orbitals have spin

dependence. Therefore, the KS orbitals (ϕ_i) in non-spin case splits up into two KS orbitals: one for up spin ($\phi_{i,\uparrow}$) and one for spin down ($\phi_{i,\downarrow}$).

In case of collinear spin only two components of m are required i.e. one parallel and anti-parallel to a particular direction. As a consequence, the charge density ρ and magnetization vector m can be represented as two separate charge densities: one for up spin ($\rho_\uparrow$) and one for down spin ($\rho_\downarrow$). Due to this representation, the exchange correlation potential due to the charge density $V_{xc}(\rho)$ and the magnetization vector $V_{xc}(m)$ can be expressed as eq. (1.38) for charge density with up spin and eq. (1.39) for charge density with down spin.

$$V_{xc,\uparrow}(\mathbf{r}) = \frac{\delta E_{xc}(\rho_\uparrow, \rho_\downarrow)}{\delta \rho_\uparrow} \tag{1.38}$$

$$V_{xc,\downarrow}(\mathbf{r}) = \frac{\delta E_{xc}(\rho_\uparrow, \rho_\downarrow)}{\delta \rho_\downarrow} \tag{1.39}$$

Therefore, the KS equations for collinear spin takes the form of eq. (1.40) for up spin and eq. (1.41) for down spin.

$$\left\{ -\frac{1}{2}\nabla^2 + V_H(\rho) + V_{ext}(\rho) + V_{xc,\uparrow}(\rho) \right\} \phi_{i,\uparrow} = \epsilon_{i,\uparrow} \phi_{i,\uparrow} \tag{1.40}$$

$$\left\{ -\frac{1}{2}\nabla^2 + V_H(\rho) + V_{ext}(\rho) + V_{xc,\downarrow}(\rho) \right\} \phi_{i,\downarrow} = \epsilon_{i,\downarrow} \phi_{i,\downarrow} \tag{1.41}$$

The band structure energy in eq. (1.26) becomes eq. (1.42). The total KS energy in eq. (1.29) becomes eq. (1.43). Since, the up spin and down spin orbitals only differ in spin, the variation in spin can be restricted while solving the the KS equation. This is known as spin restricted treatment. In the case of unrestricted treatment, the orbitals are allowed to vary both in space and in spin.

$$E_{BS} = \sum_i^{N_\uparrow} \epsilon_{i,\uparrow} + \sum_i^{N_\downarrow} \epsilon_{i,\downarrow} \tag{1.42}$$

$$E_{KS} = E_{BS} + E_{xc} + E_{n-n} - \int \left\{ V_{xc,\uparrow}(\mathbf{r})\rho_\uparrow + V_{xc,\downarrow}(\mathbf{r})\rho_\downarrow + \frac{1}{2} V_H(\mathbf{r})\rho(\mathbf{r}) \right\} d^3\mathbf{r} \tag{1.43}$$

1.6 Inclusion of Relativistic Effects

Relativistic effects are important for heavy elements in order to accurately describe the fast moving core electrons and their effect on valence electrons. Here we discuss the effect only for

single atom.

Now, let's consider time independent Dirac equation (1.44) in an external potential V_{ext} where p is the momentum operator in 3 dimensions, β is a 4 x 4 matrix and $\boldsymbol{\alpha}$ is a three component vector. The wave function Ψ is a four component spinor which can be divided into two components: major and minor spinor part (1.45)

$$(c\boldsymbol{\alpha}\cdot\mathbf{p}+\beta mc^2+V_{ext})\Psi = E\Psi \tag{1.44}$$

$$\Psi = \begin{pmatrix}\Psi_1\\ \Psi_2\\ \Psi_3\\ \Psi_4\end{pmatrix} = \begin{pmatrix}\Phi_A\\ \Phi_B\end{pmatrix} \tag{1.45}$$

Writing down eq. (1.44) in terms of major and minor spinor, we obtain eq. (1.46) and (1.47).

$$c\boldsymbol{\sigma}\cdot\mathbf{p}\Phi_B + (mc^2+V_{ext})\Phi_A = E\Phi_A \tag{1.46}$$

$$c\boldsymbol{\sigma}\cdot\mathbf{p}\Phi_A + (-mc^2+V_{ext})\Phi_B = E\Phi_B \tag{1.47}$$

Approaching the non-relativistic limit, the terms related to the rest mass can be removed (1.48) and the minor spinor becomes negligible. This leads to the decoupling of eq. (1.46) and (1.47). The term $\frac{E'-V_{ext}}{2mc^2}$ becomes negligible and the denominator of eq. (1.49) can be expanded via Taylor series, simplifying eq. (1.49) to eq. (1.50).

$$E' = E - mc^2 \tag{1.48}$$

$$\Phi_B = \frac{c\boldsymbol{\sigma}\cdot\mathbf{p}\Phi_A}{E'+2mc^2-V_{ext}} \tag{1.49}$$

$$\Phi_B = \left\{1-\frac{(E'-V_{ext})}{2mc^2}\right\}\frac{\boldsymbol{\sigma}\cdot\mathbf{p}\Phi_A}{2mc} \tag{1.50}$$

By replacing Φ_B in eq (1.46) with the expression from eq. (1.50), the equation is simplified to (1.51). Expanding the terms in eq. (1.51) upto the order of $(\frac{v}{c})^2$ and rearranging the total Hamiltonian takes the form (1.52) which leads to the inclusion of three additional terms. They are the relativistic correction to the kinetic energy term, the Darwin term and the spin-orbit coupling term, respectively. They can be regarded as correction terms which can be easily

included in the non-relativistic KS equation in order to take into account the relativistic effect.

$$\left[(\boldsymbol{\sigma}\cdot\mathbf{p})\frac{1}{2m}\left\{1-\frac{(E'-V_{ext})}{2mc^2}\right\}(\boldsymbol{\sigma}\cdot\mathbf{p})+V-E'\right]\Phi_A=H_P\Phi_A=0 \tag{1.51}$$

$$H=H_P-\left(\frac{p^4}{8m^3c^2}\right)+\left(\frac{h^2}{8m^2c^2}\nabla^2V\right)-\left(\frac{h}{4m^2c^2}\boldsymbol{\sigma}\cdot(\nabla V\times\mathbf{p})\right) \tag{1.52}$$

The first two correction terms are independent of electron spin and hence the KS orbitals with spatial dependence are sufficient for their description. Therefore, they are termed as scalar relativistic effects. The third term is dependent on angular momentum greater than 0, and thus breaks the spin degeneracy. This effect is known as spin-orbit coupling. The importance of these effects are discussed in chapter 2 in relation to pseudopotentials.

2 Nitty-Gritty of Atomic DFT Calculations

An atomic DFT program is the starting point of the pseudopotential construction process as it provides the reference values required for fitting. It is very important for the program to be able to generate highly accurate reference values as they effect the quality of the pseudopotentials and hence the accuracy of the proceeding DFT calculations. In this section the necessity for an atomic DFT program, the problems related to its implementation and approximations used are discussed.

2.1 Converting a 3D equation to a 1D Radial Kohn Sham Equation through Spherical Symmetry

As discussed in chapter 1, the Schrödinger equation can be solved analytically only for a few systems, for example the hydrogen atom. The solution is obtained using the approximation that the electron of the hydrogen atom is moving in a radially symmetric potential. This approximation leads to the decomposition of the solution into a radial part $\phi_{n,l}(r)$ and an angular part, known as spherical harmonic $Y_{l,m}(\theta,\varphi)$. As a result, the Schrödinger equation can be decoupled into two parts: the radial part and the angular part. Hence, the total solution can be written in the form of eq. (2.1) where n, l, m represents the principal, the angular and the magnetic quantum number, respectively.

$$\Psi_{n,l,m}(r,\theta,\varphi) = \frac{1}{r}\phi_{n,l}(r)\,Y_{l,m}(\theta,\varphi) \tag{2.1}$$

The angular part of the Schrödinger equation is equal to $-l(l+1)$. Hence, the full equation can be simplified to a 1D problem where the only variable is the radial coordinate r and the solutions are $\phi_{n,l}(r)$. The resultant Schrödinger equation can be written as eq. (2.2)

$$\left\{-\frac{1}{2}\frac{\partial^2}{\partial r^2} + \frac{l(l+1)}{2r^2} + V_{ext}(r)\right\}\phi_{n,l}(r) = \epsilon_{n,l}\phi_{n,l}(r) \tag{2.2}$$

The hydrogen atom with one electron is a simple case. For elements with multiple electrons, the system becomes more complicated as the motion of electrons is correlated with one other. However, through the KS-DFT formalism, the dependencies can be removed and the electrons can be represented as independent particles where an additional functional takes into account the unknown interactions and the errors introduced due to this approximation. For neutral atoms like alkaline earth metal and rare gases, this is satisfied by default. In case of elements that have an odd number of electrons such as aluminium, spherical symmetry can be obtained by distributing the electrons equally among the p orbitals. Though these kind of modification are applied to occupation numbers of the electrons of the atom, they are not necessarily the ground state of the atom. The resultant KS Hamiltonian of the multielectron system with spherical symmetry is given by (2.3) where V_H is the Hartree term representing the Coulombic repulsion between the electrons, V_{xc} represents the exchange correlation potential and V_{ext}(r) is the external potential due to the nucleus. The application of the KS Hamiltonian on the eigenstates gives out the eigenvalues (2.4) which are dependent on n and l.

$$H_{KS} = -\frac{1}{2}\frac{\partial^2}{\partial r^2} + \frac{l(l+1)}{2r^2} + V_H(r) + V_{xc}(r) + V_{ext}(r) \tag{2.3}$$

$$H_{KS}\phi_{n,l} = \epsilon_{n,l}\phi_{n,l} \tag{2.4}$$

Under a non-relativistic approximation, each set of principal and angular quantum numbers can have a maximum of $(2l+1)$ degenerate states as the eigenvalues are independent of the magnetic quantum number m. Therefore, the maximum occupancy of an eigenstate associated with the principal quantum number n and the angular quantum number l is $2(2l+1)$ where the additional factor of 2 comes from the electronic spin. Thus, for a spherically symmetric atom, the total wave function in 3D can be simplified to eq. (2.5). This spherical symmetry approximation of physical atoms generally proves to be a good model for the construction of the pseudopotentials.

$$\sum_{m=-l}^{l} \Psi_{n,l,m}(r,\theta,\varphi) = \frac{1}{r}\phi_{n,l}(r) \sum_{m=-l}^{l} Y_{l,m}(\theta,\varphi) \tag{2.5}$$

2.2 Radial Grids and Computation of Density Gradients

In order to solve the atomic KS equation the orbitals need to either be expressed in some basis set or directly evaluated(numerically) on a grid. In order to use the GGA or the hybrid functionals, the charge density should be mapped on a radial grid for the calculation of its gradient. For a spherical atom as discussed in the previous section, only the gradient with respect to the radial coordinate is required.

In order to represent the continuum radial coordinate, a radial grid is constructed using the relation in eq. (2.6) where A and B are some factors tuned in such a way that the radial grid propagates with a geometric progression factor and then after a certain cutoff value become equidistant.

$$r_i = A\left\{ i + \frac{1}{\log(B)} \log\{1 + \left(\frac{1}{B}\right)^i\}\right\} \tag{2.6}$$

The derivative of the charge density (2.7) is also simplified, i.e. only dependent on r due to the spherical symmetry.

$$\nabla\rho(r) = \frac{\partial\rho}{\partial r}\nabla|r| = \frac{\partial\rho}{\partial r}\frac{\mathbf{r}}{r} \tag{2.7}$$

Generally, for an uniform grid the integrals and derivatives of a function are evaluated through summation and finite differences. In order to adapt such formulation for the currently used grids let us consider an uniform grid u_j with grid size h on to which the radial grid is mapped. Lets assume h=1 a.u. for simplicity. Then, the integrals and derivatives can be written as eq. (2.8) and (2.9) respectively, where w_j and d_j are the weight and differential factors for the uniform grid.

$$\int \rho(u)du \approx \sum_j w_j \rho(u_j) \tag{2.8}$$

$$\frac{\partial\rho}{\partial u_i} \approx \sum_j \rho(u_{i+j}) d_j \tag{2.9}$$

The weight factors for integration W_j and differential factors D_j for the new radial grid (2.6) can be obtained using eq. (2.10) and (2.11) respectively.

$$\left(\frac{\partial r}{\partial u}\right)_j = W_j \tag{2.10}$$

$$\left(\frac{\partial u}{\partial r}\right)_j = D_j \tag{2.11}$$

Using these factors the volume integrals and radial derivatives of the charge density in this new radial coordinate become eq. (2.13) and (2.14).

$$\int \rho(r)dr = \int \left(\frac{\partial r}{\partial u}\rho(u)\right)du \approx \sum_j W_j w_j \rho_j \tag{2.12}$$

$$\int \rho(r) d^3r \approx 4\pi \sum_j r_j^2 W_j w_j \rho_j \tag{2.13}$$

$$\left(\frac{\partial \rho}{\partial r}\right)_j = \left(\frac{\partial \rho}{\partial u}\frac{\partial u}{\partial r}\right)_j \approx D_j \sum_i \rho(u_{j+i}) d_i \tag{2.14}$$

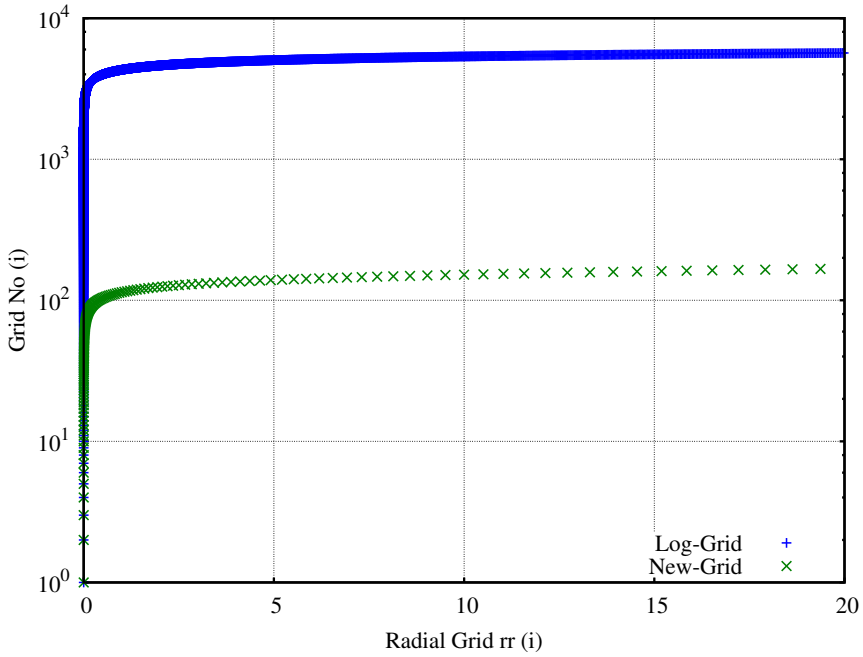

Figure 2.1: *The number of grid points with respect to the radial coordinate obtained using the logarithmic grid and the new radial grid obtained using eq. (2.6). The new radial grid requires a small number of grid points to represent the entire radial coordinate (0 to 20 a.u.) over which the calculation needs to be done without loss of accuracy.*

This form of the radial grid yields highly accurate results with μHartree precision which is comparable to the all electron references available in NIST [20] and obtained using Multi-Wavelets [21, 22], which will be discussed in chapter 5. The total number of grids required to generate the highly accurate reference value is very small. However, the logarithmic grid would require atleast a few thousand grid points in order to obtain same level of accuracy. This is clearly shown in Fig 2.1 where in order to represent the radial coordinate between 0 and 20 a.u. only ~ 200 grids points are required by the new radial grid whereas the logarithmic grid requires ~ 6000 grid points. The same program can also be used for the pseudopotential generation where only a small modification needs to be made. The earlier version of the pseudopotential generation code used a Gaussian basis set to represent the pseudo valence orbitals.

2.3 Calculation of the Spin Polarized Atom

As most of the elements in a given system are spin polarized, inclusion of spin polarization is a necessity for the production of highly accurate pseudopotentials. Treatment of spin polarization in KS-DFT has been discussed in Chapter 1. Introduction of collinear spin treatment leads to another variable called electronic spin, which can have one of two states (up or down). The KS equations are identical for both up spin and down spin orbitals where they have an additional dependency on the electronic spin. Only the exchange correlation potential depends on the individual spin charge densities. Hence, for the evaluation of the exchange correlation potential separate spin charge densities have to be produced explicitly instead of just the total charge density. This will result in two separate exchange correlation potentials for the up spin and the down spin electrons. Hence, with the inclusion of spin polarization, the KS equation becomes eq. (2.15) where the KS Hamiltonian H_{KS} is given by eq. (2.16).

$$H_{KS}\phi_{n,l,s}(r) = \epsilon_{n,l}\phi_{n,l,s}(r) \tag{2.15}$$

$$H_{KS}(r,s) = -\frac{1}{2}\frac{\partial^2}{\partial r^2} + \frac{l(l+1)}{2r^2} + V_H(r) + V_{xc}(r,s) + V_{ext}(r) \tag{2.16}$$

The total KS energy can be expressed as eq. (2.17) where α is the mixing fraction of the exact exchange Hartree Fock energy, E_{HF} is the Hartree Fock energy, E_{xc} is the exchange correlation energy and E_{eigen} (2.18) is the sum of all the eigenvalues multiplied by their occupation numbers. The terms under the integrate represent the contributions from the exchange correlation potential and the Hartree potential.

$$E_{KS} = E_{eigen} + E_{xc} + E_{ext} + \alpha E_{HF} - \int \{V_{xc_\uparrow}(\rho_\uparrow)\rho_\uparrow + V_{xc_\downarrow}(\rho_\downarrow)\rho_\downarrow + \frac{1}{2}V_H(\rho)\rho\} d^3r \tag{2.17}$$

$$E_{eigen} = \sum_i^{N_\uparrow} f_{i,\uparrow}\epsilon_{i,\uparrow} + \sum_i^{N_\downarrow} f_{i,\downarrow}\epsilon_{i,\downarrow} \tag{2.18}$$

2.4 Spin Polarized Calculation in Exchange Correlation

In this section lets try to understand briefly how the calculations of the exchange correlation functionals is done for spin polarized cases. As a simple example lets start with the LDA functional. For the evaluation of the LDA functional only the charge density ρ is required. Hence, the functional derivative of the exchange correlation energy (E_{LDA}) of the LDA functional with respect to the charge density can be expressed as eq. (2.19). Extending this approach to collinear spin systems, the spin up and spin down exchange correlation potentials takes the

form of eq. (2.20) and eq. (2.21) where the modified exchange correlation energy E_{LDA} for the Local Spin Density approximation (LSDA) is (2.22).

$$V_{LDA}(r) = \frac{\delta}{\delta\rho(r)} \int \epsilon_{xc}(\rho) d^3r = \frac{\partial \epsilon_{xc}(\rho)}{\partial \rho(r)} \tag{2.19}$$

$$V_{LSDA_\uparrow}(r) = \frac{\partial \epsilon_{xc}(\rho_\uparrow, \rho_\downarrow)}{\partial \rho_\uparrow(r)} \tag{2.20}$$

$$V_{LSDA_\downarrow}(r) = \frac{\partial \epsilon_{xc}(\rho_\uparrow, \rho_\downarrow)}{\partial \rho_\downarrow(r)} \tag{2.21}$$

$$E_{LSDA} = \int \epsilon_{xc}(\rho_\uparrow, \rho_\downarrow) d^3r \tag{2.22}$$

In case of the GGAs, the energy density ϵ_{xc} is also dependent on the gradient($\nabla\rho$) of the charge density. Hence, the above straight forward relation no longer hold. An additional correction term that arises from the dependence of ϵ_{xc} on $\nabla\rho$ is necessary in V_{GGA}. This term is known as the White Bird correction [23]. Following the White Bird correction, the exchange correlation potential for the GGA functional for the non spin polarized case can be expressed as eq. (2.23)

$$V_{GGA} = \frac{\partial \epsilon_{xc}(\rho, \nabla\rho)}{\partial \rho} - \nabla . \frac{\partial \epsilon_{xc}(\rho, \nabla\rho)}{\partial \nabla\rho} \tag{2.23}$$

2.5 LIBXC Library for the evaluation of the Exchange Correlation Functional

The LIBXC software [24] library is basically a large collection of the exchange correlation functionals which is used for the calculation of the exchange correlation potentials and the exchange correlation energy. For the atomic and the pseudopotential generation programs the LIBXC package is used. Both the programs follow the standard code convention of the LIBXC library by a six digit code with a preceding minus sign. The first three digits are related to the exchange functional and the last three to the correlation functional. In some cases only three digits are used, which is index for both the exchange and the correlation.

2.6 Calculation of the Exact Exchange for the Hybrid Functionals

Hybrid Functionals refer to those exchange correlation functionals which mix a fraction of the exact exchange of the Hartree Fock to the exchange part of the GGA functional. The act of admixing exact exchange improves the quality of the atomization energies, band gaps and

geometries for different systems. The calculation of the exact exchange Hartree Fock term is done with the use of KS orbitals rather than the charge density.

The mathematical expression for the Hartree Fock exact exchange is given by eq. (2.24). In order to evaluate this integral, initially a potential $V_{ij}^{HF}(r_1)$ is constructed for a mixed charge density $\rho_{ij}(r_1)$ (2.25) of two orbitals by solving the Poisson's equation. The resultant exact exchange Hartree Fock energy (2.26) is simply the summation of the product of the mixed charge density $\rho_{ij}(r_2)$ and the exact exchange Hartree Fock potential $V_{ij}^{HF}(r_1)$ for all possible permutations of the KS orbitals. The sum also contains the appropriate Clebsch Gordon coefficients ($A_{i,j}$), occupation (N_i, N_j) and the angular momenta (l_i,l_j).

$$E_{xx}^{HF} = -\frac{1}{2}\sum_{i,j}\iint \phi_i^*(r_1)\phi_j^*(r_1)\frac{1}{|r_1 - r_2|}\phi_i(r_2)\phi_j(r_2)d^3r_1 d^3r_2 \tag{2.24}$$

$$\rho_{ij}(r_1) = \phi_i(r_1)\phi_j(r_1) \tag{2.25}$$

$$E_{xx}^{HF} = -\frac{1}{2}\sum_{i,j}\int A_{i,j}\frac{N_i}{\sqrt{2l_i+1}}\frac{N_j}{\sqrt{2l_j+1}}V_{ij}^{HF}(r_2)\rho_{ij}(r_2)d^3r_2 \tag{2.26}$$

2.7 Relativistic Effects

The importance of relativistic effects have been discussed in Chapter 1. In this section starting from the radial Dirac equation, we will try to show similarity between the simplified radial Dirac equation and the radial KS equation. Based on this we will show that the terms arising from relativistic effects can be considered as correction terms.

Let's consider a radial Dirac eq. (2.27) and (2.28) where P(r) and Q(r) are the major and minor spinors, E is the eigenvalue and V(r) is the potential. For this set of equations a new quantum number κ (2.29) is obtained which is associated with the angular quantum number. The quantum number κ is applicable only for the orbitals whose angular momentum l is greater than 0.

$$\frac{\partial P}{\partial r} + \frac{\kappa}{r}P - (2c^2 + E - V(r))\frac{Q}{c} = 0 \tag{2.27}$$

$$\frac{\partial Q}{\partial r} - \frac{\kappa}{r}Q + (E - V(r))\frac{P}{c} = 0 \tag{2.28}$$

$$\kappa = \left\{ \begin{array}{cc} l & \text{if} \quad j = l - \frac{1}{2} \\ -(l+1) & \text{if} \quad j = l + \frac{1}{2} \end{array} \right\} \tag{2.29}$$

In the non-relativistic limit the Dirac eq. (2.27) simplifies to (2.30). The $\frac{(E-V(r))}{2c^2}$ term can be neglected in eq. (2.30) as it is very small. This leads to simplified eq. (2.31). Replacing Q in eq. (2.28) with eq. (2.31) we obtain eq. (2.32) which has the same form as the non-relativistic KS equation(2.2).

$$Q \approx \frac{1}{2c}\left\{1 - \frac{(E-V(r))}{2c^2}\right\}\left(\frac{\partial P}{\partial r} + \frac{\kappa}{r}P\right) \tag{2.30}$$

$$Q = \frac{1}{2c}\left(\frac{\partial P}{\partial r} + \frac{\kappa}{r}P\right) \tag{2.31}$$

$$-\frac{1}{2}\frac{\partial^2 P}{\partial r^2} + \frac{\kappa(\kappa+1)}{2r^2}P + V(r)P = EP \tag{2.32}$$

An accurate description of the valence electrons is necessary for the construction of a good pseudopotential. The eigenvalues of the valence electrons are much smaller than the core electrons. The relativistic effects have a small, but significant influence on the eigenvalues of the valence electrons. Due to the similarity between the simplified Dirac equation and the non-relativistic equation as shown above, the relativistic effects can be introduced as correction terms to the non-relativistic KS equation as shown in eq. (2.33). The correction terms can be obtained by replacing Q by eq. (2.30) in eq. (2.28) and expanding the term $\frac{(E-V(r))}{2c^2}$ in the resultant expression upto the order of $(v/c)^2$ as shown for eq. (1.52).

$$H = H_{KS} - \left(\frac{p^4}{8m^3}\right) + \left(\frac{\Delta V}{8c^2}\right) - \left(\frac{1}{2c^2}\frac{1}{r}\frac{\partial V}{\partial r}\mathbf{L}\cdot\mathbf{S}\right) \tag{2.33}$$

3 Pseudopotential Methods

Pseudopotential as its name suggests is some kind of empirical potential which mimics the combined effect of the nucleus and the core electrons that can be removed from the calculation. This greatly reduces the computational effort. The pseudopotential is also known as effective core potential [25–27] in Quantum Chemistry community. A review on this topic can be found in Ref. [28]. In this chapter a brief introduction about the pseudopotentials and different approaches for their construction are presented.

3.1 What is Pseudization?

In any condensed matter system, be it solid or clusters, the atoms interact with each other primarily through their valence electrons. The energetically lower core electrons do not play any significant role in chemical interaction except that of the shielding effect on the valence electrons. This assumption may not hold true in case of excited states with large energy differences with respect to the ground state. These cases were not considered during the construction of pseudopotentials in this work. As the core electrons remain neutral to the external environment, they are also known as "frozen core". Due to the orthogonality constraint, the valence electrons are forced to have oscillatory wave functions closer to the nucleus. A large basis set is required to describe this oscillatory behavior which makes the DFT calculations computationally expensive. Since the core orbitals play negligible role as explained above, the all electron Hamiltonian can be effectively replaced by a pseudo Hamiltonian which produces same set of eigenvalues for the valence electrons as the former. The only difference between them is that the pseudo Hamiltonian have weak effective core potentials which mimics the effects of the core electrons. The solution of the valence electron arising from the pseudo-Hamiltonian are called pseudo-valence orbitals. Due to the weak effective potential and removal of the core electrons in pseudo-Hamiltonian, the pseudo-valence orbitals can be smoother. Smoothness refers to the reduction in the size of the basis set which is necessary to describe the orbitals. This is represented clearly by schematic diagram in Fig 3.1. The effective core potential $V^{PS}(r)$ is weaker than the actual potential $V_{ext}(r)$. This effective core potential is known as pseudopotential.

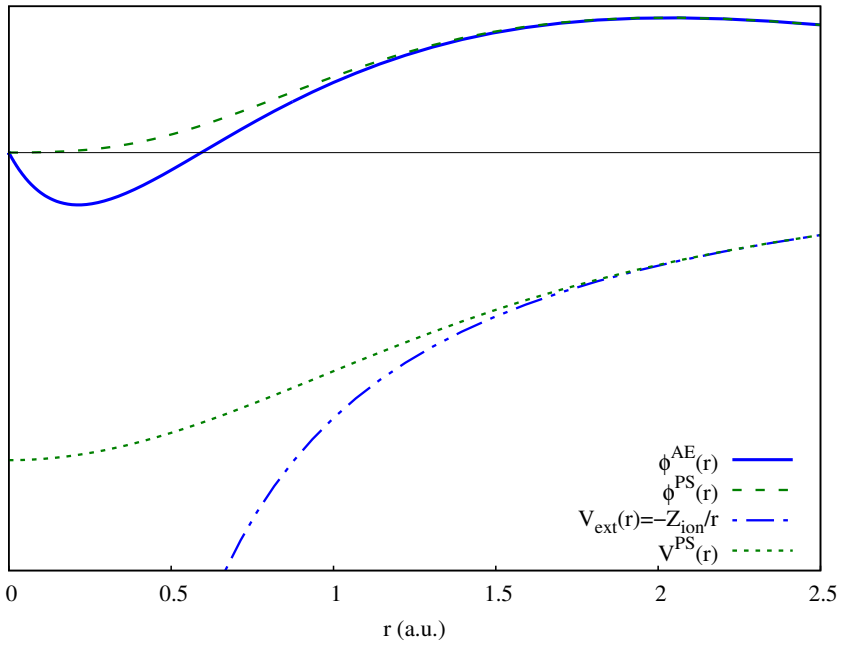

Figure 3.1: *Schematic diagram of pseudization: The replacement of $V_{ext}(r)$ with an weak potential $V^{PS}(r)$ leads to a smoother pseudo orbital $\phi^{PS}(r)$ as compared to all-electron orbital $\phi^{AE}(r)$*

The idea of pseudopotential is not only limited to the replacement of the core electrons by an effective potential. It can also be extended to all electron treatment of the atoms. For example hydrogen atom only has 1 electron which is a valence electron: no core electron exists. In this scenario instead of the nuclear potential $-1/|r-R|$, a smooth decaying effective potential can be used which does not have a singularity. This will result in a pseudo orbital whose radial part will be $(R_{10}(r))$ much smoother close to the nucleus and same as the all electron orbital in the tail region. This is explained in Fig 3.2. This is only useful in case of the light elements which has small number of electrons such as Li, Be, He etc.

3.2 Phillips Kleinman Construction

Historically, the origin of the pseudopotential method is associated with the orthogonalized planewave method (OPW) [29]. In this approach a set of pseudo valence orbitals are constructed from the combination of all electron core and valence orbitals in order to be smoother.

In order to understand the methodology let us consider an all electron Hamiltonian H whose solution gives the core orbitals ($|\phi_c\rangle$) with eigenvalues (ϵ_c) and valence orbitals ($|\phi_v\rangle$) with eigenvalues (ϵ_v). Let us consider pseudo orbitals which can be expressed in terms of $|\phi_c\rangle$ and $|\phi_v\rangle$ as expressed in eq. (3.1). The coefficient $C_{v,c}$ in eq. (3.1) is defined as the scalar product

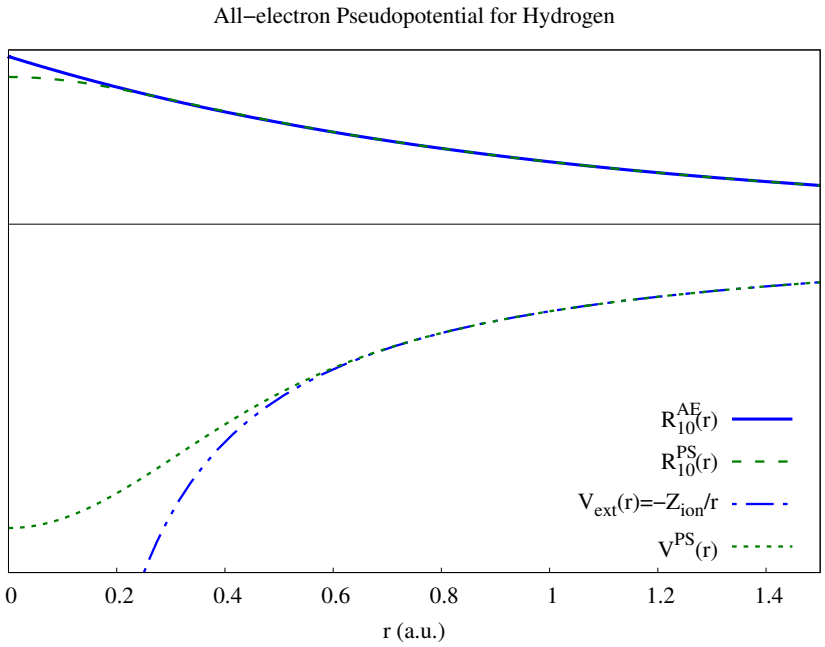

Figure 3.2: *Schematic diagram of pseudization in case of all-electron treatment: The nuclear potential of hydrogen atom is substituted with a smoothly decaying weak potential $V^{PS}(r)$ which does not have a singularity at the origin. This pseudopotential results in a pseudo orbital whose radial part $R_{10}^{PS}(r)$ has smooth behavior close to the nucleus.*

of the pseudo valence orbital and the all electron core orbital as shown in eq. (3.2)

$$|\phi_v^{PS}\rangle = |\phi_v\rangle + \sum_c C_{v,c}\,|\phi_c\rangle \tag{3.1}$$

$$\langle\phi_v^{PS}|\phi_c\rangle = C_{v,c} \tag{3.2}$$

Application of the all electron Hamiltonian on the pseudo orbital leads to eq. (3.3). Replacing the all electron valence orbital ($|\phi_v\rangle$) in eq. (3.3) from eq. (3.1), eq. (3.4) is obtained. Rearranging the eq. (3.4) leads to a pseudo-Hamiltonian (3.5) which describes the pseudo-valence orbitals. The additional potential term V_{PK} is expressed as eq. (3.6). This pseudopotential construction scheme was proposed by Philips and Kleinman [30].

$$H\,|\phi_v^{PS}\rangle = \epsilon_v\,|\phi_v\rangle + \sum_c C_{v,c}\epsilon_c\,|\phi_c\rangle \tag{3.3}$$

$$H\,|\phi_v^{PS}\rangle = \epsilon_v\,|\phi_v^{PS}\rangle + \sum_c C_{v,c}\{\epsilon_c - \epsilon_v\}\,|\phi_c\rangle \tag{3.4}$$

$$H + V_{PK} |\phi_v^{PS}\rangle = \epsilon_v |\phi_v^{PS}\rangle \tag{3.5}$$

$$V_{PK} = \sum_c \{\epsilon_v - \epsilon_c\} |\phi_c\rangle \langle\phi_c| \tag{3.6}$$

This $|\phi_c\rangle \langle\phi_c|$ in eq. (3.6) represent the projectors to the core states. The Philips Kleinman pseudopotential vanishes outside the core region as the core orbitals vanishes outside this region. Due to the inclusion of repulsive terms arising form the core, the pseudopotential turns out to be much weaker than the original potential.

3.3 Norm Conserving Pseudopotential

Pseudopotentials are often used for the description of the elements in study of the condensed matter system. For these calculations to be efficient and reliable the pseudopotential should be soft, accurate and transferable. Softer pseudopotenials need a smaller basis set to expand its pseudo valence orbitals. It is accurate if it is able to reproduce the results of all electron treatment. However, it is not enough for the pseudopotential to be accurate in ground state of the atom as in practice it is to be used in different chemical environments. This feature is known as transferability. Though these are standard definition, assessing these qualities is not always straight forward. One can always use a set of reference values of a data set for benchmarking but it is not always guaranteed as the pseudopotential construction is often done for single atoms.

But simple strategies exists so that the above mentioned qualities can be improved. They are described as follows:

- During the construction of the pseudopotential a cut off radius (r_c) is set which is typically outside the core region. At this point and beyond the pseudo valence orbital is required to match exactly the all electron valence orbital (3.7).

$$\phi^{PS}(r) = \phi^{AE}(r) \forall\, r \geq r_c \tag{3.7}$$

- In the core region the pseudo valence orbital can be as smooth as possible and hence get rid of oscillation and nodes. But the total charge of the pseudo valence orbital till the cut-off radius should be equal to that of the all-electron valence orbital (3.8).

$$\int_0^{r_c} r^2 \phi^{PS*}(r)\phi^{PS}(r)dr = \int_0^{r_c} r^2 \phi^{AE*}(r)\phi^{AE}(r)dr \tag{3.8}$$

- Eigenvalues of the pseudo valence orbitals should match the all-electron values. If all these three criteria are satisfied, then these pseudopotentials are called norm conserving

pseudopotentials.

- The scattering properties of the all-electron and the pseudo valence orbitals should match at the cut-off radius r_c. The scattering property is assessed through the the logarithmic derivative of the orbitals (3.9).

$$\left.\frac{\partial \ln\{\phi^{AE}(r)\}}{\partial r}\right|_{r=r_c} = \frac{1}{\phi^{AE}(r_c)}\frac{\partial \phi^{AE}}{\partial r}(r_c) = \frac{1}{\phi^{PS}(r_c)}\frac{\partial \phi^{PS}}{\partial r}(r_c) \tag{3.9}$$

  However, if eq. (3.7) and eq. (3.8) is followed, then eq. (3.9) is automatically satisfied.

- Logarithmic derivative of the orbitals over a range of energies is important for the assessment of the transferability of the pseudopotential. However, the energy derivative of the logarithmic derivative can be expressed in terms of charge integral as in eq. (3.8) in the core region. Hence, satisfaction of eq. (3.8) is equivalent to satisfaction of eq. (3.10) [31].

$$-\frac{\partial}{\partial E}\frac{\partial}{\partial r}\ln\{\phi(r_c,E)\} = \frac{1}{r_c^2\phi^*(r_c,E)\phi(r_c,E)}\int_0^{r_c} r^2\phi^*(r,E)\phi(r,E)\,dr \tag{3.10}$$

3.4 Semi-Local form of Pseudopotential - Bachelet Haman Schlüter construction

The pseudopotentials generated by Bachelet et. al. [32] were one of the first set of pseudopotentials to be highly successful. The scheme (BHS) followed by them for pseudopotential construction was systematic. This allowed the generation of reliable pseudopotentials and made huge advancement in the field of pseudopotential method.

As a first step an atomic reference configuration which is spherically symmetric is chosen for generation of the reference values through an atomic DFT calculation. In the following step a cut off radius for each angular momentum l of the valence orbital is set. This factor directly controls the softness of the pseudopotential as this is a norm conserving pseudopotential. The potential is constructed in such a fashion that the singularity is removed.

$$V_{trial} = -\frac{Z_{ion}}{r}\left\{1 - f\left(\frac{r}{r_{c,l}}\right)\right\} + V_{0,l}f\left(\frac{r}{r_{c,l}}\right) \tag{3.11}$$

The functional form in eq. (3.11) was considered for the input guess potential. In this equation Z_{ion} represents the ionic charge which is the difference between the nuclear charge(Z_{nuc}) and the core charge (Z_{core}) of the core electrons, $r_{c,l}$ represents the cut off radius for angular momentum l, $V_{0,l}$ represents the depth of the trial potential and f represent the cutting function which rapidly decays to zero beyond the cut off radius $r_{c,l}$. After the construction of the trial potential, norm conservation is applied on the resultant orbitals. This is done through

addition of a correction term to the resultant orbitals. If the norm conservation criteria is satisfied the final screened potential(3.13) is obtained through numerical inversion of the radial Schrödinger equation (3.12) The final screened potential still contains contributions from the Hartree potential and the exchange correlation potential. Thus, the final unscreened potential(3.14) is obtained by subtracting out this terms.

$$\left\{-\frac{\partial^2}{\partial r^2}+\frac{l(l+1)}{2r^2}+V_l(r)\right\}\phi_l=\epsilon_l\phi_l \tag{3.12}$$

$$V_l(r)=\epsilon_l-\frac{l(l+1)}{2r^2}+\frac{1}{2\phi_l}\frac{\partial^2\phi_l}{\partial r^2} \tag{3.13}$$

$$V_l^{PS}(r)=V_l(r)-\int\frac{\rho_v(\mathbf{r}')}{|r-r'|}d\mathbf{r}'-V_{xc}(\rho_v(r)) \tag{3.14}$$

The BHS pseudopotential can be divided into two parts in principle i.e. the local part which is independent of the angular momentum(l) and the other part which depends on the angular momentum. Since the second part is local only in the radial coordinates it is known as semi local form. Therefore, the total potential V_{PP} can be written as eq. (3.15)

$$V_{PP}(r)=V_{loc}+V_{SL} \tag{3.15}$$

3.5 Separable form of Pseudopotential- Kleinman Bylander transformation

Though the BHS pseudopotential was successful when it was published, it has a major drawback: it scales quadratically with respect to the size of the basis set for the calculation of the semi-local part of the pseudopotential. Secondly, it requires large memory for storing the matrix elements for its calculation. Kleinman and Bylander (KB) [33] introduced a transformation through which the non-locality of the semi-local potential on angular momentum can be removed.

Before discussing the KB transformation lets recall the projector formalism. Projectors are already introduced in discussion of the Phillips Kleinman construction. In case of a spherically symmetric atom, the projector operator $\hat{P}_l$ can be constructed with the spherical harmonics. Application of this projector operator on the KS orbitals takes the form of eq. (3.16). Following eq. (3.6) and using the projectors, application of pseudopotential V_{PP}(3.15) on the orbitals can be expressed as eq. (3.17). This term can be split into two parts i.e the local part and the semi-local part. The semi-local part (V_{SL}) of V_{PP} can be expressed as sum over different

angular momentum channels V_l(3.18).

$$\hat{P}_l\phi(r) = \sum_{m=-l}^{l} Y_{l,m}(r) \int Y^*_{l,m}(r')\phi(r')dr = \sum_{m=-l}^{l} |Y_{l,m}\rangle \langle Y_{l,m}|\phi\rangle \tag{3.16}$$

$$V_{PP}\phi(r) = \sum_l V_l^{PS}(r)\hat{P}_l\phi(r) \tag{3.17}$$

$$V_{SL}\phi(r) = \sum_l V_l(r)\hat{P}_l(r) \tag{3.18}$$

Let's assume that V_{PP} can be expressed in some form V_{sep} such that the application of the basis functions on the potential V_{sep} separates the integral as shown in eq. (3.19) where b_i are the basis functions. As both integrals are the same, only one of them needs to be computed and then can be used later. This will reduce the quadratic scaling to linear scaling with respect to the size of basis functions. This representation of V_{PP} in terms of V_{sep} is called Kleinman-Bylander transformation and the form is known as separable form.

$$\langle b_i|\, V_{sep}\, |b_j\rangle = \sum_{l,m} \langle b_i|\hat{P}_{l,m}V_l\rangle \langle V_l\hat{P}_{l,m}|b_j\rangle \tag{3.19}$$

Let's try to obtain the separable form of V_{SL} as deduced by Kleinman and Bylander. Consider an arbitary local potential V_a which is added to the local part and subtracted from the semi-local part of V_{PP} (3.20). Simplification of the projector representation of the semi-local part (3.22) of this equation leads to eq. (3.21) where δV_l (3.22) represents $(V_l - V_a)$.

$$V_{PP} = (V_{loc} + V_a) + (V_{SL} - V_a) \tag{3.20}$$

$$V_{PP} = (V_{loc} + V_a) + \sum_{l=1}^{l_{max}} (V_l - V_a)\hat{P}_l = V'_{loc} + V'_{SL} \tag{3.21}$$

$$V'_{SL} = \sum_{l=1}^{l_{max}} (\delta V_l)\hat{P}_l \tag{3.22}$$

According to the KB transformation this modified semi local part V'_{SL} is to be replaced with a separable form. The separable form can be obtained through the application of the projectors on the eigenstates of the atom $\Phi_{n,l,m}$ which are associated with the pseudpotential as shown in eq. (3.23). The eigenstate $\Phi_{n,l,m}$ contains both the radial and angular parts (3.24).

This transformation leads to identical results between the application of V_{sep} and V'_{SL} on $\Phi_{n,l,m}$.

$$V_{sep} = \sum_{n,l,m} \frac{|\delta V_l \Phi_{n,l,m}\rangle \langle \Phi_{n,l,m} \delta V_l|}{\langle \Phi_{n,l,m}|\delta V_l|\Phi_{n,l,m}\rangle} \tag{3.23}$$

$$\Phi_{n,l,m}(\mathbf{r}) = \frac{1}{r}\phi_{n,l}(r)\, Y_{l,m}(\theta,\varphi) \tag{3.24}$$

$$V_{sep}|\Phi_{n,l,m}\rangle = \delta V_l |\Phi_{n,l,m}\rangle \tag{3.25}$$

The modified semi-local part can also be expressed in terms of projectors as shown in eq. (3.26). Application of the projector form of V'_{SL} on atomic eigenstates $\Phi_{n,l,m}$(3.27) leads to same results as shown in eq. (3.25). Hence, we obtain the numerically efficient separable form.

$$V'_{SL} = \sum_{l=1}^{l_{max}} |Y_{l,m}\rangle (\delta V_l) \langle Y_{l,m}| \tag{3.26}$$

$$V'_{SL}|\Phi_{n,l,m}\rangle = |Y_{l,m}\rangle \delta V_l \phi_{l,m} = \delta V_l |\Phi_{n,l,m}\rangle \tag{3.27}$$

3.6 Limitation of the pseudopotential Methods

The pseudopotential method is based primarily on two assumptions:

- The core region remains insensitive to external environment i.e. the frozen core approximation. The change in charge density in the core region is very small.
- The contributions of the core and valence orbitals to the exchange correlation terms can be linearized i.e. $V_{xc}(\rho_{core} + \rho_{valence}) \approx V_{xc}(\rho_{core}) + V_{xc}(\rho_{valence})$. This is also true for the Hartree potential.

The validity of the approximation of the core region breaks down in case of spin-polarized atoms or molecules. Though the total charge density remains invariant in the core region, this does not always hold true for the charge density of individual spin channels [34].

The second approximations hold true if the charge density of the core and the valence electrons have small spatial overlap. During, the pseudopotential construction the classification of the core and the valence electrons is primarily based on their eigen values. Large differences in eigenvalues does not always guarantee small overlap between the core and the valence

electrons for example the transition metals. Significant error is introduced in the linearization of the exchange correlation potential if the second condition is not satisfied.

Fitting pseudopotentials to the cases where these approximations do not hold can be challenging. One way to circumvent this problem is the addition of the semicore states. Instead of the semicore states a model core charge can be also be used to account for the core-valence interaction in the exchange correlation part known as non linear core correction [34].

3.7 Semicore States - a Necessity

One way to incorporate the core-valence interaction in the pseudopotential is through addition of the semicore states on top of the valence states. Semicore states refers to those eigenstates which are difficult to classify as the core or the valence states based on the eigenvalue or spatial overlap criteria. This is exemplified in Fig 3.3 where the eigenvalue spectrum of the states are colored in accordance to classification of the core (red), the semicore (blue) or the valence states(green). In the normalized charge distribution, it can be seen that there is spatial overlap between the semicore and the valence charge distribution. Hence, the semicore states need to be treated at par with the valence states. This approach improves the description and the quality of pseudopotentials as for example in case of the 3d transition metals, addition of 3s and 3p as semi-core states is necessary to improve its accuracy.

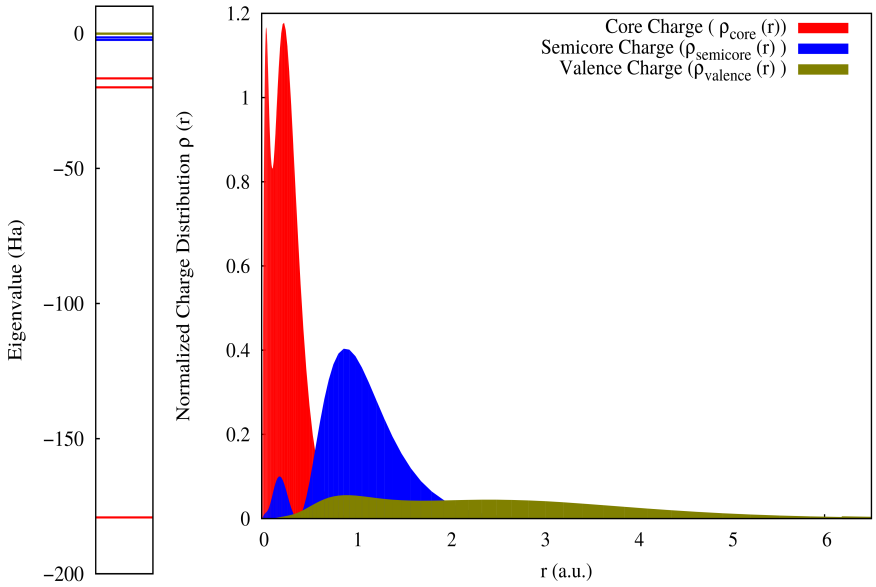

Figure 3.3: *The eigenvalue spectrum and the normalized charge distribution of the Ti atom: The electrons are classified as the core [$1s^2 2s^2 2p^2$] (red), the semicore [$3s^2 3p^6$] (blue) and the valence [$4s^2 3d^2$] (green) states. In the charge distribution it can be seen that there is significant overlap between the semicore and the valence states.*

But the addition of the semi-core states significantly increases the computational cost due to increase in the number of states to be treated in DFT calculation. This can be regarded as a trade off between the accuracy and the computational cost. In principle a soft pseudopotential with fewer electrons can be constructed but it will not be useful due to its poor transferability. This scheme can be used for the construction of pseudopotentials for the transition metals, alkaline and earth alkaline metals.

3.8 Pseudopotentials for Spin Polarized Systems

The frozen core approximation and the linearization of the core-valence interaction breaks down in case of the spin polarized calculation. Therefore, the pseudopotentials generated without spin dependence are not accurate and transferable.

In order to overcome this problem many schemes have been introduced. Zunger [35] proposed a pseudopotential where each spin channel has its own set of non-local part for each angular momentum l. Unfortunately, the constructed pseudopotential was not transferable. Zunger further proposed another scheme where a set of pseudopotentials were generated for different magnetic moments of atoms through some interpolation scheme. Then the resultant pseudopotential is expressed as combination of these potentials in such a way that it matched the magnetic moment of the atom on a given site. However, this scheme was too cumbersome and did not prove to be useful. Another scheme was proposed by Carter and Watson [36] where they introduced correction terms instead of spin dependent potentials which is linear in the local spin polarization.

Another simple and effective scheme was proposed by Louie et. al. [37] where they add a part of the core charge to the valence charge only in the calculation of the exchange correlation terms. This scheme in principle takes into account the non-linearity of the core-valence interaction in the exchange correlation. The other terms are calculated with only the valence charge density. This scheme is known as nonlinear core correction (NLCC). Most of the core charge is concentrated close to the nucleus and only a small portion of it interacts with the valence charge. Hence, the addition of partial core charge is an optimal choice. A model core charge can be used instead of exact charge density. The biggest advantage of this scheme is that a significant improvement can be obtained in accuracy and transferability without any increase in computational effort. It is also relatively easy to implement in DFT codes.

3.9 Inclusion of the Relativistic Effects

Relativistic effects are important in the description of the heavy elements. Thankfully these effects can be easily included in the model pseudopotential. In order to do this the atomic reference values are generated by solving the all-electron KS equation of an atom. This KS equation includes correction terms arising due to the relativistic effects. During, the pseudopotential fitting process, the model pseudopotential is optimized such that the solution

of the non-relativistic KS equation with the model pseudopotential reproduces this set of eigenvalues. Hence, in DFT calculations the relativistic effects can be accounted easily by solving a non-relativistic KS equation.

As discussed in chapter 2, three terms arise due to the relativistic effects i.e. the relativistic correction to the kinetic energy term, the Darwin term and the spin-orbit coupling term. The first two terms are directly incorporated in the model pseudopotential as they are spin independent and hence needs no extra set of parameters.

Generally, the spin-orbit coupling is ignored for light elements. However for the heavy elements this interaction term becomes important along with other correction terms. The spin-orbit coupling lifts the degeneracy of the eigenstates with $l > 0$ and results in spin up and spin down states which has an overall angular momentum $j = l \pm 1/2$. Hence, these two spin up and spin down states have completely different wave function and pseudopotentials. Bachelet et. al. [38] introduced an weighted average potential and a difference potential obtained from the combination of these two potentials. The average potential which takes into account scalar relativistic effects is obtained using eq. (3.28). The difference potential which describes the spin orbit coupling is obtained using eq. (3.29).

$$V_l(r,r') = \frac{1}{2l+1}\{lV_{l-1/2}(r,r') + (l+1)V_{l+1/2}(r,r')\} \tag{3.28}$$

$$\Delta V_l^{SO}(r,r') = \frac{2}{2l+1}\{V_{l+1/2}(r,r') - V_{l-1/2}(r,r')\} \tag{3.29}$$

The concept of the semi-local and the separable pseudopotential can also be extended to the relativistic pseudopotential. The only difference between the non-relativistic and the relativistic pseudopotential is that the number of terms in the relativistic pseudopotential is doubled except that of the local potential and the projectors in s channel.

3.10 Ultrasoft and Projector Augmented Wave Method

Other than the norm conserving pseudopotentials, the ultrasoft pseudopotential [39] and the PAWs [40] are often used for description of the atoms in any DFT calculation. PAWs are often considered as all electron method. In principle it is identical to all electron method if infinite number of partial waves are used in the muffin tin sphere. But in practice the number of partial waves used is quite small and finite. PAWs share a lot of similarities with the pseudopotential methods. Inside the muffin tin sphere the quality of the wave function is directly affected by the size of the muffin tin radius and the number of partial waves. In presence of finite number of partial waves, muffin tin with small radius gives better accuracy. These PAWs are called hard PAWs. On other hand ultrasoft pseudopotential method can be considered as a special case of PAWs [41]. In both the PAWs and the ultrasoft scheme, a generalized eigenvalue problem

(3.30) is solved as non-orthogonal basis set comprising of the planewaves and the partial waves are used. Here **S** represents the overlap matrix.

$$H\phi_i = \epsilon_i S\phi_i \tag{3.30}$$

If the norm conservation constraint is relaxed, the wave function inside the muffin tin can be much smoother than the norm conserving pseudopotential. These wave functions have no physical meaning and greatly reduces the number of basis functions required for its description. These pseudopotentials are known as ultrasoft pseudopotentials. The loss in charge due to nonphysical wave function is compensated through augmentation charges. This process of compensation of charge can be computationally demanding and require special algorithms to make it efficient. In addition, calculations of hybrid functionals with ultrasoft scheme can be difficult due to the complexity in the mathematical treatment for the augmentation charges for the calculation of the exact exchange in the Hartree Fock part.

3.11 Advantages of the Pseudopotential Method

Pseudopotential treatment provides great advantages in DFT calculations. These can be listed as following:

- Reduces the number of orbitals to be considered.
- Reduces significantly the size of the basis set for the description of pseudo orbitals.
- Absorbs the effect of relativity and other terms into the model pseudopotential. Hence these terms need not to be calculated explicitly.
- Reduces the numerical noise. In all-electron calculations the contribution from the core electrons to the total energy is much larger than the contribution from the valence electrons. Small relative errors in the core orbitals can therefore spoil the result and introduce considerable errors into the chemically important energy differences which are much smaller in magnitude than typical total energies.

4 Optimizing the Pseudopotential Parameters

This sections gives a brief introduction about the dual space Gaussian type norm conserving pseudopotenials, its parameters and the non linear core correction (NLCC). The strategy used for the optimization of the pseudopotential parameters for generation of soft version of these potentials are discussed. In the end some tips for generation of soft pseudopotentials are also provided.

4.1 Dual Space Gaussian Pseudopotentials

Unlike other pseudopotential families (ultrasoft or norm conserving), the dual space Gaussian pseupotential [42, 43] has a closed analytical form which consists of only few parameters. This allows to express the local potential and the projectors in terms of these parameters instead of assigning their values on a radial grid. The functional form of the local potential and the projectors are chosen based on certain desired criteria. Since different components of DFT calculations are done in real and Fourier space, it is desirable that the projectors are well localized and have smooth shape in both spaces. In this context, Gaussians are a good choice as they have optimal decay properties in both real and Fourier space. Hence, these pseudopotentials are known as dual-space Gaussian pseudopotentials. This Gaussian form of the projectors leads to efficient integration of the separable part in real space which only has quadratic scaling with respect to system size.

These dual space Gaussian pseudopotential has a local part and a non-local part. The local part in general consists of the Coulombic potential of the ionic core of the form $-Z_{ion}/r$ where the ionic core is considered to be a point charge. Here $Z_{ion} = Z_{nuc} - Z_{core}$, where Z_{nuc} is the nuclear charge and Z_{core} is the charge of the core electrons. This form has a singularity at the origin which is difficult to describe in DFT calculations using systematic basis sets like planewaves and Wavelets. However, if the ionic core is assumed to have a Gaussian charge distribution (4.1) which has a width r_{loc}, the Coulombic potential can be replaced by eq.

(4.2). This form removes the singularity at the origin and has the correct asymptotic $-Z_{ion}/r$ behavior. Along with the modified ionic potential, the local potential also includes short range potentials(4.3) which are basically Gaussians multiplied by polynomials of even order with maximum four coefficients C_k. Hence,the combination of eq. (4.2) and eq. (4.3) results in a local potential which includes both the local due to the ionic core and other common repulsive terms.

$$\rho_{ion}(r) = Z_{ion}\frac{1}{(\sqrt{\pi}r_{loc})^3}exp\left(-\frac{r^2}{2r_{loc}^2}\right) \tag{4.1}$$

$$V_{loc}(r) = -\frac{Z_{ion}}{r}erf\left(\frac{r}{\sqrt{2}r_{loc}}\right) \tag{4.2}$$

$$+exp\left(\frac{r^2}{2r_{loc}^2}\right)\sum_{k=1}^{k\leq 4}C_k\left(\frac{r}{r_{loc}}\right)^{2k-2} \tag{4.3}$$

The non-local part has a separable form where each angular momentum l can have many projectors. In dual space Gaussian pseudopotentials, the separable part has the form of eq. (4.4). The term $h_{i,j}^l$ are the weight factors in the summation of the projectors for corresponding angular momentum l. Unlike in older versions, the off-diagonal elements of $h_{i,j}^l$ are independent of diagonal elements. In similar fashion the potential for the spin-orbit coupling part is represented by eq. (4.5) where the weight factors are $k_{i,j}^l$.

$$V_l(\mathbf{r},\mathbf{r}') = \sum_{i,j=1}^{n\leq 3}\sum_{m=-l}^{l}|Y_{l,m}\rangle\, p_i^l(r)h_{i,j}^l p_j^l(r')\,\langle Y_{l,m}| \tag{4.4}$$

$$\Delta V_l^{SO}(\mathbf{r},\mathbf{r}') = \sum_{i,j=1}^{n\leq 3}\sum_{m=-l}^{l}|Y_{l,m}\rangle\, p_i^l(r)k_{i,j}^l p_j^l(r')\,\langle Y_{l,m}| \tag{4.5}$$

During regular DFT runs the spin-orbit part of the relativistic pseudopotential is ignored. If the spin-orbit part is used, then following the definition of average and difference potential in chapter 3, the two separate set of coefficients in the non-local part for spin up and spin down charge density can be written as eq. (4.6) and eq. (4.7).

$$h_{i,j}^{l+\frac{1}{2}} = h_{i,j}^l + \frac{l}{2}k_{i,j}^l \tag{4.6}$$

$$h_{i,j}^{l-\frac{1}{2}} = h_{i,j}^l - \frac{l+1}{2}k_{i,j}^l \tag{4.7}$$

The projectors $p_i^l(r)$ used in the above equations are basically Gaussian multiplied by a polynomial. In the present version of the dual space Gaussian pseudopotential, at most three projectors are used for each angular momentum l. The projectors can be obtained by using eq. (4.8). The index i can have three values i.e. three projectors. The parameter r_l i.e. the projector radius controls the width of the projectors. Each angular momentum has its own set of projectors. For the spin-orbit coupling, a separate projector radius can be introduced.

$$p_i^l(r) = \frac{\sqrt{2} r^{l+2(i-1)} exp\left(-\frac{r^2}{2r_l^2}\right)}{r_l^{l+(4i-1)/2}\sqrt{\Gamma(l+\frac{4i-1}{2})}} \tag{4.8}$$

4.2 Non Linear Core Correction (NLCC)

Willand et al. [34] found that though there exists a core region where the total charge density of an atom does not change, the charge densities of individual spin channel changes. The pseudopotentials fitted to the neutral atom is not transferable in spin polarized atoms. As explained in the previous chapter the addition of NLCC charge to the evaluation of the exchange correlation potential can solve this problem. In the latest version of the dual space Gaussian pseudopotential, a single Gaussian model charge [34] was used to represent the core charge. This model charge (4.9) has two parameters r_{core} and c_{core}. The parameter r_{core} controls the width of the Gaussian and the prefactor c_{core} controls the fraction of the core charge to be added. The remaining factors other than c_{core} and the Gaussian are the constants of normalization. The volume integral of this model core charge (4.10) gives the amount of the core charge included for NLCC.

$$\rho_{core}(r) = c_{core}\frac{Z_{nuc} - Z_{ion}}{(r_{core}\sqrt{2\pi})^3} exp\left(-\frac{r^2}{2r_{core}^2}\right) \tag{4.9}$$

$$\int_0^\infty 4\pi r^2 \rho_{core}(r) dr = c_{core}(Z_{nuc} - Z_{ion}) \tag{4.10}$$

4.3 Confining Potential

The extent of the KS orbitals of the atoms is influenced by the type of boundary conditions and the chemical environment. In condensed matter system, the orbitals are spatially localized as compared to an atom in free boundary conditions where the KS orbitals have a slow decaying tail. In order to create a pseudopotential which can mimic this behavior, it is necessary to include this spatial localization in the fitting process. Hence, the atom is placed in a smoothly varying parabolic potential. The mathematical form of this external potential is given by eq.

(4.11).

$$V_{rprb} = \frac{1}{2}\left(\frac{r^2}{r_{rprb}^4}\right) \tag{4.11}$$

The parameter r_{rprb} controls the broadening of the confining potential. A large r_{rprb} value leads to a very weak confining potential. This becomes equivalent to free boundary conditions. A small value of r_{rprb} leads to very strong confining potential which can be considered equivalent to the situation of the atoms under high pressure. Hence, by manipulating the parameter r_{rprb}, a pseudopotential suited for a particular application can easily be generated. It has been found that $r_{rprb} = 2r_{cut-off}$ is optimal for the generation of pseudopotentials which are required for standard applications. Here $r_{cut-off}$ is the cut-off radius at which the norm conservation of the orbitals are checked. The cut off radius is a scaled value of the covalent radius of the element. In addition to the above features, the confining potential also allows the inclusion of unoccupied orbitals for different angular momentum l. Due to their inclusion several atomic configuration which are basically excited states can be created.

4.4 Amoeba - Simplex Downhill Method for fitting

The fitting of pseudopotential parameters can be considered equivalent to an optimization problem where the goal is to minimize the penalty function. The exact form of the penalty function used is discussed in next section. The penalty function consists of terms which take into account different atomic properties such as eigenvalues and charge densities of the atomic KS orbitals. What makes the fitting process difficult is the wide range of values the parameters of the dual space Gaussian pseudopotential can have. The accuracy and convergence rate of the DFT calculations is directly influenced by these pseudopotential parameters. Hence, the optimization of the pseudopotential parameters can be significantly effected by the random moves. For this kind of problem, a simplex downhill method is found to be suitable. It is also known as Nelder Mead Method [44] or amoeba method. In this method a simplex is created which is made of N+1 vertices. Each vertex is a collection of N fitting parameters. The algorithm used in amoeba method is described below:

1. After the creation of the simplex, the center of the simplex is obtained which is the average of all vertices.
2. The vertex with highest penalty value is reflected at the center.
3. The new reflected vertex is accepted if it does not have the highest penalty value. The vertex with the highest penalty value is replaced with the reflected vertex.
4. In case if the penalty value of the reflected vertex is lowest.
    - The vertex is moved along the reflection axis.

- The new vertex is accepted if the penalty value goes down.
- Else the reflected vertex is stored back.
- The vertex with the highest penalty value is replaced with the accepted vertex

5. If the penalty value of the reflected vertex is highest.
   - The reflected vertex is rejected.
   - The vertex is contracted towards other vertices.
   - If the contracted vertex has a lower penalty value than the initial vertex, the new contracted vertex is accepted. It replaces the vertex with the highest penalty value.
   - If no then all the vertices are contracted towards the vertex with lowest penalty value
6. This process continues until all the vertices converge to a single point i.e. the difference between the highest penalty value and the lowest penalty value is below a certain threshold value.

In order to create the simplex in the amoeba method different sets of parameters are required. These sets of parameters are generated using the random number generator along with the input guess parameters. To add flexibility in the control of the optimization process, a prefactor a_{fact} was introduced along with the variation generated by random number as shown in eq. (4.12) and eq. (4.13) where $rand$ is the random number. The parameter a_{fact} is decided by the user through an input file. This is useful as parameters like projector radius (r_l) or local radius (r_{loc}) vary in small magnitude (0.001) but the $h^l_{i,j}$ parameters vary significantly(1-10).

$$xx_{new} = xx_{old} + rand * a_{fact} \tag{4.12}$$

$$xx_{new} = xx_{old} + xx_{old} * rand * a_{fact} \tag{4.13}$$

The variation in the radial parameters such as r_{loc}, r_l and r_{core} are controlled through the sigmoid (4.14) function.

$$r_{new} = r_{old} + a_{fact} r_{old} \frac{2\tan^{-1}(rand)}{\pi} \tag{4.14}$$

The prefactor of the model Gaussian core charge (c_{core}) in NLCC cannot be greater than 1 in principle. But it is difficult to optimize this parameter due to the presence of r_{core} in the denominator of the normalization constant which leads to a large value. Due to this large amplitude, the variation of c_{core} has very small effect on the optimization process. To get rid of this problem the $(Z_{nuc} - Z_{core})$ along with c_{core} is treated as a single term g_{core} =

$c_{core}(Z_{nuc} - Z_{core})$. This single term is fitted during the optimization process. After the optimization process, the c_{core} can be easily extracted as the rest of the term is known. In order to introduce a change in g_{core}, it is expressed as variable θ using eq. (4.15). Then the change in θ is introduced using eq. (4.16). After obtaining the new θ_{new}, g_{core} is extracted back using eq. (4.17).

$$\theta = \tan\left\{\left(\frac{g_{core}}{Z_{nuc} - Z_{core}} - 0.5\right)\pi\right\} \tag{4.15}$$

$$\theta_{new} = \theta_{old} + |\theta_{old}| a_{fact} * rand \tag{4.16}$$

$$g_{core} = (Z_{nuc} - Z_{core})\left(\frac{1}{2} + \frac{\tan^{-1}\theta_{new}}{\pi}\right) \tag{4.17}$$

4.5 The definition of the Penalty Function

The penalty function used for the amoeba method is basically a sum of quadratic functions multiplied by a weight factor. This equation consists of values obtained from all electron calculation and pseudopotential calculation. The values obtained from all electron calculation are the reference values. The pseudopotential parameters are optimized such that the values obtained from pseudopotential calculation comes close to the all electron reference values. The penalty function can be expressed as eq. (4.18). In this equation the subscript AE relates to the values obtained through all electron calculation and PS refers to the values obtained for the pseudopotential calculation.

$$\begin{aligned} P = \sum_i \sum_{n,l} \{ & w^2_{EE,n,l}(EE^{AE}_{i,n,l} - EE^{PS}_{i,n,l})^2 + w^2_{CC,n,l}(CC^{AE}_{i,n,l} - CC^{PS}_{i,n,l})^2 \\ & + w^2_{SS,n,l} SS^2_{i,n,l}\} + w^2_{excit} \sum_{i<j} (\Delta E^{AE}_{i,j} - \Delta E^{PS}_{i,j})^2 \end{aligned} \tag{4.18}$$

The first term in eq. (4.18) corresponds to the penalty due to the difference in eigenvalue of the all electron and pseudo orbitals. Similarly the second term relates to the penalty due to the difference in charge density of the all electron and pseudo orbitals. Along with the occupied states, the unoccupied states are also considered in this penalty terms. These two quantities take into account the scattering property of the pseudo orbitals.

The third term in eq. (4.18) is associated with the penalty due to the softness of the pseudo orbitals. The softness term ($SS_{i,n,l}$) associated with each pseudo orbital can be expressed as eq. (4.19) which is a product of kinetic energy and an exponential function. This is motivated by the fact that the kinetic energy is a good indicator of the hardness of the wave function. A low kinetic energy indicates that the orbitals are smooth. The parameter $r_{d,n,l}$ is uniquely

defined for each orbital by the user in an input file. The variable $w_{EE,n,l}, w_{CC,n,l}, w_{SS,n,l}$ in eq. (4.18) represents the weight factors for the eigenvalue penalty term, charge density penalty term and softness penalty term respectively.

$$SS_{i,n,l} = \int_0^\infty 4\pi r^2 \frac{1}{2} \phi_{i,n,l} \nabla^2 \phi_{i,n,l} exp\left(- \frac{r}{r_{d,n,l}} \right) dr \tag{4.19}$$

During the pseudopotential fitting process multiple atomic configurations are considered. The fourth term in eq. (4.18) represents the penalty due to the difference in the total energy of different atomic configurations. This term incorporates the transferability property into the pseudopotential. The weight factor w_{excit} for this penalty term is same for all the atomic configuration.

The fitting of pseudopotential parameters over multiple atomic configuration is done through MPI parallelization where each atomic configuration is assigned to a MPI process. Each MPI process takes care of the calculation of the penalty terms for the eigenvalue, charge density and the softness terms associated to that particular atomic configuration. The MPI processes communicate only during the calculation of the difference of the total energy of different atomic configuration. All the atomic configuration uses the same set of weight factors.

4.6 Some tips for generating Dual space Gaussian pseudopotential

During the introduction of the dual space Gaussian pseudopotential, it was mentioned that altogether there are around 40 parameters out of which only few (10 - 20) need to be optimized depending upon the element under consideration. For example in case of the hydrogen atom only the local potential is sufficient whereas in the case of zinc along with the local potential, projectors for s, p and d channels are required for the description of its pseudo atom. Optimizing this set of parameters is not always a straight forward job. It is often necessary to have a good input guess to obtain a pseudopotential with desirable characteristics. In principle one can fit the parameters to any values which minimizes the penalty function but it may not be physically relevant.

An important feature of the dual space Gaussian pseudopotentials is that the parameters of the pseudopotential follow the trends of the periodic table as shown in Fig 4.1. Hence, if a good pseudopotential exists of a neighboring chemical element, then the pseudopotential of this neighboring element can be used as an input guess. The parameters in particular the projector (r_l) and local radius (r_{loc}) can be obtained through simple interpolation. On other hand if an old pseudopotential of the element exists, it can also be used as an input guess. It might happen that the penalty minimization gets stuck with a particular set of parameters which may not correspond to a good quality pseudopotential. In that case the fitting process has to be restarted with manually chosen parameters.

Among the different pseudopotential parameters, the local radius r_{loc} needs to be handled

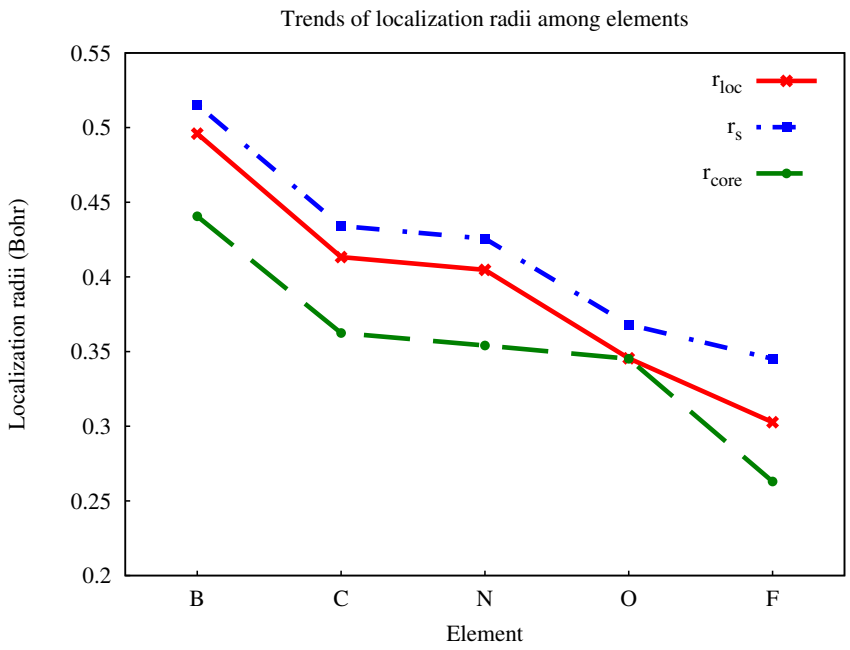

Figure 4.1: *Trends of r_{loc} (local radius), r_s (s-projector radius) and r_{core} (width of the Gaussian core charge in NLCC) among the elements of second row in the periodic table.*

with care. This parameter controls the softness of the local part. This is clearly demonstrated in Fig 4.2. A large value of local radius r_{loc} leads to a softer local potential. But large r_{loc} values leads to non physical description of the atom as it extends beyond the frozen core region. This feature can be easily judged by comparing the pseudo orbitals and all electron orbitals. The spatial variation of the first few valence or semicore orbitals should not extend much beyond the frozen core region. This philosophy cannot be used in the case of only valence pseudopotentials where the projector radii are quite large. Hence, the local radius needs to be kept frozen or varied only by a small quantity during the fitting cycle.

Another important point is the set of atomic configurations to be considered for the generation of reference values. In order to capture all possible chemical environments both the spin polarized and non-spin polarized cases of the atom in neutral, excited and ionized states needs to be considered. A confining potential helps to include the unoccupied orbitals and spatially limit the extend of the orbitals.

The set of weight factors used in the fitting is not well defined. Generally the user gets a feeling of the values based on experience. During the fitting cycle the penalty of different components are printed out so one can keep track on which quantities are improved. In certain cases user intervention is required to modify the weight parameters when one set of penalty term is minimized compared to others. For example if one puts a larger weight on the scattering property instead on the excitation energies, the fitting process will deliver a pseudopotential

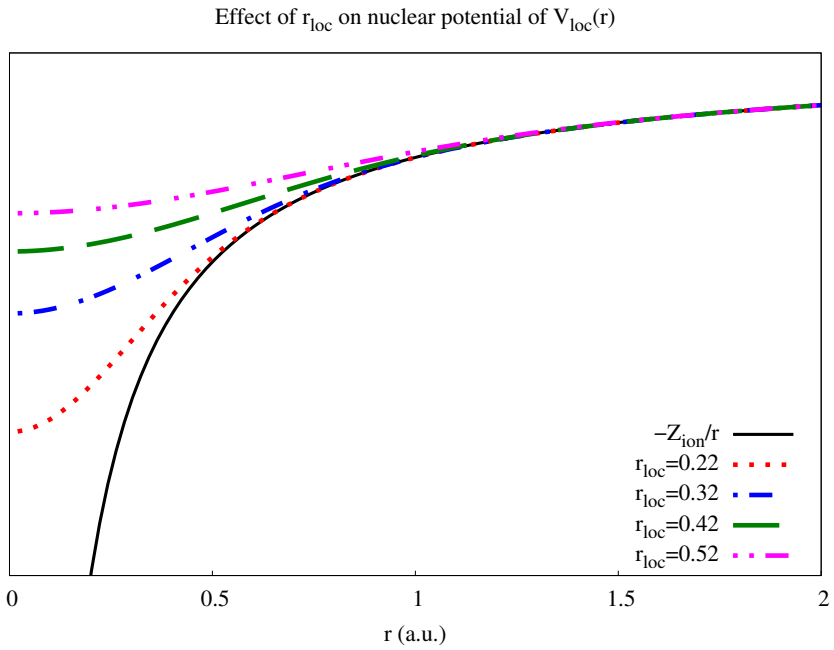

Figure 4.2: *Model Coulombic potential (4.2) of the ionic core for different values of r_{loc}: The figure shows how the smoothness of the Coulombic potential is effected by the parameter r_{loc}. Large values lead to weaker potential which extends beyond the frozen core region. This severely affects the accuracy of the pseudopotential.*

with better scattering properties in comparison to the excited states.

4.7 Fitting Pseudopotential Parameters

In this section the strategies followed for the generation and fitting of pseudopotential parameters are discussed. This fitting process was done for the PBE and PBE0 functionals with a non-relativistic treatment. The protocol followed is explained below:

- A set of multiple atomic configuration is initially constructed. The cut-off radius and the parameter for the confining potential is set.
- A set of reference values is generated by running the atomic program on multiple atomic configurations.
- One of the existing old pseudopotentials [34, 45] was chosen as an input guess.
- As a preliminary run the pseudo code was executed with no fitting cycle with the selected input guess. This process simply solve the KS equation and print out the difference in the eigenvalues, charge densities, excitation energies and softness term. This process

was repeated for a few sets of the pseudopotential parameters which were obtained by applying simple interpolation.

- Once a good input guess is obtained, the weight parameters were set. The assignment of weight factors was based on the criteria that there should be a balance between the weight on softness term and scattering properties. As a first step a high weight is imposed on the eigenvalues and charge densities such that the scattering properties get better. But at the same time the weight on the excited energies and the softness is decided such that their quality do not deteriorate because of improvement in scattering properties.
- With these settings, few optimizations runs are done with the amoeba method as implemented in the pseudopotential fitting program.
- Once good scattering properties are obtained from optimization runs, weight on excitation energies are increased gradually. As the scattering properties are good enough, high accuracy in excitation energy is easily reached through few more optimization steps.
- In the end the weight factors for the softness penalty term is increased in order to take care of the softness of the pseudopotential. As each pseudo orbital has its own set of weight factors for eigenvalues, charge densities and softness terms, the shape of individual orbitals can be controlled.

In the end all the weight factors were tuned such that an accuracy of 10^{-4} Ha is reached in the pseudo orbital eigenvalues of the occupied orbitals and at least 10^{-3} in unoccupied orbitals with respect to the all electron reference values. For the excited energies a target accuracy of 10^{-4} Ha was set and for the charge densities 10^{-4} against the all electron reference values. During the fitting cycles for the excited energies and the softness term, the radii parameters of the pseudopotential are kept frozen or varied only by a small fraction. The convergence rate of the pseudopotentials in a DFT run was also considered in its judgement as good or bad pseudopotential. Generally pseudopotential with large $h^l_{i,j}$ values tends to have convergence problems.

For the generation of the PBE0 pseudopotentials the above strategy was used where the PBE pseudopotentials was used as an input guess. Through this process new soft and transferable pseudopotentials were generated for all elements till the 3rd row of periodic table. PBE pseudopotential with relativistic treatment were also generated for a few 3d transition metals, the whole 4d transition metals and for all the alkaline and earth alkaline metal except Ba and Fr. The accuracy of these pseudopotentials were benchmarked against the atomization energies of a large dataset of 211 molecules and through the Delta test [46] of elemental solids.

5 All Electron Reference Data for Benchmarking

Highly accurate reference values are essential for benchmarking and estimating the errors of newly developed exchange correlation functionals, basis sets, pseudopotentials or DFT codes. Though there exists a large amount of reference data and benchmarks on molecular systems, most of them are unreliable due to the errors introduced by the basis set.

The necessity of a highly accurate reference data can be understood from this example. The atomization energy of $SiCl_4$ is less than 1 Ha but it is obtained as a difference between the total energy of the molecule and its constituent atoms. The total energy of the molecule is about ~ 2000 Ha. It is important to note that though the atomization energy is small compared to the total energy of the molecule, it is obtained as difference of two large terms. In these cases it is important to have low noise in the total energy due to the basis set or the integration grids. An accuracy of 1 μHa is necessary in the total energy to obtain reliable atomization energies with a chemical accuracy of 1 kcal/mol.

Using Multi-Wavelets basis set it has been possible for the first time to obtain total and atomization energies with μHa accuracy for a large data set of molecules. These reference data have been used to estimate the basis set error of other families of basis set such as Gaussian Type Orbitals (GTOs), Numeric Atomic Orbitals(NAOs) and Augmented Plane Waves(APW). These set of reference data were further used for benchmarking the new soft dual space Gaussian pseudopotentials which is discussed in chapter 6. Along with the molecular energies, delta test [46] of elemental solids was also used for evaluation of the accuracy of the pseudopotentials. In this chapter all the details associated with the generation of the accurate reference values and related studies are discussed.

5.1 Gaussian Type Orbitals for Reference Data

In the literature there exist a large number of benchmark studies [20, 47, 48] of different kind of data sets consisting of molecules. GTOs have been popular in the chemistry community due to its simple analytic form and straight forward analytical integration. These studies are mostly done using quantum chemistry codes which use GTOs as basis set. There exists few studies [47, 49] which show an improvement in accuracy with respect to the reference data with an increasing size of the basis set. Though popular, GTOs have major problems which are difficult to circumvent. They are listed below:

1. As the GTOs basis set is not systematic, increasing the basis set size does not guarantee more accurate energies.

2. Using a large basis set may introduce convergence problems due to linear dependencies particularly in large systems [50]. To overcome this kind of problem a general strategy followed is the removal of few basis functions.

3. It is difficult for GTOs to describe the region close to the nucleus and in the tail region. Close to the nucleus the GTOs cannot describe the electron-nucleus cusp i.e. the discontinuity in the first derivative. In the tail region the wave function decays exponentially ($\exp(-\alpha r)$) whereas the Gaussian decays rapidly ($\exp(-\tilde{\alpha} r^2)$) in comparison to the exponential function.

5.2 Why Multi-Wavelets?

The problems associated to the use of GTOs is already discussed in the previous section. On the other hand using Numeric Atomic Orbitals(NAOs) [51] as a basis set, a different set of reference values is obtained for the same systems. Ideally all the quantum chemistry codes in the complete basis set limit should converge to a single reference value with some threshold irrespective of the basis set used. However, this is far from reality. Another issue related to use of a large basis set is the convergence problem in case of large systems due to linear dependencies [50]. This is very complicated situation. As both basis set (GTOs and NAOs) are not systematic, it is difficult to judge which one is more accurate and they cannot be considered as absolute reference values. Fortunately, the MWs basis set have all the necessary features to solve this problem. The methods related to MWs have already been developed [52–55]. It is systematic, adaptive and can be used in all electron calculations.

5.3 Computational Methods

5.3.1 Data Set of Molecules

For the creation of the data set, the molecules present in the G2/97 Test Set [56, 57] were considered. This test set consists of 148 molecules and radicals which represent elements upto the 3rd row of the periodic table. The structures reported in the literature are optimized at the MP2 level of theory. However for our study we obtained the experimental structures from the NIST database [20]. In case of missing experimental data, the optimized geometry at the MP2 level of theory with the largest basis set present in NIST was considered.

Though the test set consists of large number of molecules, a few elements are under represented for example Li, Be, F, Na, Mg, Al, S and Cl. The test set also lacked other possible combination of different chemical elements. There were no noble gases in this test set. Taking this into account additional 58 molecules were considered which also include dimers of noble gases. In order to assess the error in the case of non-covalent bonding, 6 extra molecules were considered. Altogether the data set consists of 212 molecules. The total energy, the atomization energy and the electrostatic dipole moment of the molecules are considered for comparison. Only single point energy evaluations were done. The details of the data set and reference values can be found in [58]. Single atom energies for the LDA functional were obtained from the NIST Atomic Database [59].

5.3.2 DFT Codes used in this Benchmark Study

In this work our goal was to generate highly accurate reference values using MWs and use them to judge the accuracy of other basis sets which are frequently used. The basis sets used for this study were GTOs [60, 61], NAOs [51] and MWs. Among the solid state community, Augmented Plane Wave(APW) [62] method is considered to be gold standard. Hence, APW is also considered. In order to use these basis sets, the DFT codes NWCHEM [63] for GTOs, FHI-AIMS [64] for NAOs, MRCHEM [65] for MWs and ELK [66] for APW was used. The settings for the different codes were set such that the only contribution to the error comes from the basis set. Hence, largest number of radial grids and integration grids were considered.

Though large basis set are generally used for benchmark studies, in regular production runs medium size basis sets are used and for quick pre-relaxation small basis sets are used. Hence, the assessment of the quality of the basis set was extended to both type and size of the basis set. One basis set representing each category was considered. For the GTOs 6+31G**, aug-cc-pVDZ, aug-cc-pVTZ and aug-cc-pV5Z were used. The aug-cc-pVQZ basis set was used for Li, Be, Na and Mg instead of aug-cc-pV5Z as it was not available. In the case of NAOs light, tight, tier2 and tier4 basis sets were used. For light and tight basis set the default settings were used. In case of MWs a precision parameter was set for the individual components of the total energy depending on which the basis set was constructed systematically. All this information is summarized in Table 5.1. In order to evaluate the exchange correlation functional the

LIBXC [24] library was used in NWCHEM and FHI-AIMS whereas the XCFUN [67] library was used in MRCHEM. The runs for APW could only be done for the LDA functional for a handful of molecules as it is very computationally challenging and one needs a very large computational box in order to converge the energy to the to free boundary solution.

For other DFT codes, the runs were done for both the PBE and the PBE0 functionals. In order to make a fair comparison it was essential to converge all the solutions among the different codes to the same ground state. This is technically a challenging task as the molecules have a large number of metastable electronic states. For the errors in the atom energies along with the PBE and the PBE0, the SVWN5 [8, 68] functional was also considered.

DFT Code	Basis Set			
	Type	Size		
		Small	Production	Large
NWCHEM	GTOs	6-31+G**	aug-cc-pVDZ aug-cc-pVTZ	aug-cc-pV5Z aug-cc-pVQZ (for Li, Be, Na and Mg)
FHI-AIMS	NAOs	light	tight tier2	tier4 tier3(Hydrogen)

Table 5.1: *The basis sets are classified according to their types, size and the DFT codes which use them.*

5.4 Results

For the comparison study of the basis sets, both single atoms and molecules were considered. Generally it is found that the errors in single atom energies are much larger than molecular energies. The study of the atom energies were done in order to observe trends in the errors of the energies with respect to the elements for a given basis set. In order to judge the quality of the charge density, the electrostatic dipole moments of the molecules were also considered. The results of the comparisons are discussed below in different sections.

5.4.1 Error in Atom energies

As an initial step of the comparison study among different types of basis sets, single atom energies were considered. It is much simpler to study the errors in single atoms rather than molecules. There exist many exchange correlation functionals which could have been studied. However, the most popular ones PBE and PBE0 were considered. Here PBE represents the GGA functional and PBE0 the hybrid functionals. In order to judge the accuracy of the MWs an independent set of reference values are required. Thankfully, highly accurate values of atom energies for SVWN5 functionals are available in the NIST database [59]. These values were obtained using four independent atomic programs which agree upto six decimal places. Only the light elements (upto the 3rd row of the periodic table) have been considered. Among

these elements which are spherically symmetric in their ground state were considered for the comparison study of the SVWN5 functional as the atom energies reported in the NIST database are for spherically symmetric atoms.

In Fig 5.1 the errors for different type of basis sets among different functionals are summarized. Here the values reported are only for the most accurate basis set employed in each case. In the first panel the absolute errors for the SVWN5 functional are reported. As mentioned previously MWs could achieve consistently μHa accuracy for all the elements. The NAOs could achieve on average ~0.01-0.1 mHa accuracy. It is interesting to note that NAOs could achieve the same accuracy as MWs for the elements with closed shell configuration. The absolute error in the case of APW lies between ~0.1-1 mHa. The absolute errors in the case of GTOs is about 1 mHa. There is a clear trend of increase in the error with an increase in the atomic number of the elements for GTOs. However, the elements Li, Be, Na and Mg are outliers. This is due to the fact that the aug-cc-pVQZ basis set was used for them instead of the aug-cc-pV5Z as it was not available.

However for the PBE (second panel) and the PBE0 (third panel) functionals all the 18 elements were included for the error estimation. The atom energies obtained from MWs were used as reference values. The GTOs in NWCHEM perform at the limit of chemical accuracy (1 mHa). The NAOs in FHI-AIMS performs better and could achieve an accuracy less than 0.1 mHa except for flourine(0.3 mHa). The exact match of the closed shell elements could also be found for the PBE and PBE0 functional. This is because the exact radial functions of spherically symmetric spin-unpolarized atoms are part of the NAOs basis set. The trend of increasing absolute errors with respect to the atomic number Z is also observed in the PBE and the PBE0 functionals for GTOs with the same outliers as found for the SVWN5 functional. On the other hand, the nuclear charge(Z) has minor influence on the accuracy of the NAOs basis set. For APW only the SVWN5 values are reported. Converging with respect to the box size is both a technically demanding and memory intensive task. The APW method is not optimal for these kind of systems.

5.4.2 Error in Molecular Energies

It is difficult to estimate the errors in the energies of molecules from the errors of individual single atoms. This is because there exists no qualitative argument or quantitative expression for this comparison. Generally it is found that the error in the energies of molecules are much lower than the errors in energies of the single atom. As the DFT calculations deal with polyatomic systems, it is more useful to estimate and benchmark the errors in large systems rather than single atoms. In order to estimate the basis set error for the basis sets under study, total energies, atomization energies and electrostatic dipole moments of a large data set of 211 molecules as discussed in section 5.3.1 were computed for both the PBE and the PBE0 functional. Absolute reference values were obtained using MWs as implemented in MRCHEM with the highest affordable precision (1 μHa in all cases).

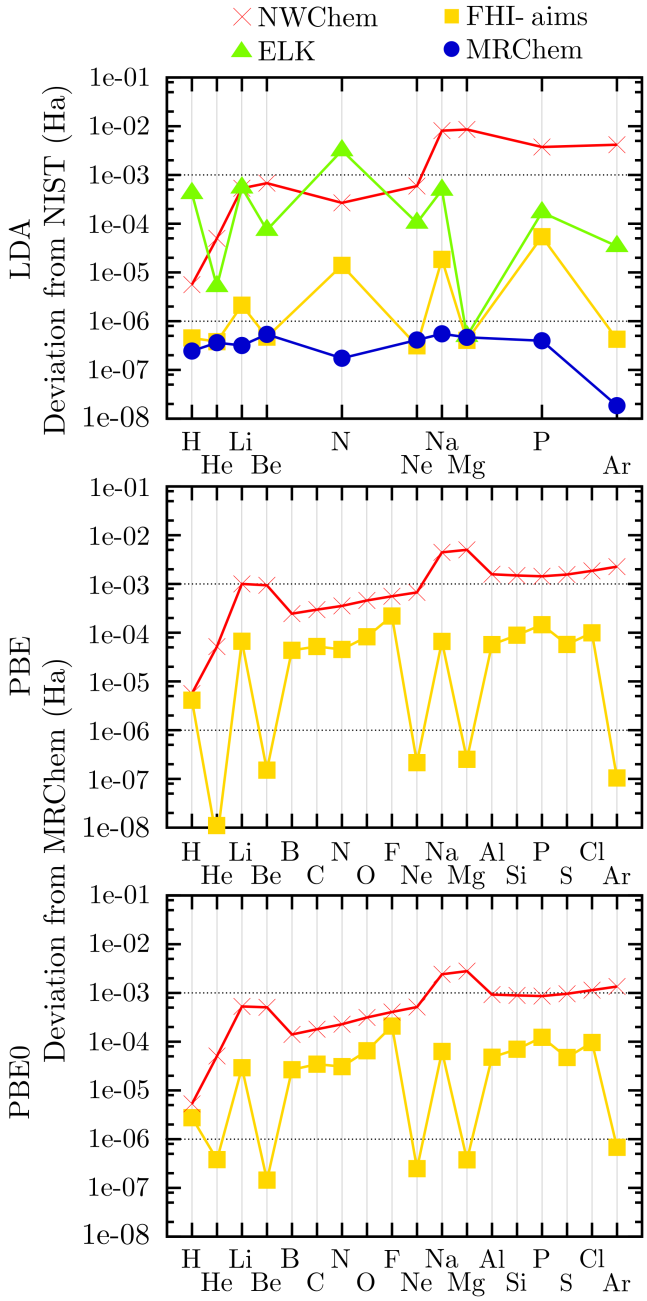

Figure 5.1: *Absolute deviation in total energy found for different functionals for selected atoms. For LDA-SVWN5, energy differences are w.r.t. NIST all-electron values. [59] For GGA-PBE and hybrid-PBE0, the energy differences are w.r.t* MRCHEM. *In all codes the largest basis set and tighter parameters were used. In all plots the reference values (NIST for LDA and* MRCHEM *for PBE/PBE0) are given with 6 decimal precision;a displayed error below 1e-06 Ha means that no discrepancy is detectable.*

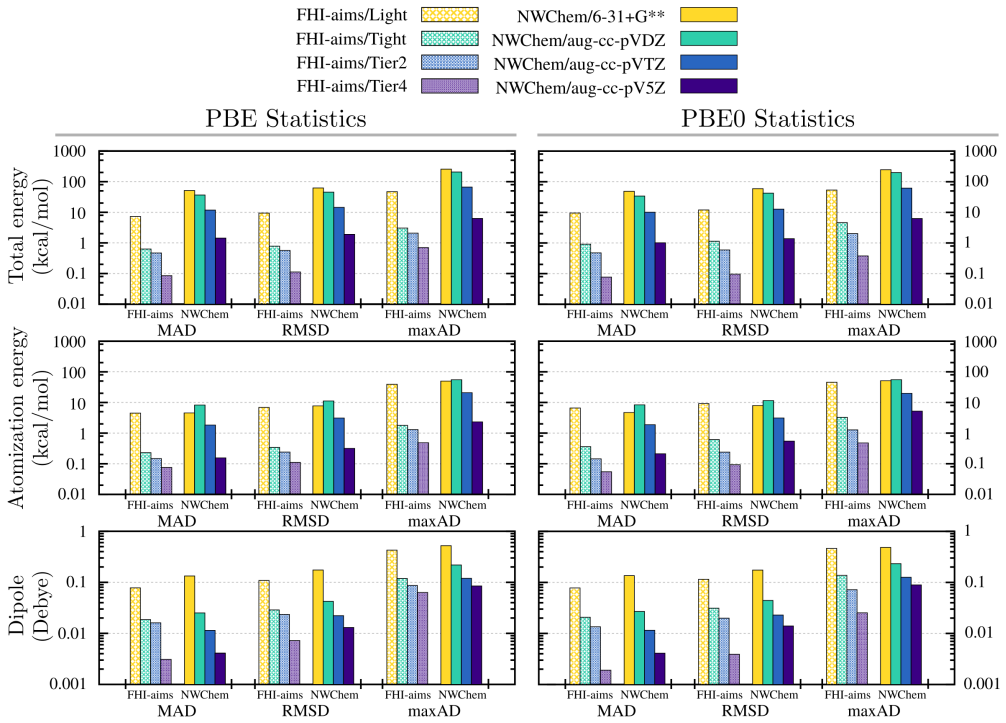

Figure 5.2: *GGA-PBE (left) and hybrid-PBE0 (right) deviations in total energy, atomization energy, and electrostatic dipole moment for the set of 210 molecules with respect to highly accurate values obtained using* MRCHEM. *MAD, RMSD and maxAD stand for mean absolute deviation, root mean square deviation and maximum absolute deviation, respectively. Results are included for two different DFT codes (*NWCHEM *and* FHI-AIMS *) and four bases each (ranging from light/standard to the largest available).*

The statistics of the error in total energy (top panel), atomization energy (middle panel) and electrostatic dipole moment (bottom panel) are shown in Fig 5.2 where MAD, RMSD and maxAD stands for Mean Absolute Deviation, Root Mean Square Deviation and Maximum Absolute Deviation respectively. The left panel refers to data obtained using the PBE functional and the right panel refers to data obtained using the PBE0 functional.

A recent study by Medvedev et. al. [69] indicate that the variational energy is not a good measure to judge the quality of the electronic density. Hence, dipole moments were included in our study which is a non-variational quantity. In addition the dipole moments helped to judge whether the different electronic codes converged to the same electronic ground state and not to a meta stable state. This was important in order to make a fair comparison among the different codes. In general it is difficult for a user to detect such inconsistency. In order to overcome this problem, initially different spin initialization of different molecules were probed to identify the correct ground state.

From the gathered pool of data the following conclusion can be drawn:

1. The total energies obtained by NAO(tier4) are more accurate then the GTOs(aug-cc-pV5Z) for the basis sets of similar size

2. Error cancellation in atomization energy is observed in both NAOs and GTOs. However, it is much more prominent in case of GTOs where the RMSD is lowered by a factor of 4-8 with respect to the total energies. The reduction factor in case of NAOs is about ~1.5-2. This cancellation effect is more stronger in case of the smaller basis sets. Here, again the NAOs are closer to the reference value than the GTOs for comparable basis set.

3. Both the PBE and the PBE0 functionals yield similar results. Hence, it can be concluded that the accuracy of different types of basis sets (NAOs and GTOs) will be similar for other functionals of the same type.

4. The dipole moments of the molecules are considered accurate if the error is less than 0.01 Debye [70]. Among NAOs and GTOs, only the largest basis set used in our study could achieve this target accuracy on average. The basis sets still had outliers whose errors were around 0.1 Debye.

5. As explained in last section, APW is not suitable for this kind of study due to convergence problems and heavy memory requirements. However, the atomization energies of a few molecules could achieve the chemical accuracy (1 kcal/mol) for which convergence was achieved in the limit of large box size.

5.5 Conclusions

To the best of our knowledge, this work presents the most accurate atomization energies calculated to date, for a large benchmark set of molecules. We conclude that moderately sized GTOs basis sets frequently used in quantum chemistry applications, suffer from average total energy errors much larger than 10 kcal/mol, and while very large GTOs basis sets yield the desired accuracy on average, there are still significant outliers. However, it may not always be feasible to employ such basis sets for systems much larger than those included in this study.

NAOs give much better accuracy even for moderately large bases ("tight" and beyond) since they can be constructed to possess the numerically correct behavior for a given exchange correlation functional, both in the nuclear as well as in the tail region. When feasible, APW based calculations achieve errors around ~1 mHa for total energies and ~1 kcal/mol for atomization energies. However, this level of convergence is difficult to reach for general molecular systems.

With our MWs results as reference, [58] it will be possible to unambiguously assess the accuracy of any given basis for the computation of total energies and atomization energies. This will help to shed light on the quality of the currently available basis sets, and the underlying reasons for their shortcomings. It will also guide towards the development of more accurate basis sets.

Another central conclusion of our work is that the basis set error can dominate over errors arising from the choice of exchange correlation functional under many circumstances, in particular if some of the most advanced and accurate functionals are used. Our results set therefore new standards in the verification and validation of electronic structure methods. We expect that results of this work and the method described will be used to assess the accuracy of all future developments in DFT methods.

5.6 Delta Test for Elemental Solids

Similar issue of accuracy and precision as discussed above also exists in the solid state community. A simple calculation of Si yields lattice constant which vary by more than 5 % using different pseudopotentials or DFT codes. In order to solve this, the DFT community came together for a collaborative effort for benchmarking different DFT codes, methods and pseudopotentials. The APW method is considered to be gold standard for the bulk systems. Hence the reference was generated using the Wien2k [71] DFT package which uses the APW methodology. The data set used in this study consists of ground state elemental solids of 71 elements. The equation of states of different elements obtained with different codes were compared and the difference between them is defined as delta factor [46]. The equation of state takes in to account the lattice constant, bulk modulus and its derivative. This test was done for 40 different pseudopotential families and codes. The tests for each code or pseudopotential was done by the experts of the code. This delta test was also included along with the tests on molecular systems as discussed above for benchmarking the new soft dual space Gaussian pseudopotentials.

6 Soft Norm Conserving PBE and PBE0 Pseudopotentials with Chemical Accuracy

New soft dual space Gaussian pseudopotentials [34, 43, 45] were generated for the PBE and PBE0 functionals by applying the softness penalty term. Not only the new pseudopotentials are soft, but accurate and transferable, as shown by the test of the molecular properties and the Delta test. The pseudopotentials generated for the PBE and PBE0 functionals have an absolute mean error of 1.38 kcal/mol in the atomization energy of the molecules where the reference values were obtained from the Multi-Wavelets(MWs) as discussed in chapter 5. As the pseudopotentials are soft and accurate, chemical accuracy could be achieved with less computational cost as compared to the medium sized basis sets. The PBE pseudopotentials were able to achieve all electron accuracy in case of the Delta test.

6.1 Introduction

Modern day research in material science has come to a stage where the computers can literally screen out materials of interest from a given pool of thousands of structures. It is often labelled "Material Discovery". These have been possible due to the development of the KS-DFT. A lot of approximation goes into the numerical solution of these KS equations for instance basis set, exchange correlation functionals, integration grids, Poisson solvers etc. In order to make sure the solutions of KS equations are reliable, it is important to estimate the errors arising due to these approximations. One of the important component of this machinery are the libraries of the pseudopotentials. The advantages of the pseudopotential method have been discussed in detail in chapter 3. Among desirable properties of a pseudopotential, some of the most important ones are the accuracy and transferability. For Material Discovery, the practitioners of DFT needs a pseudopotential which is transferable among systems with different chemical compositions while producing reliable accurate results. Deviation from this requirement will

result in incorrect physical and chemical properties of the material. This step is important as it assists the experimentalist in synthesis of the new materials.

Another important factor which limits the accuracy is the choice of the exchange correlation functionals. The errors associated with different exchange correlation functionals are well documented. Within a given exchange correlation functional, the other sources of error in a pseudopotential method other than the basis set is the pseudopotential itself. The pseudopotential is basically a model potential which is fitted to some reference values. Ideally the error from the pseudopotential can be reduced by fitting it to as many atomic configuration as possible. But, in practice this is possible only for few cases. Hence, in order to make the pseudopotentials reliable it is necessary to estimate the error of the pseudopotential within a given exchange correlation functional. But, for regular production runs, the pseudopotential should be soft. Hence, the pseudopotential needs to be soft, accurate and transferable.

New soft and accurate dual space Gaussian [43, 45] pseudopotentials have been generated for the PBE and PBE0 functionals. The methodology for the generation of these pseudopotentials is discussed in detail in chapter 4. The quality of these pseudopotentials is assessed through different tests as discussed in the following section.

6.2 Computational Setup for the Benchmark Calculation of the Pseudopotentials

6.2.1 Atomization Energy Calculation

For the assessment of the transferability and the accuracy of the pseudopotentials, the atomization energies of molecules and their electrostatic dipole moments were considered. The data set of the molecules and the reference values obtained using the MWs as discussed in chapter 5 is used for the tests of the pseudopotentials. The SCF runs were done using BIGDFT package [72]. BIGDFT is massively parallelized electronic structure code which uses the Daubechies Wavelets as its basis set. The evaluation of the exchange correlation functional in BIGDFT was done using the LIBXC library [24]. The input spin polarization of the atoms in the molecules were initialized such that they converge to the same ground state as found in the MWs. These input spin polarizations were obtained from the results of chapter 5. Minimization scheme was used for the SCF runs. Ground state of the single atoms, have been considered for computation of the single atom energies. In the ground state of the atoms, the eigenstates have integer occupations of the electrons. An $h_{grid} = 0.2$ a.u. is used, which is the spacing of the real space grid used in BIGDFT. These settings have been used for both the PBE and the PBE0 functionals.

6.2.2 Delta Test Calculation

Along with the atomization energies of the molecules, the Delta test of the elemental solids was also considered. The structure files of the elemental solids and the reference values for this test were obtained from the Delta package which is available in the website https://molmod.ugent.be/deltacodesdft. The reference values were calculated using the Wien2K [71] package. This test was conducted only for the PBE functional.

The KS equation of these systems was solved using the BIGDFT package [72]. For all the elements mixing calculation was done where electronic temperature was set to a low value of 10^{-5} Ry. The number of k points was decided based on the number of atoms in the unit cell. The h_{grid} was set to 0.3 a.u.. Other parameters were tuned such that an accuracy of 1 meV/atom is reached in the end. At present BIGDFT can only handle orthorhombic systems. So all the structures were converted to orthorhombic unit cell if the default structure file is not orthorhombic. In case of structures impossible to be converted, Quantum Espresso [73] package was used for such cases. Quantum Espresso package uses planewaves as its basis set. A program was written to convert the dual space Gaussian pseudopotential files to the UPF format used by Quantum Espresso. While using Quantum Espresso a large energy cutoff of 160 Ry was used. The post processing of the generated data was done through the Python scripts as provided by the Delta Package. For Quantum Espresso the LIBXC library was used for the evaluation of the exchange correlation potential and energy. More details about the setup can be found in Supplementary Information of Ref. [74].

6.3 Results

6.3.1 Softness of the Dual Space Gaussian Pseudopotential

The softness of the newly generated pseudopotentials can be easily shown in Fig 6.1. For the demonstration of softness, a nitrogen atom in a cubic box is considered. Here, h_{grid} represents the spacing between the grids which is used in the BIGDFT package. This can be considered equivalent to the energy cut off in planewaves i.e. a larger h_{grid} corresponds to a smaller energy cut off. The energy convergence with respect to the h_{grid} clearly indicates that the new NLCC pseudopotential is much softer than the older versions i.e. the ones generated by Krack[45] and Willand et. al.[34]. In order to achieve an accuracy of 10^{-4} Ha, $h_{grid} \approx 0.3$ a.u. is required for the older version of the dual space Gaussian type pseudopotential. However, with the new pseudopotential this accuracy can easily be reached for a $h_{grid} \approx 0.4$ a.u. This allows a significant speed up in simulations of large scale systems which are generally computationally expensive.

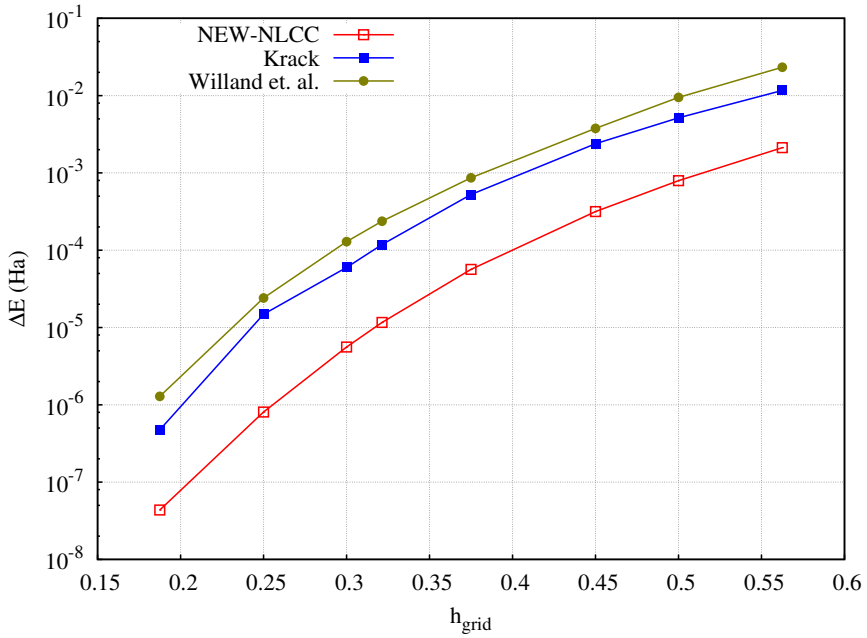

Figure 6.1: *Energy convergence of a nitrogen atom in a cubic box with respect to the h_{grid} for different versions of the dual space Gaussian pseudopotential.*

6.3.2 Errors in Molecular Properties Calculated with the Dual Space Gaussian Pseudopotentials

Atomization energy and electrostatic dipole moments of 167 molecules have been calculated with the newly obtained PBE and PBE0 dual space Gaussian pseudopotentials using BIGDFT [72]. These values have been compared against the most accurate reference obtained from MRCHEM as detailed in chapter 5. Errors in atomization energies for different molecules are provided in Fig 6.2 and Fig 6.3. From the plots it is clear that a large number of molecules have an error around 1-2 kcal/mol with some outliers. The goal of generating these pseudopotentials were to make them softer and at the same time accurate for production runs. For this purpose an accuracy of 2 kcal/mol is sufficient. These pseudopotentials give an absolute mean error of 1.38 kcal/mol for both the PBE and the PBE0 functionals. Highly accurate pseudopotentials of this family for PBE functionals have already been generated by Willand et. al. [34] which are harder than the new ones.

In addition the absolute errors in the electrostatic dipole moment is shown in Fig 6.4 and Fig 6.5. Interestingly the absolute mean error in dipole moments is about 0.0134 Debye for both the functionals which is quite accurate. This indicates that the solution of the KS equation for these given set of potentials are pretty good. The mean absolute deviation(MAD), root mean square deviation (RMSD), and maximum absolute deviation (maxAD) of the atomization energy and the electrostatic dipole moments for both the PBE and the PBE0 functionals are listed in Table 6.1. These values are comparable to the all-electron values obtained from using

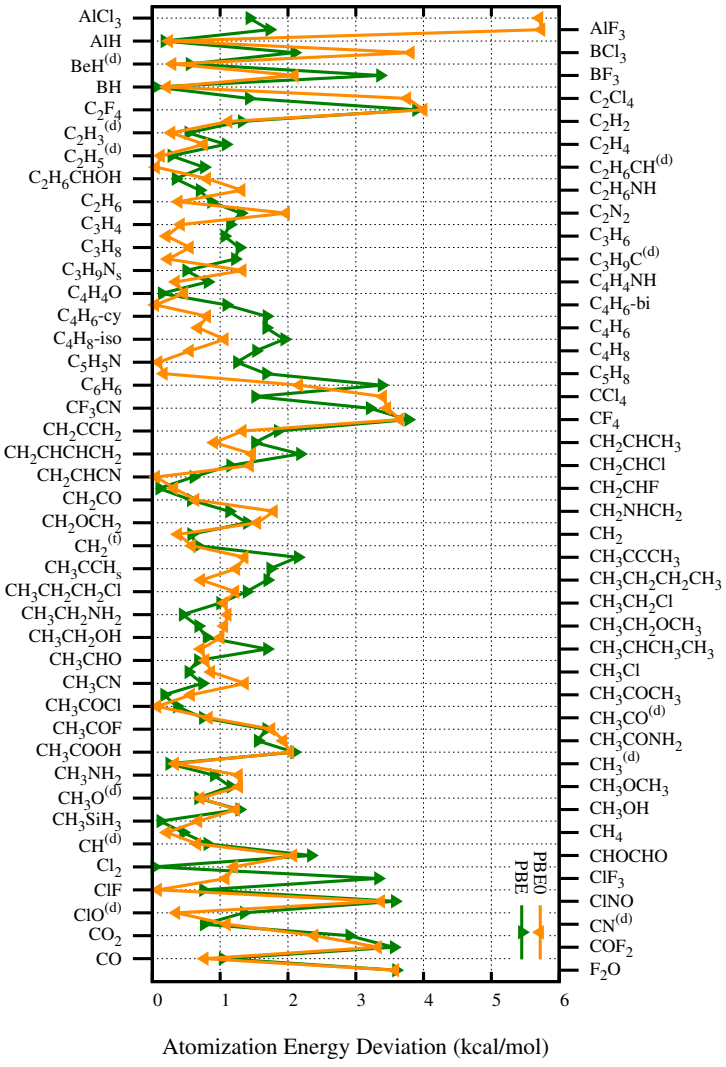

Figure 6.2: *Absolute error in the atomization energy of the molecules calculated with the PBE and PBE0 dual space Gaussian pseudopotentials using* BIGDFT *with respect to the absolute values of* MRCHEM.

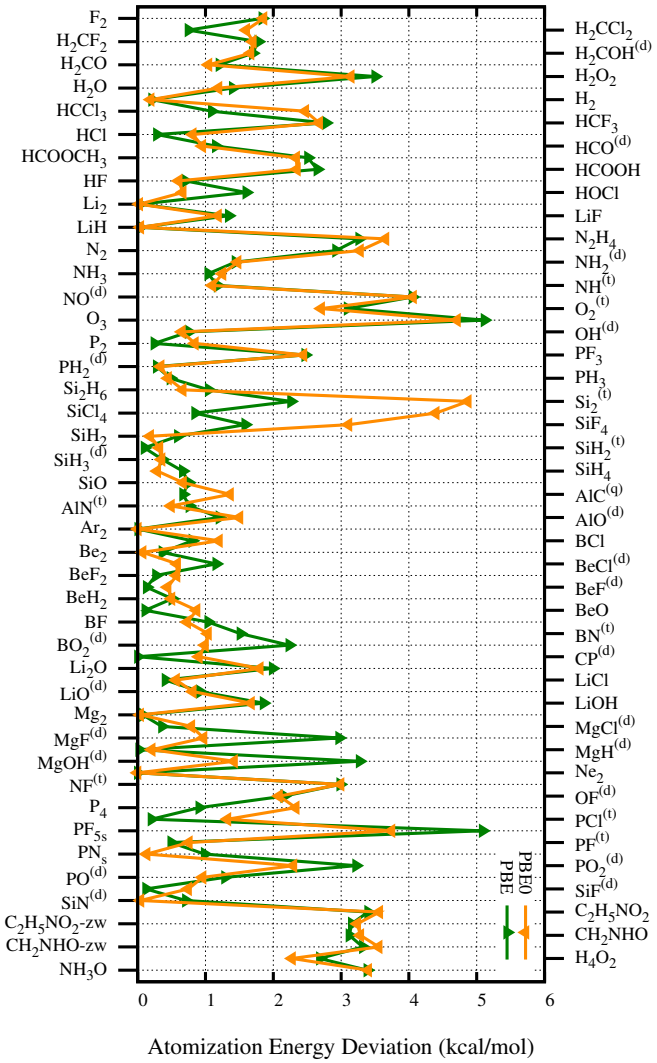

Figure 6.3: *Continuation of Fig 6.2*

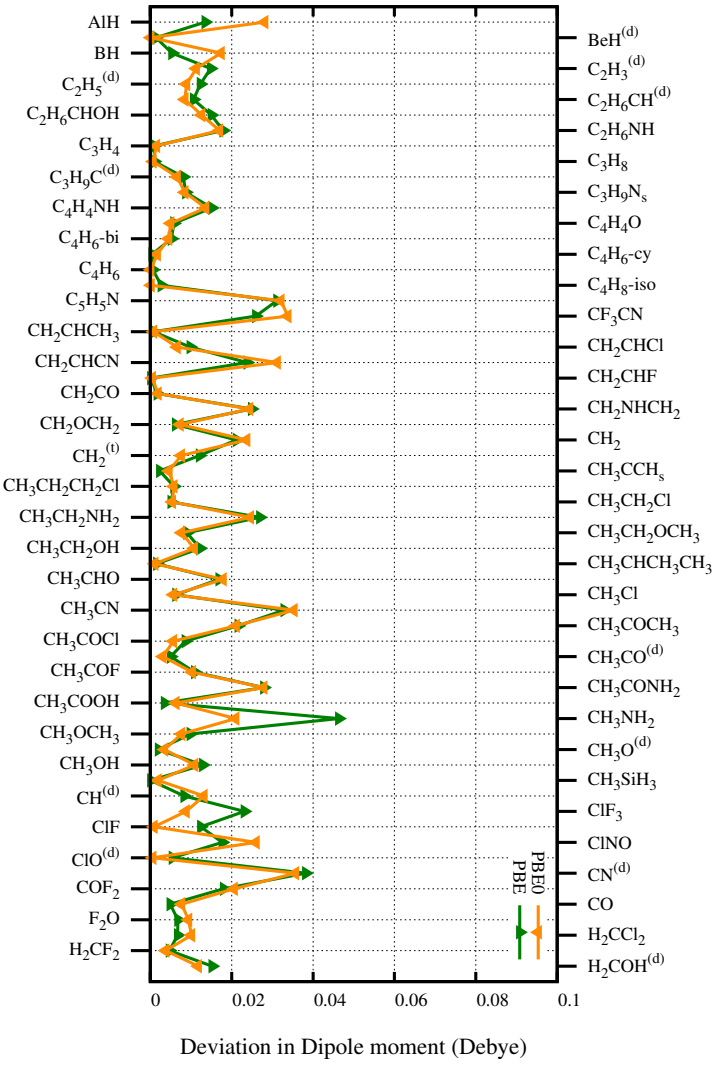

Figure 6.4: *Absolute error in the electrostatic dipole moment of the molecules calculated with the PBE and PBE0 dual space Gaussian pseudopotentials using* BIGDFT *with respect to the absolute values of* MRCHEM.

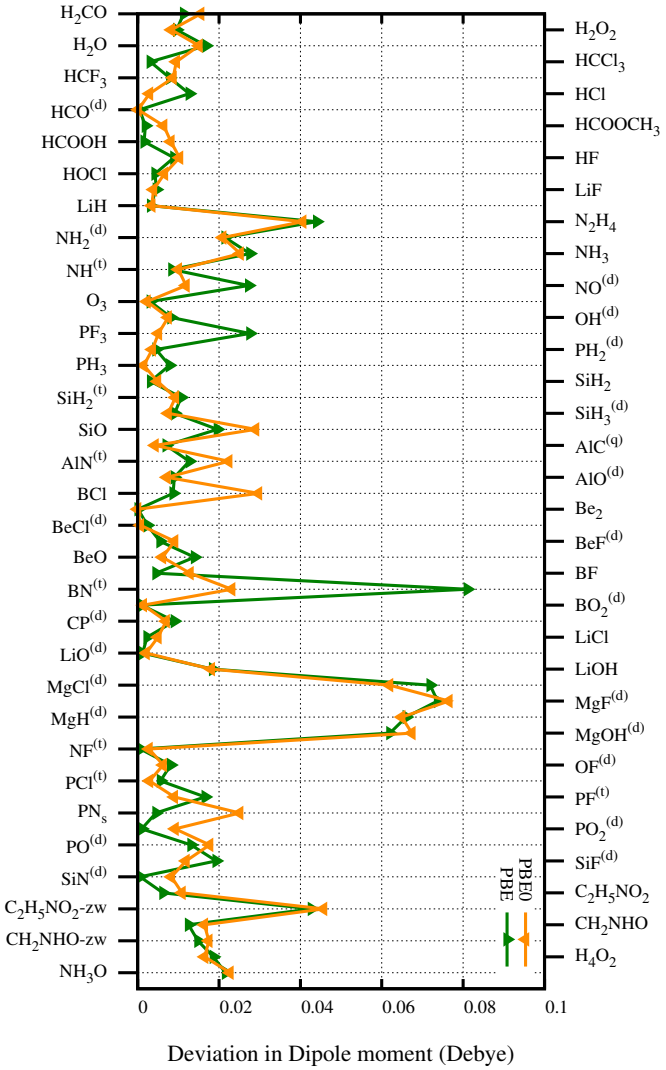

Figure 6.5: *Continuation of Fig 6.4*

medium size basis set. These results are better then the GTOs and are comparable to the NAOs for both the electrostatic dipole moments and the atomization energies.

	Atomization Energy (kcal/mol)		Dipole Moment (Debye)	
	PBE	PBE0	PBE	PBE0
MAD	1.38	1.38	0.0134	0.0131
RMSD	1.77	1.86	0.0203	0.0191
maxAD	5.74	5.11	0.0810	0.0765

Table 6.1: *Mean absolute deviation (MAD), root mean square deviation RMSD and maximum absolute deviation (maxAD) of the atomization energy errors and dipole moments of 167 molecules considered here. Calculations have been done using* BIGDFT

6.3.3 Delta Test of the Dual Space Gaussian Pseudopotentials for PBE Functionals

In the large community effort of benchmark and validation, we participated to perform the calculations for the delta test of the dual space Gaussian pseudopotentials. Delta test was already introduced in section 5.6. The accuracy of the pseudopotential is represented with a single value called "delta". A delta value of 2 is considered to be accurate enough for production calculations. The delta values of elements whose new pseudopotentials were generated are shown in the Fig 6.6. There is remarkable improvement with respect to the older version of the pseudopotentials which were very hard and performed badly in the Delta test in particular the heavy elements.

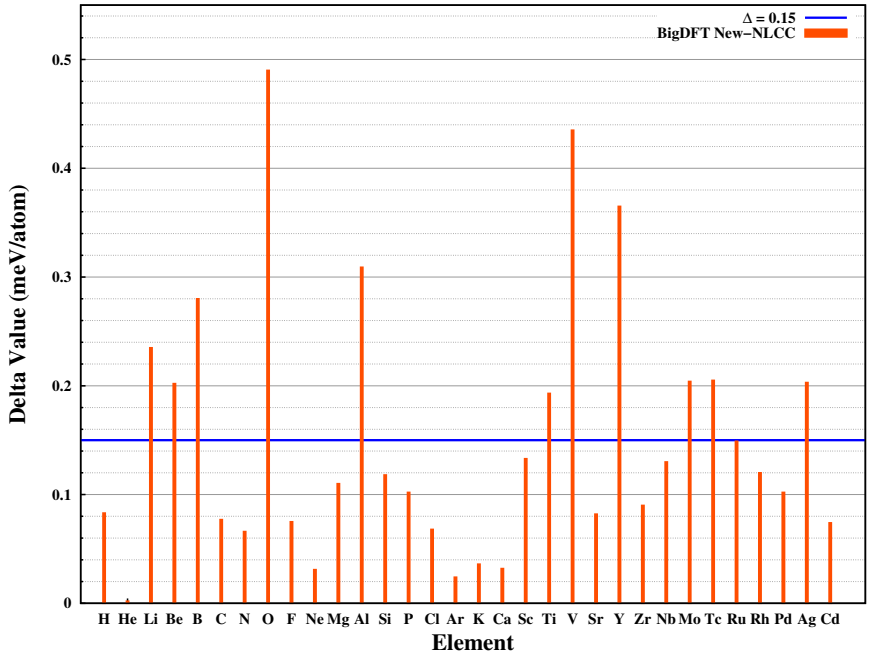

Figure 6.6: *Delta values of different elements obtained using the new HGH-NLCC pseudopotentials with PBE functional. The average delta value is represented by the blue line which corresponds to value of 0.15 which is close to the all-electron values. The maximum delta value is of oxygen which is around 0.5.*

The new pseudopotential of the light elements were able to achieve Delta values comparable to all electron calculation. It is also important to note that the relativistic pseudopotentials of transition metals were able to achieve all electron accuracy i.e. very small Delta value which was not possible with the dual space Gaussian pseudopotential generated by Krack [45]. The highest delta value is that of oxygen (0.49). In addition to good accuracy these new pseudopotentials are very soft as compared to older versions.

In Fig 6.6 pseudopotentials only for first few 3d transition metals are shown. The 3d transition metals have localized 3d orbitals which forces the d channel to have small projector radius.

Furthermore, due to spatial overlap, the semicore states are required for its better description. This makes generation of a soft pseudopotential for the 3d transition metals difficult.

6.4 Conclusion

New set of dual space Gaussian pseudopotentials have been generated for the PBE and PBE0 functionals. The Delta value of the elemental solids and the errors in the atomization energies and the dipole moments have been considered to judge the quality of the newly generated pseudopotentials. The following conclusions about the pseudopotentials can be drawn from the tests:

- The PBE and PBE0 dual space Gaussian pseudopotentials have an absolute mean error of 1.38 kcal/mol in the atomization energies and about 0.0135 Debye in electrostatic dipole moments. This accuracy is sufficient for regular production runs.
- The PBE pseudopotentials were able to achieve an average delta value of 0.15 which is comparable to all electron results.
- The newly generated pseudopotentials are much softer than the older versions.
- As these pseudopotentials are accurate in both the molecular systems and the elemental solids, it can be used reliably in any kind of system i.e. the pseudopotentials are transferable.

Therefore, these set of new pseudopotentials are soft, accurate and transferable.

7 Structure Prediction of Cages and Clusters

The ultimate goal of generating soft, accurate and transferable pseudopotential is to use them for study of structural and electronic properties of materials at a cheaper cost without sacrificing the accuracy of the results. This becomes important in case of large scale simulation like structure prediction of clusters or cage structures consisting of many atoms. The application of the newly generated pseudopotentials for structure predictions are discussed in this chapter.

7.1 Pseudopotentials applied to Different Problems

The new PBE pseudopotential generated were used for several applications. For some applications the pseudopotentials were specifically optimized. The publication which used these pseudopotentials are listed below:

1. *Interatomic potentials for ionic systems with density functional accuracy based on charge densities obtained by a neural network* Phys. Rev. B 92, 045131 (2015)

2. *Characterization of individual molecular adsorption geometries by atomic force microscopy: Cu-TCPP on rutile TiO_2 (110)* J. Chem. Phys. 143, 094202 (2015)

3. *Structure and optical properties of small $(TiO_2)_n$ nanoparticles, n=21-24.* submitted to J. Chem. Phys. (under review)

These new pseudopotentials were also used for the structure prediction of different clusters and cages. The investigation was carried out through minima hopping runs [75–79] and they are presented in the following sections.

7.2 Metastable Exohedrally Decorated Borospherene Cages B_{40}

The experimental discovery of borospherene, the only non-carbon fullerene observed in nature, has generated a lot of interest in the scientific community and led to the theoretical prediction of various endohedrally and exohedrally decorated borospherene. We apply Minima Hopping Method (MHM), a global geometry optimization algorithm at the density functional level to check the stability of recently proposed exohedrally decorated borospherenes $M_6@B_{40}$ for (M = Li, Na, K, Rb, Be, Mg, Ca, Sr, Sc and Ti). By performing short MHM runs, we find that the proposed fullerene structures are not global minima. Our new lowest energy structures are significantly deformed and of much lower symmetry. These low energy structures easily aggregate by forming chemical bonds when they are brought together. Exohedrally decorated borospherene is therefore not to be expected to be found as a building block of new materials that might have technologically useful properties.

7.2.1 Introduction

Considerable theoretical efforts are under way in nanosciences to find fullerene structures made out of non-carbon materials and numerous theoretical non-carbon structures can be found in the literature [80–84]. However, up to date nearly all experimentally discovered structures [85–94] are either pure carbon systems or are based on carbon fullerene skeletons, which are decorated by other elements or where one or more carbon atoms are replaced by other elements. Several theoretically proposed structures were shown to be metastable and to be much higher in energy than the ground state. As a consequence it is very unlikely that they could ever be synthesized. This was for instance the case for endohedrally doped Si_{20} fullerene [95] and the B_{80} fullerene [96–98]. A boron-carbon heterofullerene with boron patches was found to be the ground state instead of a configuration where the boron atoms are homogeneously distributed [83].

Boron (B_n) cages of different sizes have been proposed theoretically (n = 28, 38 and 40) [99–102]. After two decades of search a cage structure for (B_{40}^{-1}) was finally observed experimentally by Zhai et. al. [102] together with a quasi planar structure. Calculations assigned a lower energy to the quasi planar structure. However, according to the same kind of theoretical calculations, the ground state of neutral B_{40} has a cage like structure. It has a fullerene structure with D_{2d} symmetry consisting of two planar hexagonal and four non-planar heptagonal rings. This ground state structure is 0.5 eV lower in energy than the second minimum [102]. The quasi planar structure is the fifth lowest in energy with an energy difference of 1 eV. The discovery of the borospherene has generated a lot of interest in the scientific community. An important difference to C_{60} has however to be noted. Carbon fullerenes attract each other only by weak van der Waals forces, but do not form covalent bonds among each other. As already noted by Zhai [102], B_{40} is expected to be highly reactive [96, 103] and should therefore form covalent bonds with adjacent borospherenes, destroying its original fullerene shape. The results presented in this paper confirm this expectation.

Since, the discovery of borospherene, a large number of decorated borospherene structures has been proposed theoretically primarily for applications in hydrogen storage. The decoration of B_{40} can be classified by the type of adsorbate atoms (adatoms), which can be an alkaline metal, earth alkaline metal or transition metal. Bai et. al. [104] performed minima hopping based structure predictions for endohedral M@B_{40} (M = Ca, Sr) and exohedral M@B_{40} (M = Be, Mg). Fa et. al. [105] found endohedral M@B_{40} (M = Na, Ba) to be stable. Jin .et. al. [106] investigated endohedral M@B_{40} (M = Sc, Y, La) and observed that they have strong binding energies and may thus exist in nature. Hydrogen adsorption studies on Li decorated B_{40} by Bai et. al. [107] predict that H_2 storage can be increased from 7.1 wt% in Li_6B_{40} to 13.8 wt% in $Li_{14}B_{40}$. The theoretical studies of Liu et. al. [108] showed that exohedrally decorated B_{40} with six alkaline metal atoms (AM = Li, Na, K) is stable and could achieve a hydrogen storage capacity of 8 wt%. Tang et. al. [109] predicted Sc decorated B_{40} to be stable through short molecular dynamics simulation. Based on a study of single metal atom adsorption energies, Dong et. al. [110] proposed a B_{40} fullerene decorated with six titanium atoms as a promising candidate for hydrogen storage. In all the above mentioned theoretical $B_{40}M_6$ structures, the six adatoms are centered in the two hexagons and four heptagons of the bare B_{40} fullerene.

However, in none of these later studies systematic structure predictions were performed. By performing structure predictions, we will show in this contribution, that the B_{40} fullerene decorated with six alkaline metal, earth alkaline metal or transition metal atoms is only a metastable structure and that there are other disordered structures which are considerably lower in energy. These low energy structures are in addition highly reactive and form bonds when brought into contact with each other. Hence it is extremely unlikely that bulk materials formed by metal decorated B_{40} fullerenes can be synthesized.

7.2.2 Computational Methods

The scanning of potential energy surface (PES) of these decorated B_{40} cages was carried out using the Minima Hopping method (MHM) [75–79] as implemented in BIGDFT [72] package at the density functional level of theory. The MHM is an algorithm to explore the PES of a polyatomic system in an unbiased efficient manner. The MHM consists of two parts. In the first part short molecular dynamics trajectories are performed to cross barriers between minima followed by local geometry optimizations. In the second part the new minimum is accepted or rejected based on energy difference and structural similarity criteria [111]. BIGDFT is massively parallel electronic structure code which uses Daubechies wavelets as basis set and gives extremely short times to solution on parallel computers. The atoms were described using the new soft norm conserving HGH pseudopotentials [34, 45] with a non-linear core correction. The exchange correlation interaction of the electrons were described through generalized gradient approximation with the Perdew-Burke-Ernzerhof (PBE) [10] functional. The calculations was carried out with free boundary conditions. The convergence parameters were set such that the total energy converged within 10^{-5} eV and the structure was relaxed until the maximum force component of any atom was less than 1.0 meV/Å.

For the calculation of total energies with hybrid functionals PBE0 [14] and B3LYP [9, 12, 15, 16], the FHI-AIMS [64, 112–115] all electron code was also used which uses numerical atomic orbitals as basis set. The tier2 basis set was used. The SCF convergence criteria set was 10^{-6} eV for total energy, 10^{-6} eV for eigenvalues and 10^{-6} a.u. for charge density. Free boundary conditions were used in FHI-AIMS calculations.

For calculating the dimerization energy the structures are placed side by side and geometrically relaxed. The PBE exchange correlation functional was used. This calculation has been carried out using BIGDFT. The LIBXC [24] library was used for the calculation of the functionals.

7.2.3 Results and Discussion

In this work we study the PES of borospherene $M_6@B_{40}$ decorated with six metal atoms. We consider alkaline metals (Li, Na, K, Rb), earth alkaline metals (Be, Mg, Ca, Sr) and transition metals (Sc and Ti) in our study.

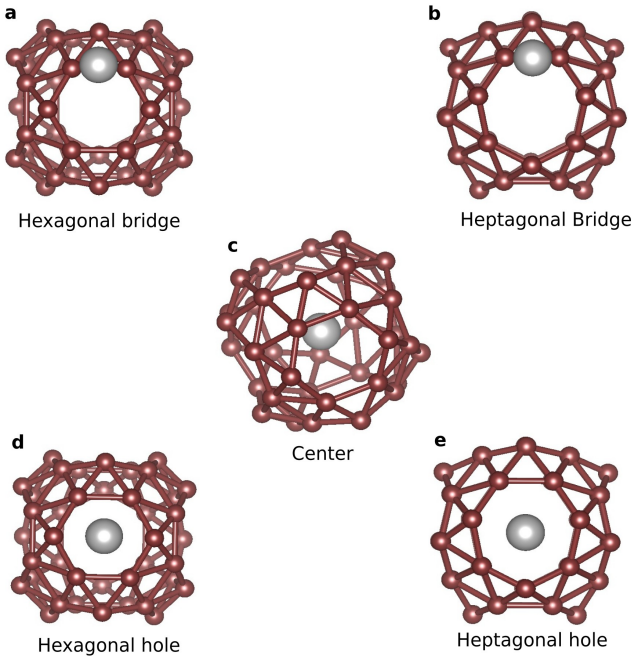

Figure 7.1: *The adsorbate atom, represented by a grey sphere, can be placed on five different positions in the borospherene (B_{40}) represented by brown spheres. The five different sites are (a) on the B-B bond of the hexagonal ring, (b) on the B-B bond of the heptagonal ring, (c) center of the cage, (d) hexagonal hole and (e) heptagonal hole*

Before discussing the six-atom decorations of the B_{40} cage, let us briefly address the single adatom case. A single adatom can sit in the center of the cage, centers of the hexagons and

heptagons or on the B – B bridge of the hexagonal/heptagonal rings as shown in Fig 7.1.

$$E_{bind} = -[E_{M@B40} - E_M - E_{B40}] \tag{7.1}$$

The binding energy (B.E.) of a single adatom on B_{40} for different metal atoms and for different positions are obtained using the eq. (7.1) where E_M represents the energy of an isolated metal adatom, E_{B40} the energy of an isolated B_{40} cage and $E_{M@B40}$ the energy of the decorated cage.

	CENTER (eV)	HEX (eV)	HEPT (eV)	HEX B-B (eV)	HEPT B-B (eV)
$Be@B_{40}$	-	3.168	3.141	-	-
$Mg@B_{40}$	0.069	1.093	1.050	-	-
$Ca@B_{40}$	3.776	2.520	2.655	-	-
$Sr@B_{40}$	13.167	11.666	11.746	-	-
$Li@B_{40}$	1.796	2.112	2.254	-	-
$Na@B_{40}$	1.683	1.546	1.582	-	-
$K@B_{40}$	1.675	1.714	1.764	-	-
$Rb@B_{40}$	1.017	1.670	1.714	-	-
$Sc@B_{40}$	5.171	3.906	4.543	-	2.091
$Ti@B_{40}$	9.466	9.089	9.257	6.815	6.775

Table 7.1: *The binding energy (in eV) of the single adatom to different sites of the B_{40} for the PBE exchange correlation fuctional. These calculations have been carried out using* BIGDFT *for free boundary conditions. The headings CENTER, HEX and HEPT represents the center, hexagonal hole and heptagonal hole of the borospherene respectively. HEX B-B and HEPT B-B represent the B-B bond belonging to the hexagon and heptagon ring respectively.*

The B.E. trends for different adatoms at different positions are shown in Table 7.1. During a geometry relaxation Li, Be, Mg, Sc and Ti take on an off center position inside the cage and come close to either hexagon or heptagon holes whereas Na, K, Rb, Ca and Sr are stable at the center of the cage. The alkaline metals and earth metals are unstable at the B – B bridge of the hexagon/heptagon. Upon relaxation the adatom positioned on the B – B bridge moves to the hexagon/heptagon holes. A titanium atom is stable on both the hexagonal and heptagonal B – B bridge whereas Sc is stable only on the heptagonal B – B bridge. Among the earth alkaline metals, the hexagonal hole is energetically more favorable for Be and Mg whereas for Ca and Sr, the most stable site is the center of the borospherene. All the alkaline metals prefer the heptagonal hole except Na which prefers the center. The transition metals (Sc and Ti) are most stable at the off-center position inside the borospherene cage.

For six adatoms the number of possibilities of decorating the B_{40} is too large to be mapped out systematically and chemical intuition typically fails to predict completely new structures. In order to check the stability of $M_6@B_{40}$ cages we therefore use a systematic and unbiased structure prediction method, namely the Minima Hopping Method (MHM) [75–79] as implemented

in the BIGDFT [72] package. The PBE functional [10] is used in all these runs.

As an input guess for the MHM runs, we placed the adatoms in the hexagonal and heptagonal centers of the perfect fullerene as these prototype structures were found to be stable in recent publications [107, 108, 110]. All the MHM runs gave very soon deformed cages that were lower in energy than the initial fullerene structure. The deformed structures often lost their characteristic hexagon-heptagon patterns and are shown in Fig 7.2. These deformed structures have rings containing between 6 and 10 boron atoms. The initial guess structure of adatoms on hexagonal and heptagonal rings of borospherene were found to be local minima except for Be. For earth alkaline metals, i.e. Mg, Ca, Sr, the lowest energy structures had randomly arranged rings with 7-10 atoms. In case of alkaline metals, the lowest energy structures of Li, Na, K, Rb decorated B_{40} had rings with 6-8 borons. The Sc and Ti decorated lowest energy structures had rings with 5-9 borons.

In Ref.[116] it was shown that the PBE functional gives a reasonable description of boron clusters, but cannot however always predict the correct energetic ordering between different structures. For this reason the stability of the deformed cages was further assessed by recalculating the energy differences between the lowest energy structure found and the perfectly decorated cage structure with the PBE0 [14] and B3LYP [9, 12, 15, 16] functionals using the all electron FHI-AIMS [64] code. We also compared the PBE level pseudopotential results obtained from BIGDFT with the all electron results obtained with FHI-AIMS and found that they are in close agreement. The energy difference between the lowest energy structure and perfect fullerene structure agree within 200 meV. The data of Fig 7.3 show that also the two other functionals predict our structures found on the PBE level to be lower in energy than the perfect cage. This indicates that even in gas-phase, it is unlikely to get an intact fullerene structure.

It is also interesting to notice that clustering of the metal atoms was never observed during our short MHM runs. This may be explained by the relatively strong binding of the metal atoms to the boron skeleton. This in in contrast to the case of C_{60} where lower binding energies leads to clustering. Since the cages are deformed and disordered, they are unlikely to form building block for larger structures.

To study the reactivity of the deformed metal decorated B_{40} cages we brought two units in close contact and performed a geometry optimization to obtain the dimerization energy which is defined as eq. (7.2) where E_{mono} and E_{dimer} are the total energies of the monomer and dimer respectively.

$$E_{DE} = -[E_{dimer} - 2E_{mono}] \tag{7.2}$$

Here the monomers are the lowest energy structures. The D.E. for different cases are shown in the Fig 7.4. For pure B_{40} , the geometry is relaxed by placing the two cages along the hexagonal and heptagonal rings. Our calculation for B_{40} dimers shows that they form strong covalent

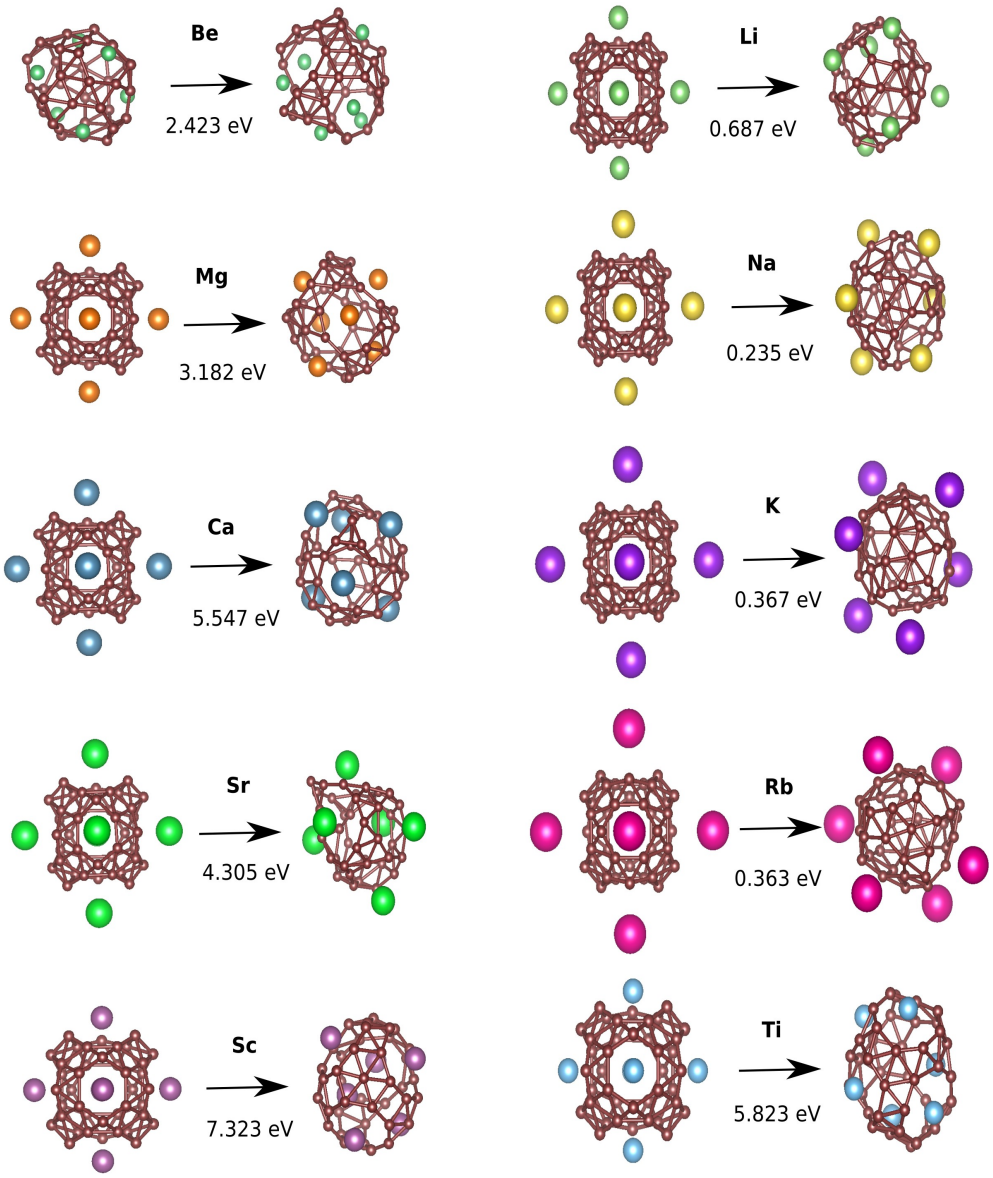

Figure 7.2: *The first and third columns show the perfectly decorated cage structures of borospherene with different adsorbates: alkaline, earth alkaline and transition metals. The second and fourth columns represent the lowest energy structure found in minima hopping runs. Brown spheres represent boron atoms and the other colours various metal atoms. The energy difference (in eV) between the lowest energy structure and the initial decorated borospherene is also shown for PBE exchange correlation functional.*

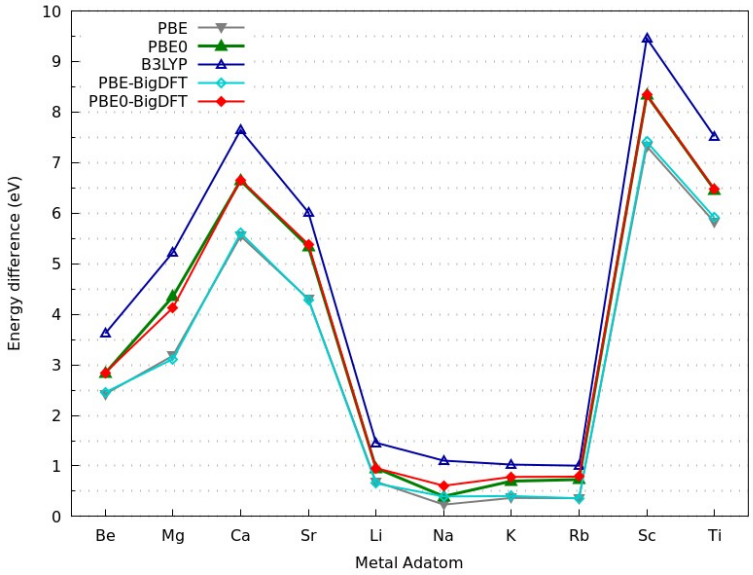

Figure 7.3: *The energy difference (in eV) of the perfect cage with respect to the lowest energy structure of $M_6@B_{40}$ for different adatoms calculated with different exchange correlation functionals and two different codes, namely* FHI-AIMS *and* BIGDFT. *Unless specified the calculations were done with the* FHI-AIMS *code.*

bonds along the heptagonal rings releasing 0.656 eV. However, dimerization through hexagonal rings is energetically not favorable. For the decorated M_6B_{40}, the D.E. is larger than the pure B_{40}.

To summarize, our investigations of the PES of the exohedrally decorated B_{40} cages reveal that the highly symmetric configurations obtained by positioning metal adatoms on high symmetry sites of the perfect borospherene cage are metastable. In a global geometry optimization runs, they distort to form structures with rings of various sizes, losing thereby symmetry. Earth alkaline and transition metals decorated B_{40} have a large energy gap between the lowest energy structure and the fullerene structure.

The D.E. indicate that they form strong bonds and are chemically reactive. All these results suggest that theoretically postulated decorated structures of B_{40} are not realizable as building blocks for applications such as hydrogen storage. More generally these findings show that structures obtained by chemical intuition are frequently not ground states and that performing unbiased global geometry optimization is essential to make reliable structure predictions.

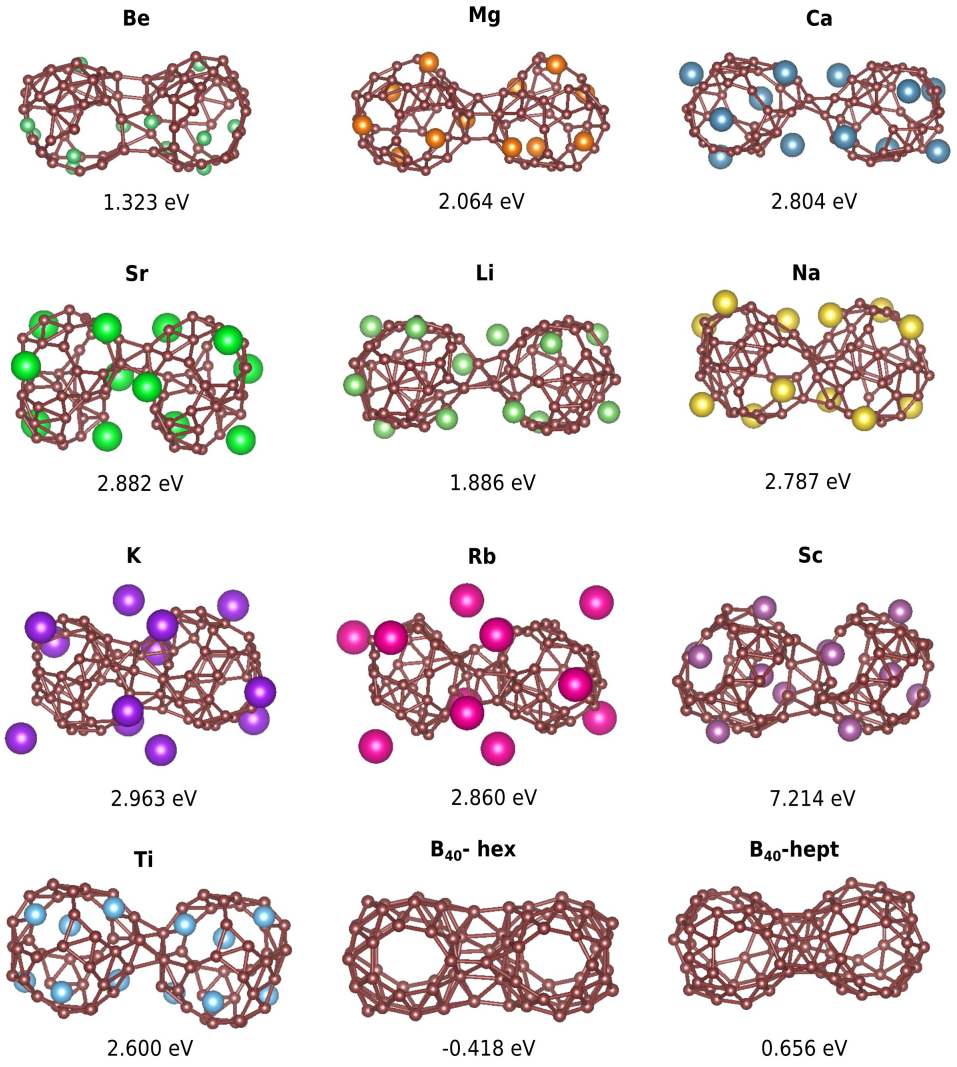

Figure 7.4: *The relaxed structures of dimers made from the lowest energy structures of different M_6B_{40} and B_{40} together with their dimerization energy (in eV). All the calculation have been done using* BIGDFT *and the PBE exchange correlation functional. B_{40}-hex represents dimer formed along the hexagonal rings and B_{40}-hept represents dimer formed along heptagonal rings.*

7.3 Theoretical prediction of $\{Si(NH)_{0.5}O_{1.5}\}_n$ (n=20,24) Fullerene

Fullerene [117] and fullerene based materials are important for development of new technologies in nanosciences. Their stability and inert nature makes them special. No substitute have been found for fullerene despite a large number of theoretical predictions of new structures. This is due to the fact that most of the predicted structures are reactive and metastable. Through systematic search of potential energy landscape at density functional level of theory, polyatomic $\{Si(NH)_{0.5}O_{1.5}\}_n$ (n=20 and 24) cages were found to be putative global minima. Dimerizaton energy study of these cages clearly show their inert nature. They posses all the necessary qualities to be stable and nonreactive as fullerene. We hope that these structures will generate interest among experimentalists and may serve as building block for nanostructures.

7.3.1 Introduction

The electronic industry at present is primarily based on silica based structures. Search of new materials have received renewed interest in the past decade as miniaturization of devices is reaching the structural limit. Among them, the nanostructures of carbon [117, 118] have received a huge attention due to their unique properties. Numerous efforts are undertaken to find other non-carbon fullerene structures.

Extensive theoretical and experimental studies are available on silica based nanostructures such as clusters, cages, nanotubes and nanowires [82, 119–124]. These structures possess desirable mechanical, electronic and optical properties for applications and can be tuned by varying their size and shape. Though significant progress have been made in the experimental study of silica nanotubes, a large gap remains for the systems like cages and clusters. Silica clusters generated in laser beam experiments are often short lived. However, through DFT studies [119] it was found that the silica clusters with full coordination are more stable than the ones which have uncoordinated ends. Bromley [82], through theoretical investigation of nanocages, nanotubes and nanoclusters of different sizes (n = 12, 18 and 24) of silica $(SiO_2)_n$ found that with increasing cluster size, fully coordinated cage structure becomes more stable than other morphology and may be experimentally realizable. Based on this work, Zhang et. al. [124] constructed a family of fully coordinated silica cages (for n = 20, 24, 28, 36 and 60) which are found to be energetically stable through B3LYP [9, 12, 15, 16] calculations.

In the literature a large number of theoretically proposed structures can be found [80–84, 96, 98]. However, only a handful have been realized experimentally. Most of these theoretically proposed structures are metastable and reactive. They are prone to aggregation i.e. they form strong bonds when they come close together. The stability of the nanostructures are often judged by (i) the energy gap between the structures, (ii) HOMO-LUMO gap, and (iii) the binding energy. For any proposed structure to act as building block, on top of above mentioned criteria, it should be strongly resistant to aggregation. For example the silica nanocages studied in Ref [125] spontaneously forms dimer. This makes it difficult to synthesize the structures. This may explain why among the multitude of theoretically predicted structures only cage

structures of fullerene and B_{40} [102] have only been observed experimentally till date.

Based on the above discussed criteria through our DFT investigations we predict new silica based cage structures which have features similar to those of fullerenes. These cage structures are found to be putative global minima and have large HOMO-LUMO gaps. They have strong resistance to aggregation and form weak bonds between the cages. Hence, they may act as basic building blocks of larger structures. These new cage structures are obtained by chemical substitution of certain O atom with NH group of silica cages $(SiO_2)_n$ of size n=20 and n=24. For later reference $\{Si(NH)_{0.5}O_{1.5}\}_{20}$ and $\{Si(NH)_{0.5}O_{1.5}\}_{24}$ are referred as SiNHO-20 and SiNHO-24 respectively. The silica structures of $(SiO_2)_{20}$ and $(SiO_2)_{24}$ are referred as SiO-20 and SiO-24 respectively. Structure of SiNHO-20 and SiNHO-24 are in general referred as SiNHO and SiO-20 and SiO-24 as SiO. In the following text "cage" refers to the cage structure of SiNHO-20 and SiNHO-24 unless explicitly mentioned.

7.3.2 Computational Methods

The Minima Hopping Method (MHM) [75–79] has been employed for the unbiased and efficient potential energy surface (PES) search of the SiNHO-20 and SiNHO-24 clusters as implemented in BIGDFT [72] package which uses Daubechies wavelets as its basis set. The details of the MHM is discussed in section 7.2.2. The calculation is carried out at the PBE [10] level of theory. The atoms are described through the new soft norm conserving HGH type pseudopotentials [34, 42, 45] consisting of non linear core correction. The parameters were tuned such that the total energy converged to 10^{-5} eV and the maximum component of the force was less than 1 meV/Åat convergence of relaxation.

The cohesive energy (C.E.) of these structures have been calculated which is defined as

$$E_{coh} = [E_{struc} - n_{Si}E_{Si} - n_N E_N - n_O E_O - n_H E_H] \tag{7.3}$$

where E_{Si}, E_N, E_O, E_H, E_{struc} are the total energy of silicon, nitrogen, oxygen, hydrogen atom and the structure respectively. The n_{Si}, n_N, n_O and n_H represents the number of silicon, nitrogen, oxygen and hydrogen atoms present in the structure.

The dimerization energy (D.E.) is defined as

$$E_{DE} = [E_{dimer} - 2E_{mono}] \tag{7.4}$$

where E_{mono} and E_{dimer} are the total energies of the monomer and the dimer respectively. Here the monomer is the lowest energy cage structure. The dimer is obtained by bringing two cages close together and relaxing them. The D.E. calculation was done using BIGDFT using the same set of parameters as mentioned above for the PBE functional. The distance between the cages is defined as the distance between the center of mass of the two individual cages.

Different properties like the C.E., the electrostatic dipole/quadruple moment and the HOMO-

LUMO gap are also evaluated for the PBE functional. The HOMO-LUMO gap for the PBE0 [14] functional was calculated using FHI-AIMS [64, 112–115], an all-electron code which uses numeric atomic orbitals as its basis set. Tight basis settings were used for these calculations. The SCF runs were continued until the total energy converged to 10^{-6} eV, eigenvalue to 10^{-4} eV and charge density to 10^{-5}. All the calculations in BIGDFT and FHI-AIMS were done with free boundary conditions. The LIBXC library [24] was used for the evaluation of exchange correlation functionals.

7.3.3 Results

Design principle

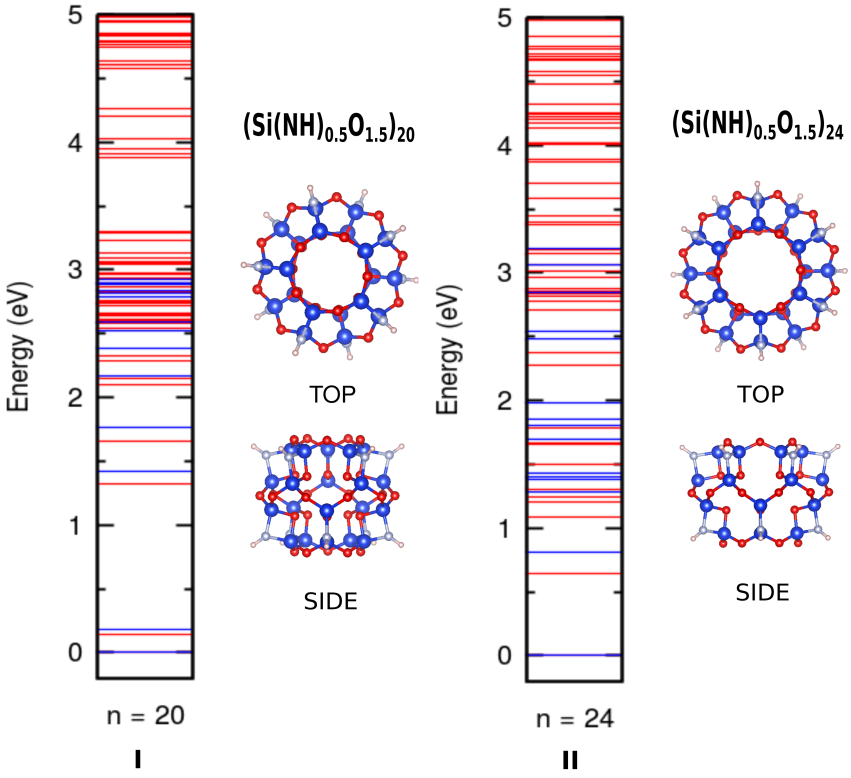

Figure 7.5: *I and II represents the energy spectrum of* $\{Si(NH)_{0.5}O_{1.5}\}_{20}$ *and* $\{Si(NH)_{0.5}O_{1.5}\}_{24}$ *clusters, respectively for both the PBE (red colour) and PBE0 (blue colour) functionals. Beside the energy spectrum plot the top and side view of the lowest energy structure of the corresponding cluster size are shown. In the structure, the Si atom are represented by blue spheres, O by red spheres, N by grey spheres and H by pink spheres. The structures and energies have been calculated using the PBE functional in* BIGDFT. *The PBE0 calculations were done using* FHI-AIMS.

In our investigation we considered fully coordinated silica cages of SiO-20 and SiO-24 proposed by Zhang et. al [124]. SiO-20 has a D_{5d} symmetry consisting of 12 five membered rings (MRs). The SiO-24 consists of 2 six MRs and 10 five MRs and has D_3 symmetry. Each Si is bonded to 4 oxygen atoms arranged in tetrahedral symmetry. The silica cages in general have natural tendency to form dimers spontaneously through siloxane bridges [125]. We show later through calculations that this holds true also for the SiO-20 and SiO-24 cages. This natural tendency of spontaneous dimerization indicate that they might be difficult to synthesize. Based on this information we propose new structure (SiNHO-20 and SiNHO-24), obtained by replacing certain O atoms (25 % by stoichiometry) with NH group as shown in Fig 7.5. After a geometry relaxation it was found to be local minimum. However, geometry relaxations of the NH_2 substituted structure leads to distorted cage structure.

Potential Energy Surface Profile

Simple geometry relaxation of the structure is not enough to justify its stability. There may exist other structures in its PES which are lower or closer in energy to the proposed structure. We apply the MHM algorithm to scan its PES. The MHM runs resulted in a large pool of structures for both SiNHO-20 and SiNHO-24. The energy spectrum of the PES of these polyatomic cages are shown in Fig 7.5. In the PES search, both SiNHO-20 and SiNHO-24 cages were found to be the lowest energy structure. Most of the other structures obtained were distorted cage structures with randomly arranged NH groups or NH_2 groups with uncoordinated N or O bonds. For SiNHO-20 the second lowest energy structure was found to be 0.16 eV and 0.18 eV higher than the cage structure for the PBE and the PBE0 functionals respectively. Similarly for SiNHO-24, the energy difference between the lowest energy structure and the second lowest energy structure are 0.65 eV for the PBE and 0.8 eV for the PBE0 functionals. In general in our study we found that the energy gap between the structures increases while using the PBE0 functional instead of the PBE functional. Interestingly in both cases, the second lowest energy structure has the intact cage structure with exchanged O and NH groups. The other structures are much higher in energy (> 1 eV) with respect to the proposed cage structure.

Energetic and Electrostatic Properties

Apart from the PES, the stability of SiNHO-20 and SiNHO-24 cages was assessed through other properties like the cohesive energy and the HOMO-LUMO gap. Different properties of the first five lowest energy structures of both sizes SiNHO-20 and SiNHO-24 computed for PBE functional and HOMO-LUMO gap for PBE0 functional are listed in the Table 7.2.

The cohesive energy (C.E.) of pure silica cages SiO-20 and SiO-24 are found to be -13.4175 Ha and -16.1667 Ha respectively. However, the SiNHO-20 and SiNHO-24 cages have lower cohesive energies which is calculated using the eq. (7.3). These observation also holds for the other low energy structures. The E_{coh} of second lowest energy structure of SiNHO-20 is quite close to the first (0.0053 Ha) unlike the case of SiNHO-24 (0.25 Ha). As PBE in general under

Structure no	$E_{cohesive}$ (Ha) PBE	HOMO-LUMO Gap (eV) PBE	PBE0	Dipole Moment (Debye)	Quadrupole Moment (eÅ^2) Q_{xx}	Q_{yy}	Q_{zz}
n=20							
$(SiO_2)_{20}$	-13.4175	4.61	7.38	0.0000	-1.8279	-1.7237	3.5517
1st	-14.3074	4.25	6.75	0.0000	-4.6375	2.2596	2.3780
2nd	-14.3021	4.47	6.96	3.0605	-14.8321	-0.9980	15.8302
3rd	-14.2587	3.32	5.66	7.3135	-16.0653	-15.1491	31.2132
4th	-14.2464	3.61	5.94	5.5935	-17.4696	-10.0673	27.5372
5th	-14.2302	4.28	6.78	4.1508	-16.4106	1.8070	14.6037
n=24							
$(SiO_2)_{24}$	-16.1667	4.89	7.66	0.0004	-3.0168	-3.0024	6.0192
1st	-17.2302	4.42	6.89	0.0008	-2.5420	1.2171	1.3248
2nd	-17.2064	3.99	6.41	4.8393	-19.3576	6.5193	12.8383
3rd	-17.1902	4.22	6.79	8.2961	-36.7088	6.6764	30.0324
4th	-17.1860	4.16	6.57	4.6301	-20.2580	7.3360	12.9220
5th	-17.1845	3.98	6.40	4.2136	-15.5466	6.3919	9.1546

Table 7.2: *The cohesive energy, HOMO-LUMO gap, electrostatic dipole and quadrupole moment of the $(SiO_2)_{20}$, $(SiO_2)_{24}$ cages and the first five low energy structures of $\{Si(NH)_{0.5}O_{1.5}\}_n$ cluster of size n=20 and n=24 for the PBE functionals and HOMO-LUMO gap for the PBE0 functional. The cohesive energy is defined here as the difference between the energy of the structure and energy of its constituent atoms in isolation. The magnitude of the dipole moment and the eigenvalues of the diagonalized quadrupole moment matrix are reported here. All quantities are estimated using* BIGDFT *except the HOMO-LUMO gap for PBE0 functional which is calculated using* FHI-AIMS.

estimates the band gap, the HOMO-LUMO gap was also calculated using the PBE0 functional. The calculations were done using FHI-AIMS, an all electron code. Silica bulk structures have typically large band gap for e.g. alpha quartz the most stable phase of silica has a band gap of 9 eV. Silica cages SiO-20 and SiO-24 also have typically large HOMO-LUMO gaps which are close to the bulk value. The large PBE and PBE0 HOMO-LUMO gap of SiNHO cages also supports their superior chemical stability. But the trends of C.E. and HOMO-LUMO gap of SiO and SiNHO cages are not synchronous. Hence, it is difficult to conclude which one is more stable. Both of them have large gaps and C.E.. The only conclusive remark that can be made at this point is that both of them are chemically stable.

Dimerization Energy

The different physical quantities enlisted in the Table 7.2 clearly indicate the stability of both the SiO and SiNHO cages in isolation. These quantities do not necessarily give a clear picture about the reactivity of the structures i.e. whether or not it form dimers with strong bonds when two such cages are brought in vicinity of each other. The ultimate criteria to check the stability of the structure is through the investigation of its reactivity. For example fullerene C_{60}

forms weak bonds between them when brought close together. We apply this test to both SiO and SiNHO cages.

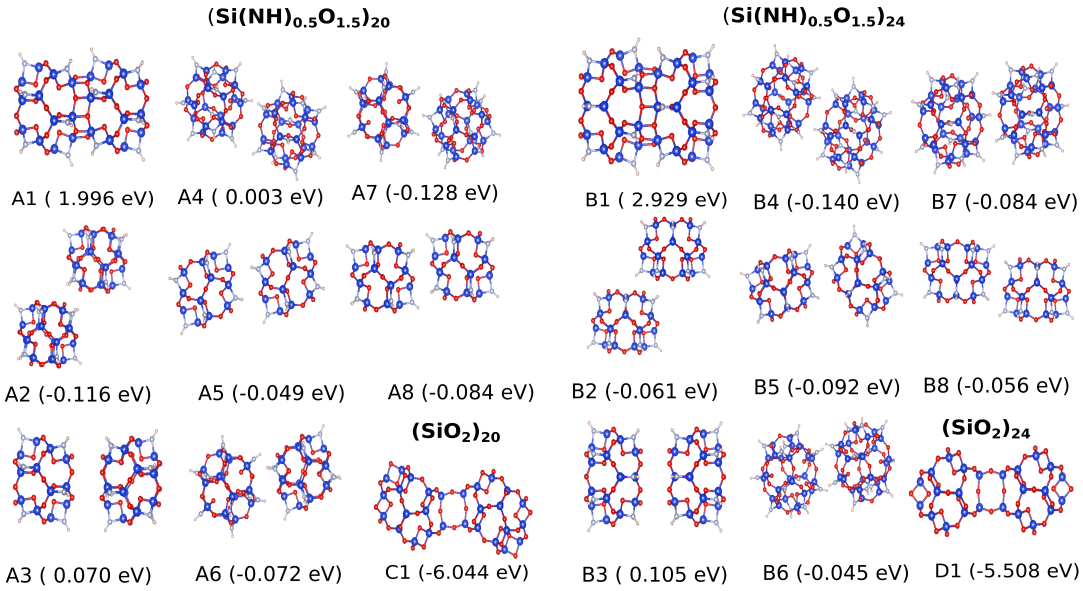

Figure 7.6: *The relaxed structure and dimerization energy for different possible arrangements of different cages are shown. First three columns (A1-A8) and last three columns (B1-B8) represent the dimers of* $\{Si(NH)_{0.5}O_{1.5}\}_{20}$ *and* $\{Si(NH)_{0.5}O_{1.5}\}_{24}$ *cages respectively. C1 and D1 represents the dimer of pure silica cages of size n = 20 and 24, respectively. The dimerization energy was evaluated using* BIGDFT *for the PBE using eq. (7.4)*

In this study we bring two such cages close together with different possible arrangements and relax them. The different possible ways in which the two cages can approach each other is shown in Fig 7.6. The dimerization energy is calculated using eq. (7.4). The silica cages SiO-20 and SiO-24 are highly reactive. They easily form dimers with large dimerization energies of 6.044 eV (SiO-20) and 5.508 eV (SiO-24) as shown in case C1 and D1 of Fig 7.6. However the relaxed structures of dimers of SiNHO-20 and SiNHO-24 cages always resulted in large distances between them and small D.E. This show that the cages form weak bonds between them. Since van der Waals correction was not used in the calculation, the only possibility of the origin of interaction is the long range electrostatic interaction. From the estimated multipole moments in Table 7.2 it is clear that it is due to the quadruple interaction as the dipole moment is negligible in both SiNHO-20 and SiNHO-24 cages. This study clearly distinguishes the stability of the structures which was not always conclusive from C.E. and HOMO-LUMO gap.

Distance vs Dimerization Energy Curves

Case A1 and B1 in Fig 7.6 are unique in comparison to other cases as they form covalent bonds between the cages, although energetically unfavorable. In experimental conditions, as the cages have rotational and translational degrees of freedom it may happen that they approach each other and form the configuration shown in case A1. In such a situation, the system has to gain energy in order to cross the barrier as it is an endothermic process.

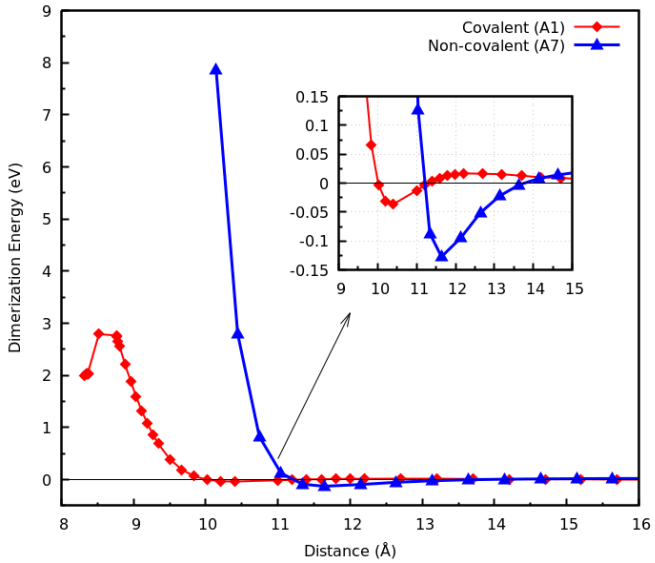

Figure 7.7: *Distance vs Dimerization energy curve for case A1 and A7 of* $\{Si(NH)_{0.5}O_{1.5}\}_{20}$ *as shown in Fig 7.6. Covalent(A1) and Non-covalent (A7) represents case A1 and A7 of dimers of* $\{Si(NH)_{0.5}O_{1.5}\}_{20}$. *These quantities were evaluated using* BIGDFT *for the PBE functional. The inset shows the minima when the cages are far apart.*

Therefore, to estimate the viability of this process we calculate the D.E. as function of distance between the cages and compare case A1 with case A7 of SiNHO-20. Here we also compute case A7 for reference to bring out the difference of distance vs D.E. profile. The distance vs D.E. plot for case A1 and A7 are shown in Fig 7.7. The nature of distance-D.E. plot of Non-covalent (A7) is very similar to long range weak bonding interaction. However, the distance-D.E. plot of Covalent (A1) is different from case A7: it has two minima. The higher minimum represents the structure of case A1. The energy difference between the two minima is ~2 eV, while the energy difference between the higher minimum and the maximum is about ~0.8 eV. In order to jump from lower minimum to higher minimum the system has to gain an energy of ~2.8 eV to cross the barrier. Hence, it is unlikely in experiments that the cages can really crossover this barrier and form covalent bonds unless energy is provided externally. The magnitude of D.E. of lower minimum is very small. The inset in Fig 7.7 gives a better resolution of lower minima. It is interesting to observe the dispersion like behavior for this cages.

7.3.4 Conclusions

In summary through MHM runs we found that the NH substituted silica cages SiNHO-20 and SiNHO-24 are putative lowest energy structure in their respective PES. The second lowest energy structures are 0.16 eV and 0.65 eV higher in energy for n=20 and n=24, respectively. Large HOMO-LUMO gaps and cohesive energy indicate that they are chemically stable in isolation. D.E. of the cages show that they are nonreactive and resistant to aggregation. The origin of weak bonding in the dimers is due to the quadrupole interaction as the dipole moment is negligible. Hence, the new proposed cage structures possess all the necessary properties to act as an building block for nanostructures i.e. (i) large energy gap between the structures, (ii) large HOMO-LUMO gap, (iii) large cohesive energies and (iv) resistant to aggregation. Hence, we hope that our proposed cage structure may generate interest in the experimental community and can be used to build assembled nanostructures.

7.4 Structure and Energetic properties of Small $(TiO_2)_n$ Nanoparticles, n=21-24

Recently nanostructured TiO_2 ("black TiO_2") has been discovered to absorb visible light, which makes it an efficient material for water splitting. Hydrogenization has been proposed to be at the origin of this beneficial electronic structure of black TiO_2. Here we investigate, using ab initio methods, alternative mechanisms related to structure modifications in nanoclusters that could be responsible for absorption in the visible range.

7.4.1 Introduction

Titanium dioxide (TiO_2) is mainly used as antireflection coating for solar cells and as photoelectrodes for photochemical energy conversion processes [126]. The reasons for the continuous interest in TiO_2 for energy conversion are that the titanium dioxide is chemically inert and has outstanding corrosion resistance to aqueous solutions[127, 128]. The photoelectrochemical (PEC) cell consisting of a crystalline TiO_2 anode and a Pt cathode can be used for water splitting under irradiation of light. Both optical and catalytical functionality are required for the PEC cells to obtain maximal absorption of solar energy. Nonetheless, an important drawback for its application as photoelectrode is related to the limited ability for light absorption due to a relatively large band gap value [126, 129]. TiO_2 absorbs only in the ultraviolet part of the solar emission spectra, thus imposing low conversion efficiency. A number of attempts have been made to narrow the band gap of TiO_2. Many attempts were focusing on doping of TiO_2 with cation or anion atoms[130–132]. TiO_2 nanostructures have attracted great attention since the prominent discovery made by B. O'Regan who demonstrated that the photovoltaic cell with sintered anatase TiO_2 nanoparticles exhibits a commercially realistic energy-conversion efficiency[127]. Since then, many studies have been performed on the synthesis, properties and modifications of TiO_2 nanomaterials which are referred to in recent review papers [133, 134].

TiO_2 nanocrystals (NCs) are mostly synthesized with sol-gel methods, resulting in a high degree of crystallinity [135, 136]. Although the crystal phases and the morphology are strongly affected by the synthesis conditions, both experiment and theory proved that smaller samples (with a diameter smaller than 11.2-17.6 nm for hydrothermal samples) show the anatase structure [137, 138]. State-of-the-art techniques have been employed to characterize the structure of TiO_2 nanoparticles, which indicate that the number of distorted octahedral and under-coordinated Ti atoms at the surface of nanoparticles is increased as the particles size decreases [139–142].

Hamad et al. performed a theoretical calculation on $(TiO_2)_n$ clusters ($n = 1-15$) with a combination of simulated annealing, Monte Carlo basin hopping, and genetic algorithm methods[143]. They claimed that particles with $n \geq 11$ have at least one central octahedron surrounded by a shell of surface tetrahedra, trigonal bipyramids, and square base pyramids.

Qu and Kroes [144] optimized $(TiO_2)_n$ for $n = 1-9$ using density-functional theory at the B3LYP/LANL2DZ level and argued that the lowest energy $(TiO_2)_n$ structures contain one or two terminal oxygen atoms. Mingyang Chen et al [145] employed a tree growth (TG) algorithm with a hybrid genetic algorithm (HGA). They found that optimized clusters (for $n = 2-13$) do not show the character of a TiO_2 bulk crystal with 6-fold coordinated Ti.

For larger clusters (1-2 nm) synthesized in experiment, the structure of these particles is especially sensitive to the synthesis methods and various treatments and reactions [137, 146–148], which can in turn tune their chemical reactivities and electronic and optical properties. Very little work on structure prediction of bare clusters in this size regime has been found in the literature. Studying the structure of these bare nanoclusters is fundamentally important not only to determine their phase stability, but also to gain a basic understanding of structure-property relationships in small clusters [149]. In our study we therefore investigate nanoparticles with a size similar to that in experiment. Our nanoclusters have diameters of about 1.2-1.5 nm.

Most theoretical studies have focused on passivated nanoclusters in this regime which assume the clusters having bulk-like structure [150]. However, passivation usually significantly changes the structure and properties of the nanocluster, which prevents us to understand the intrinsic properties of the bare clusters. Here we have performed minima hopping runs of the bare nanoclusters of TiO_2 at density functional level to theory to investigate its structural morphology and its relation to the energetic properties.

7.4.2 Computational Methods

The potential energy landscape of the $(TiO_2)_n$ clusters ($n = 21, 22, 23, 24$) was explored using the Minima Hopping Method [75–79] (MHM) for searching new configurations. The structural exploration was performed at DFT level using the electronic structure package BIGDFT [72], in which the MHM is implemented. The BIGDFT code uses Daubechies Wavelets as its basis set. The PBE functional was used to describe the exchange-correlation energy along with soft norm conserving HGH pseudopotentials including a non-linear core correction. The parameters for convergence were set in such a way that energy differences were converged to within 10^{-4} eV and the relaxation of the configuration was continued until the maximum force component of any atom was less then 5 meV/Å. The calculation was done with free boundary conditions. The HOMO-LUMO gap for these nanostructures were calculated using the PBE exchange correlation functional. The cohesive energy of the nanoclusters was evaluated using the eq. 7.5 where $E_{(TiO_2)_n}$ is total energy of the total structure and E_{TiO_2} is the total energy of single formula unit of TiO_2.

$$E_{coh} = \frac{E_{(TiO_2)_n}}{n} - E_{TiO_2} \tag{7.5}$$

7.4.3 Results

Lowest Energy Structure

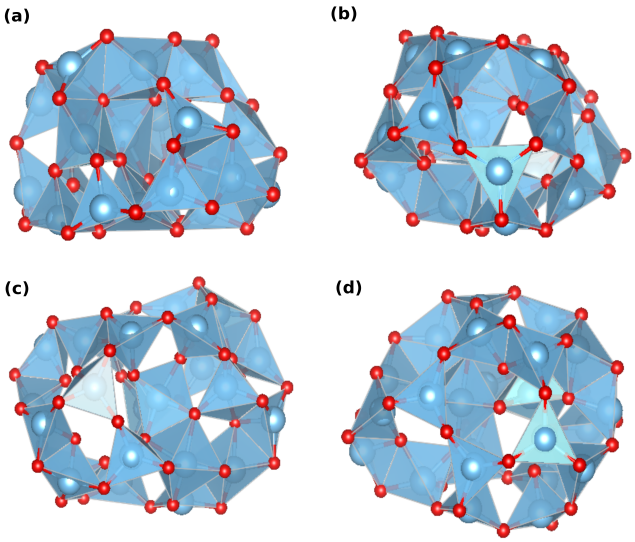

Figure 7.8: *The lowest energy structure for (a) n=21, (b) n=22, (c) n=23 and (d) n=24 formula units. Ti atoms are represented by large blue spheres, oxygen atoms are represented by small red spheres. In all the cases one Ti atom is found which is enclosed by an octahedra made by the oxygen atoms.*

The lowest energy structure obtained in the MHM run for each size of the TiO_2 nanocluster are shown in Fig 7.8. Unlike, bulk structures, where the Ti atom is coordinated to 6 oxygen atoms, most of the Ti atoms are coordinated to 4 oxygen atoms, where the Ti atoms are enclosed in a tetrahedron. A few of the Ti atoms have 5-fold coordination. Only one Ti atom in all the cases were able to have 6-fold coordination where the octahedra of the oxygen atoms are distorted. The structures of the TiO_2 nanoclusters found in this study do not have any well defined symmetry. As shown in Fig 7.8, the coordination polyhedra of the structures are distorted and randomly arranged.

Potential Energy Surface Profile

The energy spectrum of the structures of the $(TiO_2)_n$ nanoclusters obtained through MHM runs are shown in Fig 7.9. The lowest energy structures for all sizes are not well defined structures. There exists a lot of structures which are close in energy to the lowest energy structure. The energy differences between the lowest energy structure and the second-lowest is ranging from 86 meV to 294 meV for all sizes of nanoclusters. Among these structures, it have been found that structures with uncoordinated oxygen bonds have higher energy as compared to structures with coordinated oxygen bonds. This indicates that the satisfaction of the oxygen bonds stabilizes the TiO_2 clusters.

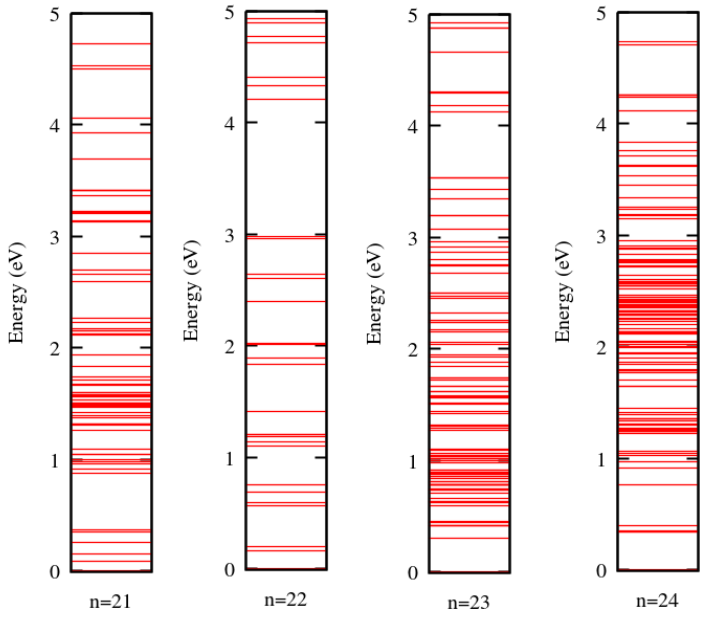

Figure 7.9: The energy spectrum plot for each size of the TiO_2 nanoclusters with n = 21, 22, 23 and 24.

Energetic Properties of the Nanoclusters

In order to study the stability and electronic properties of these nanoclusters, the HOMO-LUMO gap and the cohesive energy have been evaluated at the DFT level of theory with the PBE functional. The HOMO-LUMO gap and the cohesive energies of the 10 lowest energy structures of all sizes have been listed in Table 7.3.

Despite, being amorphous, these nanoclusters yield high values for the HOMO-LUMO gaps. Another, interesting point to observe is that the HOMO-LUMO gaps of different structures of the nanoclusters of size n=23 and n=24 vary over a wide range ~1.3-3 eV. Some of the high energy structures which have low gaps have uncoordinated oxygen atoms. They may give rise to mid-gap states which leads to fall in the HOMO-LUMO gap.

The cohesive energies of the $(TiO_2)_n$ nanoclusters were obtained using eq. 7.5 and are listed in Table 7.3. The difference in the cohesive energies of the structures of each size are very small. However, among the lowest energy structure of different sizes, $(TiO_2)_{23}$ does not follow the trend in the cohesive energy.

Cage Structure of $(TiO_2)_{24}$ nanocluster

For the nanoclusters of size n=24, a cage structure has been obtained which has completely coordinated O atoms. The cage structure is the third lowest energy structure. The side and top

Structure no	HOMO-LUMO Gap (eV)				$E_{cohesive}$ (eV)			
	n=21	n=22	n=23	n=24	n=21	n=22	n=23	n=24
1	2.86	3.02	2.74	3.08	-5.094	-5.148	-5.116	-5.193
2	2.74	3.21	1.97	3.10	-5.089	-5.141	-5.103	-5.179
3	2.76	2.96	2.92	2.82	-5.086	-5.139	-5.098	-5.178
4	2.96	2.96	2.71	2.88	-5.082	-5.123	-5.096	-5.178
5	2.83	2.94	1.89	2.85	-5.077	-5.121	-5.096	-5.176
6	2.83	2.28	1.85	2.93	-5.076	-5.117	-5.090	-5.161
7	2.69	2.90	2.91	2.06	-5.052	-5.114	-5.089	-5.155
8	2.66	2.93	1.83	2.82	-5.050	-5.098	-5.088	-5.153
9	2.67	2.87	1.85	1.30	-5.048	-5.097	-5.087	-5.150
10	2.87	2.81	2.82	2.28	-5.047	-5.094	-5.085	-5.149

Table 7.3: *The HOMO-LUMO gap and the cohesive energy of the ten lowest energy structures of nanoclusters of TiO_2 of all sizes (n=21, 22, 23 and 24). The calculations have been done using* BIGDFT *package for the PBE functional*

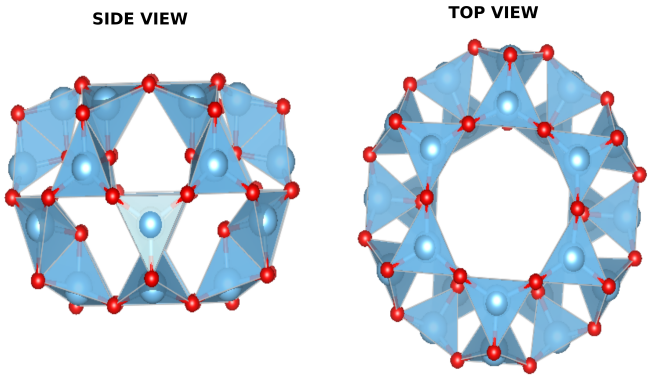

Figure 7.10: *The top and side view of the cage structure of $(TiO_2)_{24}$ which the is the third lowest energy structure.*

view of the cage is shown in Fig 7.10. The O atoms are 2-fold coordinated and the Ti atoms are 4 fold coordinated. This is unusual as compared to other structures where most of them are distorted and randomly organized.

7.4.4 Conclusion

The structure and energetic properties of the $(TiO_2)_n$ nanoparticles with $n = 21-24$ have been studied using structure-prediction methods. We found a large number of structures that are all based on a few structural motifs, namely distorted octahedra, pyramids and tetrahedra connected to each other through oxygen atoms at the corners of the polyhedra. The Ti atoms sit at the center of these polyhedra. Most of the Ti atoms are 4-fold coordinated. A few Ti atoms

have 5-fold coordination. Only, a single Ti atom has 6-fold coordination which is generally found in bulk structures.

The lowest energy structure of these nanoclusters are not well defined as a lot of the low energy structures are energetically close to the lowest energy structure. The energy differences range between 86 meV to 294 meV. Despite, being amorphous these clusters have large HOMO-LUMO gaps and cohesive energies. Among the structures of same size in particular n=23 and n=24, the HOMO-LUMO gap varies over a large range ~1.3-3 eV. The lowering of the gaps can be associated to the uncoordinated oxygen atoms in those structures. The single coordinated oxygen atoms (dangling bonds) give rise to mid level states.

Therefore, the optical absorption in the visible spectrum of light can be enhanced by introducing more dangling bonds in these nanoclusters. This can be affected by the synthesis of off-stoichiometric or doped TiO_2 clusters.

8 Outlook and Conclusion

8.1 Conclusion

The results presented in this thesis can be broadly classified as three contributions: (1) Obtaining all electron reference data for benchmarking (2) Generation and Benchmarking of soft dual space Gaussian type pseudopotentials and (3) Application of soft pseudopotentials for structure prediction of large clusters and cages.

Through the use of MWs as implemented in MRCHEM, the total energies and atomization energies of a large data set of molecules for the PBE and the PBE0 exchange correlation functionals were calculated for the first time till date, with guaranteed μHa accuracy. These highly accurate reference data also allowed the estimation of errors introduced by the GTOs and the NAOs basis sets used in different quantum chemistry codes. Among the GTOs, only the largest basis set (aug-cc-pV5Z) employed for the benchmark study was able to achieve chemical accuracy. However, both the largest (tier4) and the medium size basis sets of the NAOs (tight, tier2) were able to achieve chemical accuracy. This demonstrates that NAOs are better for regular production DFT calculations as compared to the GTOs. However, both the GTOs and NAOs have large errors in the electrostatic dipole moment of the molecules.

The application of the softness constraint on the pseudo orbitals of the pseudo atom, through the softness penalty term made it possible to generate soft dual space Gaussian type pseudopotentials for the PBE and the PBE0 exchange correlation functionals. As the pseudopotentials are fitted to multiple atomic configuration, the property of transferability was taken into account during the fitting cycles. For the benchmark studies of these pseudopotentials, the data set of molecules and the reference data obtained using MWs as explained above were used. The benchmark studies of the PBE and the PBE0 pseudopotentials display remarkable accuracy and transferability with a mean absolute deviation of ~ 1.38 kcal/mol in atomization energy of molecules which is optimal for regular production runs. The mean absolute error in the electrostatic dipole moment of the molecules are comparable to the errors obtained using the medium sized basis sets in GTOs. Through these tests and benchmarks, the pseudopotentials display their softness, accuracy and transferability.

These new soft pseudopotentials were used for the structure prediction of large systems: (1) Metastable exohedrally decorated borospherene(B_{40}) and (2) Prediction of $\{Si(NH)_{0.5}O_{1.5}\}_n$ cages. Through our investigations, exohedrally decorated borospherene (B_{40}) cages that were believed to be ground state structures in the literature, turned out to be only metastable structures. On other hand new $\{Si(NH)_{0.5}O_{1.5}\}_n$ (n=20, 24) cages were predicted which are found to be stable and nonreactive. They possess all the necessary features to behave like fullerene. Hence, they could be used as building blocks for new materials.

The pseudopotentials were also used for the investigation of $(TiO_2)_n$ nanoclusters to understand the origin of the unusual absorption of the "black TiO_2" in the visible spectrum. Through the Minima Hopping runs of the $(TiO_2)_n$ nanoclusters, a large number of structures are found. The structures were found to be devoid of symmetry, where the Ti atoms are coordinated to the O atoms in tetrahedra, octahedra or pyramidal arrangements. These coordination polyhedra are attached to each other through the O atoms. Among the nanoclusters, the structures with singly terminated O atoms often have small HOMO-LUMO gaps and are higher in energy as compared to the lowest energy structure. These singly terminated O atoms in the nanoclusters possibly gave rise to the mid-level states which leads to decrease in HOMO-LUMO gaps and therefore, absorption in the visible spectrum.

8.2 Future Developments

New soft, accurate and transferable dual space Gaussian type pseudopotential have been generated for the PBE and the PBE0 functionals which are discussed in this thesis. However, there exists a lot of room for improvements. The new possibilities are listed below:

1. A new routine can be written for the calculation of the meta-GGA functionals.
2. The pseudopotential fitting program can be used for the generation of pseudopotentials for heavy elements.
3. It would be useful to generate pseudopotentials for some other commonly used hybrid functionals such as B3LYP, HSE06 etc.
4. The atoms in a unit cell come closer under high pressure as compared to normal conditions. It may be possible that the current pseudopotentials may not adapt the changes in chemical environment due to high pressure as they are not accounted during pseudopotential constructions. These feature can be easily included in the pseudopotential construction through the confining potential. It would be useful if these high pressure cases are considered in the pseudopotential benchmarking.
5. At present, the database of molecules presented in this thesis only consider elements till third row of the periodic table. A database of molecules consisting of heavy elements will be necessary for benchmarking the pseudopotentials of heavy elements. In general

these pseudopotentials are benchmarked against bulk systems of different chemical compositions such as oxides or nitrides to inspect their accuracy and transferability.

Though some tips have been provided to make the generation of pseudopotentials user friendly, it still remains a difficult task which improves only through experience. Generation of good input guess is one of the most difficult job in this fitting process. A good input guess is vital for generating a pseudopotential with desirable features. It often involves tricks and trying out different possibilities.

Appendices

A Pseudopotential parameters of different elements

$$\hat{V}_{PSP} = \hat{V}_{loc} + \hat{V}_{nl} \tag{A.1}$$

The first part i.e. local part takes the form

$$V_{loc}(r) = -\frac{Z_{ion}}{r} erf\left(\frac{r}{\sqrt{2}r_{loc}}\right) + exp\left(-\frac{r^2}{2r_{loc}^2}\right)\sum_{k=1}^{k\leq 4} C_k\left(\frac{r}{r_{loc}}\right)^{2k-2} \tag{A.2}$$

The second part i.e. the non-local term is split into different channels where $\hat{V}_{nl} = \sum_l V_l(r,r')$. The term $V_l(r,r')$ is expressed in terms of separable projectors (A.3) which are defined as eq. (A.4).

$$V_l(\mathbf{r},\mathbf{r}') = \sum_{i,j=1}^{n\leq 3}\sum_{m=-l}^{l} p_i^{l,m}(r) h_{i,j}^l p_j^{l,m}(r') \tag{A.3}$$

$$p_i^{l,m}(r) = \frac{\sqrt{2}r^{l+2(i-1)} e^{\left(-\frac{r^2}{2r_l^2}\right)}}{r_l^{l+(4i-1)/2}\sqrt{\Gamma(l+\frac{4i-1}{2})}} Y_{l,m}(\theta,\varphi) \tag{A.4}$$

The model core charge for the NLCC is given by

$$\rho_c(r) = c_{core}\frac{Z_{nuc}-Z_{ion}}{(\sqrt{2\pi}r_{core})^3} e^{-\left(\frac{r^2}{2r_{core}^2}\right)} \tag{A.5}$$

During the evaluation of the Kohn Sham energy with the HGH-NLCC pseudopotential, the model charge density is used only in the exchange correlation part. The total KS energy

expression with NLCC can be written as

$$E_{KS} = \sum_i \langle \psi_i | -\frac{1}{2}\nabla^2 + V_H[\rho] + V_{xc}[\rho+\rho_c] + V_{PSP} | \psi_i \rangle - E_H[\rho] + E_{xc}[\rho+\rho_c] - \int \rho(r) V_{xc}[\rho+\rho_c](r) dr \tag{A.6}$$

Here E_{xc} represents the exchange correlation energy, V_{xc} represents exchange correlation potential, V_H represents Hartree potential and ψ_i are the KS orbitals.

A.1 HGH-NLCC Pseudopotential Parameters of Light Elements (H-C) for PBE Functionals

H	1	1				Z_{nuc}	Z_{ion}			
	0.22873	-3.72290	0.65760			r_{loc}	c_1	c_2		
He	2	2				Z_{nuc}	Z_{ion}			
	0.22000	-8.43080	1.59912			r_{loc}	c_1	c_2		
Li	3	1				Z_{nuc}	Z_{ion}			
	0.81163	-1.07249	0.20165			r_{loc}	c_1	c_2		
	0.69760	1.55506				r_s	h^s_{11}			
	0.76801	0.28730				r_{core}	c_{core}			
Li	3	3				Z_{nuc}	Z_{ion}			
	0.48000	-12.63333	9.44319	-1.88725	0.09645	r_{loc}	c_1	c_2	c_3	c_4
Be	4	2				Z_{nuc}	Z_{ion}			
	0.72000	-1.84638	0.26055			r_{loc}	c_1	c_2		
	0.49588	3.34579				r_s	h^s_{11}			
	0.32394	0.41160				r_{core}	c_{core}			
Be	4	4				Z_{nuc}	Z_{ion}			
	0.35000	-8.30344	1.45310			r_{loc}	c_1	c_2		
	0.27000	-11.37616	6.43170			r_s	h^s_{11}	h^s_{12}		
			-4.02556					h^s_{22}		
B	5	3				Z_{nuc}	Z_{ion}			
	0.49593	-3.21500	0.49383			r_{loc}	c_1	c_2		
	0.51530	6.77688	-1.95302			r_s	h^s_{11}	h^s_{12}		
			0.57309					h^s_{22}		
	0.44059	0.78133				r_{core}	c_{core}			
C	6	4				Z_{nuc}	Z_{ion}			
	0.41329	-5.72930	0.87475			r_{loc}	c_1	c_2		
	0.43410	9.01955	-2.41858			r_s	h^s_{11}	h^s_{12}		
			0.55473					h^s_{22}		
	0.36240	0.60557				r_{core}	c_{core}			

A.2 HGH-NLCC Pseudopotential Parameters of Light Elements (N-Si) for PBE Functionals

N	7	5		Z_{nuc}	Z_{ion}	
	0.40469	-8.10098	1.29419	r_{loc}	c_1	c_2
	0.42560	9.21833	-2.49059	r_s	h^s_{11}	h^s_{12}
			0.38356			h^s_{22}
	0.35406	0.38000		r_{core}	c_{core}	
O	8	6		Z_{nuc}	Z_{ion}	
	0.34550	-11.74359	1.90654	r_{loc}	c_1	c_2
	0.36804	10.85891	-2.12901	r_s	h^s_{11}	h^s_{12}
			-0.42977			h^s_{22}
	0.34517	0.23248		r_{core}	c_{core}	
F	9	7		Z_{nuc}	Z_{ion}	
	0.30271	-15.36075	2.45384	r_{loc}	c_1	c_2
	0.31898	14.70725	-2.98548	r_s	h^s_{11}	h^s_{12}
			-0.41217			h^s_{22}
	0.26297	0.25250		r_{core}	c_{core}	
Ne	10	8		Z_{nuc}	Z_{ion}	
	0.30809	-17.94117	3.02848	r_{loc}	c_1	c_2
	0.31860	15.08710	-3.15454	r_s	h^s_{11}	h^s_{12}
			-0.63777			h^s_{22}
	0.29304	0.36593		r_{core}	c_{core}	
Mg	12	2		Z_{nuc}	Z_{ion}	
	0.65406	-5.22393	0.91370	r_{loc}	c_1	c_2
	0.48001	6.34259	-2.08214	r_s	h^s_{11}	h^s_{12}
			3.44562			h^s_{22}
	0.57942	1.96776		r_p	h^p_{11}	
	0.45589	0.34873		r_{core}	c_{core}	
Al	13	3		Z_{nuc}	Z_{ion}	
	0.60224	-5.18802	0.69616	r_{loc}	c_1	c_2
	0.45122	6.17503	-1.91494	r_s	h^s_{11}	h^s_{12}
			3.68229			h^s_{22}
	0.53747	2.27296		r_p	h^p_{11}	
	0.43029	0.35833		r_{core}	c_{core}	
Si	14	4		Z_{nuc}	Z_{ion}	
	0.55318	-3.88383	0.39048	r_{loc}	c_1	c_2
	0.41164	5.41134	-1.60000	r_s	h^s_{11}	h^s_{12}
			4.01974			h^s_{22}
	0.49248	2.43794		r_p	h^p_{11}	
	0.39203	0.35951		r_{core}	c_{core}	

A.3 HGH-NLCC Pseudopotential Parameters of Light Elements (P-Ar) for PBE Functionals

P	15	5		Z_{nuc}	Z_{ion}	
	0.47303	-5.64603	0.64426	r_{loc}	c_1	c_2
	0.37336	4.62035	-0.63842	r_s	h^s_{11}	h^s_{12}
			4.21895			h^s_{22}
	0.42787	3.53692		r_p	h^p_{11}	
	0.35069	0.50000		r_{core}	c_{core}	
Cl	17	7		Z_{nuc}	Z_{ion}	
	0.43228	0.24738	-0.77814	r_{loc}	c_1	c_2
	0.33909	6.93128	-1.63356	r_s	h^s_{11}	h^s_{12}
			4.67949			h^s_{22}
	0.39006	3.33584		r_p	h^p_{11}	
	0.31790	0.74093		r_{core}	c_{core}	
Ar	18	8		Z_{nuc}	Z_{ion}	
	0.44846	0.16764	-1.60217	r_{loc}	c_1	c_2
	0.35178	11.79047	-4.14831	r_s	h^s_{11}	h^s_{12}
			5.02661			h^s_{22}
	0.40466	2.78132		r_p	h^p_{11}	
	0.33980	0.90016		r_{core}	c_{core}	

A.4 HGH-NLCC Pseudopotential Parameters of Heavy Elements K-Ti for PBE Functionals

K	19	9		Z_{nuc}	Z_{ion}	
	0.61120	18.55895	-2.98437	r_{loc}	c_1	c_2
	0.41430	-1.54324	0.25201	r_s	h^s_{11}	h^s_{12}
			-4.11457			h^s_{22}
	0.35655	-5.66832	2.51741	r_p	h^p_{11}	h^p_{12}
			-6.61321			h^p_{22}
	0.34499	-11.65920		r_d	h^d_{11}	
	0.36896	0.49919		r_{core}	c_{core}	
Ca	20	10		Z_{nuc}	Z_{ion}	
	0.59199	17.61894	-2.43213	r_{loc}	c_1	c_2
	0.41299	-3.10608	-0.25644	r_s	h^s_{11}	h^s_{12}
			-2.65139			h^s_{22}
	0.36049	-3.77293	0.68959	r_p	h^p_{11}	h^p_{12}
			-4.82046			h^p_{22}
	0.34999	-10.96478		r_d	h^d_{11}	
	0.37178	0.46804		r_{core}	c_{core}	
Sc	21	11		Z_{nuc}	Z_{ion}	
	0.54694	9.00601	-0.65954	r_{loc}	c_1	c_2
	0.42877	-1.64516	1.04646	r_s	h^s_{11}	h^s_{12}
			-2.73036			h^s_{22}
	0.41183	-5.68053	1.29590	r_p	h^p_{11}	h^p_{12}
			-1.12573			h^p_{22}
		-0.15760	0.30847		k^p_{11}	k^p_{12}
			-0.38268			k^p_{22}
	0.35275	-7.15731		r_d	h^d_{11}	
		0.00208			k^d_{11}	
	0.38795	0.45517		r_{core}	c_{core}	
Ti	22	12		Z_{nuc}	Z_{ion}	
	0.51194	9.54470	-0.89545	r_{loc}	c_1	c_2
	0.39377	-1.20250	1.43470	r_s	h^s_{11}	h^s_{12}
			-3.47669			h^s_{22}
	0.37683	-5.93044	1.44770	r_p	h^p_{11}	h^p_{12}
			-1.42790			h^p_{22}
		0.90975	-0.36889		k^p_{11}	k^p_{12}
			0.02081			k^p_{22}
	0.31775	-8.59111		r_d	h^d_{11}	
		0.00296			k^d_{11}	
	0.35495	0.49967		r_{core}	c_{core}	

A.5 HGH-NLCC Pseudopotential Parameters of Heavy Elements V, Sr, Y for PBE Functionals

V	23	13		Z_{nuc}	Z_{ion}	
	0.47939	8.40989	0.78733	r_{loc}	c_1	c_2
	0.41119	-0.89039	0.04929	r_s	h^s_{11}	h^s_{12}
			-1.89789			h^s_{22}
	0.35160	-5.98940	1.30217	r_p	h^p_{11}	h^p_{12}
			-2.11022			h^p_{22}
		-0.36255	1.06555		k^p_{11}	k^p_{12}
			-1.48569			k^p_{22}
	0.33494	-8.02664		r_d	h^d_{11}	
		0.00309			k^d_{11}	
	0.39519	0.49896		r_{core}	c_{core}	
Sr	38	10		Z_{nuc}	Z_{ion}	
	0.65120	17.98404	-2.60864	r_{loc}	c_1	c_2
	0.45429	-3.53474	2.71196	r_s	h^s_{11}	h^s_{12}
			-5.45579			h^s_{22}
	0.39655	10.10752	-3.42692	r_p	h^p_{11}	h^p_{12}
			-3.88765			h^p_{22}
		0.13020	0.08289		k^p_{11}	k^p_{12}
			-0.05897			k^p_{22}
	0.38500	-7.35239		r_d	h^d_{11}	
		0.01613			k^d_{11}	
	0.40896	0.66222		r_{core}	c_{core}	
Y	39	11		Z_{nuc}	Z_{ion}	
	0.67848	13.32286	-1.84557	r_{loc}	c_1	c_2
	0.53405	-4.05698	0.87353	r_s	h^s_{11}	h^s_{12}
			-1.73120			h^s_{22}
	0.51335	-5.09537	0.90680	r_p	h^p_{11}	h^p_{12}
			-0.67110			h^p_{22}
		-0.04308	0.13245		k^p_{11}	k^p_{12}
			-0.13225			k^p_{22}
	0.38500	-4.69926		r_d	h^d_{11}	
		0.01203			k^d_{11}	
	0.48416	0.34974		r_{core}	c_{core}	

A.6 HGH-NLCC Pseudopotential Parameters of Heavy Elements Zr-Mo for PBE Functionals

Zr	40	12		Z_{nuc}	Z_{ion}	
	0.58023	18.04122	-2.80560	r_{loc}	c_1	c_2
	0.42726	-3.83194	3.18642	r_s	h^s_{11}	h^s_{12}
			-5.00121			h^s_{22}
	0.35456	10.81139	-3.62978	r_p	h^p_{11}	h^p_{12}
			-3.41893			h^p_{22}
		0.09888	-0.12022		k^p_{11}	k^p_{12}
			0.25312			k^p_{22}
	0.33987	-7.36447		r_d	h^d_{11}	
		0.02708			k^d_{11}	
	0.36972	0.50789		r_{core}	c_{core}	
Nb	41	13		Z_{nuc}	Z_{ion}	
	0.61579	13.83804	-2.00166	r_{loc}	c_1	c_2
	0.50278	-2.90006	0.43265	r_s	h^s_{11}	h^s_{12}
			-1.48583			h^s_{22}
	0.46665	-5.18626	1.31913	r_p	h^p_{11}	h^p_{12}
			-1.00378			h^p_{22}
		0.07293	0.27674		k^p_{11}	k^p_{12}
			-0.41584			k^p_{22}
	0.39959	-5.10034		r_d	h^d_{11}	
		0.01659			k^d_{11}	
	0.42811	0.30733		r_{core}	c_{core}	
Mo	42	14		Z_{nuc}	Z_{ion}	
	0.56056	16.54768	-2.28823	r_{loc}	c_1	c_2
	0.45218	-2.20958	0.58224	r_s	h^s_{11}	h^s_{12}
			-2.20099			h^s_{22}
	0.41752	-4.83558	1.08499	r_p	h^p_{11}	h^p_{12}
			-1.44535			h^p_{22}
		-0.60917	1.16478		k^p_{11}	k^p_{12}
			-1.34066			k^p_{22}
	0.37321	-5.38426		r_d	h^d_{11}	
		0.02136			k^d_{11}	
	0.41057	0.28468		r_{core}	c_{core}	

A.7 HGH-NLCC Pseudopotential Parameters of Heavy Elements Tc-Rh for PBE Functionals

Tc	43	15		Z_{nuc}	Z_{ion}	
	0.54180	16.94339	-2.21488	r_{loc}	c_1	c_2
	0.43648	-1.44992	-0.18042	r_s	h^s_{11}	h^s_{12}
			-1.78365			h^s_{22}
	0.40766	-5.95933	1.62632	r_p	h^p_{11}	h^p_{12}
			-1.85359			h^p_{22}
		-1.53284	1.88408		k^p_{11}	k^p_{12}
			-1.90347			k^p_{22}
	0.36946	-5.59808		r_d	h^d_{11}	
		0.02246			k^d_{11}	
	0.36204	0.09960		r_{core}	c_{core}	
Ru	44	16		Z_{nuc}	Z_{ion}	
	0.52348	17.09781	-2.31321	r_{loc}	c_1	c_2
	0.42008	-1.06708	0.07405	r_s	h^s_{11}	h^s_{12}
			-2.25880			h^s_{22}
	0.39179	-6.03062	1.88580	r_p	h^p_{11}	h^p_{12}
			-2.21233			h^p_{22}
		-1.40733	1.96564		k^p_{11}	k^p_{12}
			-0.20921			k^p_{22}
	0.36946	-5.83110		r_d	h^d_{11}	
		0.02565			k^d_{11}	
	0.34699	0.12923		r_{core}	c_{core}	
Rh	45	17		Z_{nuc}	Z_{ion}	
	0.50658	17.64742	-2.34984	r_{loc}	c_1	c_2
	0.40602	-0.78019	0.06845	r_s	h^s_{11}	h^s_{12}
			-2.50633			h^s_{22}
	0.37966	-5.86004	1.71644	r_p	h^p_{11}	h^p_{12}
			-2.18831			h^p_{22}
		-1.10086	1.69500		k^p_{11}	k^p_{12}
			-1.84584			k^p_{22}
	0.34518	-6.08372		r_d	h^d_{11}	
		0.02820			k^d_{11}	
	0.33416	0.12950		r_{core}	c_{core}	

A.8 HGH-NLCC Pseudopotential Parameters of Heavy Elements Pd-Cd for PBE Functionals

Pd	46	18		Z_{nuc}	Z_{ion}	
	0.48640	18.52091	-2.49094	r_{loc}	c_1	c_2
	0.38872	-0.43163	0.42116	r_s	h^s_{11}	h^s_{12}
			-3.09919			h^s_{22}
	0.36401	-5.74044	1.90163	r_p	h^p_{11}	h^p_{12}
			-2.57490			h^p_{22}
		-1.37195	1.85671		k^p_{11}	k^p_{12}
			-1.90491			k^p_{22}
	0.33148	-6.32798		r_d	h^d_{11}	
		0.03235			k^d_{11}	
	0.32176	0.20840		r_{core}	c_{core}	
Ag	47	19		Z_{nuc}	Z_{ion}	
	0.47869	18.65989	-1.65269	r_{loc}	c_1	c_2
	0.37907	1.04196	-1.17905	r_s	h^s_{11}	h^s_{12}
			-2.20467			h^s_{22}
	0.35938	-5.68214	1.52729	r_p	h^p_{11}	h^p_{12}
			-2.64910			h^p_{22}
		-4.79931	4.64737		k^p_{11}	k^p_{12}
			-4.19248			k^p_{22}
	0.35017	-6.09555		r_d	h^d_{11}	
		0.02866			k^d_{11}	
	0.33804	0.49212		r_{core}	c_{core}	
Cd	48	20		Z_{nuc}	Z_{ion}	
	0.48127	16.87741	-1.12195	r_{loc}	c_1	c_2
	0.38399	0.05169	-1.39258	r_s	h^s_{11}	h^s_{12}
			-1.61648			h^s_{22}
	0.36364	-5.70884	0.49683	r_p	h^p_{11}	h^p_{12}
			-1.21685			h^p_{22}
		-3.53209	4.06373		k^p_{11}	k^p_{12}
			-0.41467			k^p_{22}
	0.35346	-6.43121		r_d	h^d_{11}	
		0.02900			k^d_{11}	
	0.34275	0.48942		r_{core}	c_{core}	

A.9 HGH-NLCC Pseudopotential Parameters of Light Elements (H-C) for PBE0 Functionals

H	1	1				Z_{nuc}	Z_{ion}			
	0.22873	-3.72290	0.65760			r_{loc}	c_1	c_2		
He	2	2				Z_{nuc}	Z_{ion}			
	0.22000	-8.42982	1.59734			r_{loc}	c_1	c_2		
Li	3	1				Z_{nuc}	Z_{ion}			
	0.81163	-1.04032	0.18351			r_{loc}	c_1	c_2		
	0.69743	1.56798				r_s	h^s_{11}			
	0.76750	0.29585				r_{core}	c_{core}			
Li	3	3				Z_{nuc}	Z_{ion}			
	0.47992	-12.608673	9.38546	-1.86997	0.09546	r_{loc}	c_1	c_2	c_3	c_4
Be	4	2				Z_{nuc}	Z_{ion}			
	0.72000	-1.84778	0.25751			r_{loc}	c_1	c_2		
	0.49588	3.35068				r_s	h^s_{11}			
	0.32394	0.41158				r_{core}	c_{core}			
Be	4	4				Z_{nuc}	Z_{ion}			
	0.35000	-5.97540	0.85668			r_{loc}	c_1	c_2		
	0.27000	-13.44677	0.71930			r_s	h^s_{11}	h^s_{12}		
			-4.49703					h^s_{22}		
B	5	3				Z_{nuc}	Z_{ion}			
	0.49593	-3.41358	0.51312			r_{loc}	c_1	c_2		
	0.51530	7.56628	-2.45956			r_s	h^s_{11}	h^s_{12}		
			0.89639					h^s_{22}		
	0.44059	0.77990				r_{core}	c_{core}			
C	6	4				Z_{nuc}	Z_{ion}			
	0.41329	-5.8024	0.88423			r_{loc}	c_1	c_2		
	0.43410	11.05567	-3.74483			r_s	h^s_{11}	h^s_{12}		
			1.41908					h^s_{22}		
	0.36240	0.75399				r_{core}	c_{core}			

A.10 HGH-NLCC Pseudopotential Parameters of Light Elements (N-Si) for PBE0 Functionals

N	7	5		Z_{nuc}	Z_{ion}	
	0.40469	-8.20785	1.30570	r_{loc}	c_1	c_2
	0.42560	9.25678	-2.52783	r_s	h^s_{11}	h^s_{12}
			0.42119			h^s_{22}
	0.35406	0.37877		r_{core}	c_{core}	
O	8	6		Z_{nuc}	Z_{ion}	
	0.34550	-11.74292	1.87490	r_{loc}	c_1	c_2
	0.36804	12.19702	-3.16044	r_s	h^s_{11}	h^s_{12}
			0.37138			h^s_{22}
	0.34517	0.22320		r_{core}	c_{core}	
F	9	7		Z_{nuc}	Z_{ion}	
	0.30169	-15.53059	2.47602	r_{loc}	c_1	c_2
	0.31658	17.63794	-5.01149	r_s	h^s_{11}	h^s_{12}
			1.06185			h^s_{22}
	0.26294	0.25495		r_{core}	c_{core}	
Ne	10	8		Z_{nuc}	Z_{ion}	
	0.30809	-18.00532	3.01504	r_{loc}	c_1	c_2
	0.31859	23.06976	-9.39472	r_s	h^s_{11}	h^s_{12}
			-4.25561			h^s_{22}
	0.29304	0.37225		r_{core}	c_{core}	
Mg	12	2		Z_{nuc}	Z_{ion}	
	0.65406	-7.18475	1.03384	r_{loc}	c_1	c_2
	0.46984	9.13632	-4.22648	r_s	h^s_{11}	h^s_{12}
			5.81114			h^s_{22}
	0.60161	2.03682		r_p	h^p_{11}	
	0.45716	0.34880		r_{core}	c_{core}	
Al	13	3		Z_{nuc}	Z_{ion}	
	0.60224	-6.62575	0.81667	r_{loc}	c_1	c_2
	0.45122	17.61711	-7.16791	r_s	h^s_{11}	h^s_{12}
			6.36679			h^s_{22}
	0.53747	2.51061		r_p	h^p_{11}	
	0.43029	0.27837		r_{core}	c_{core}	
Si	14	4		Z_{nuc}	Z_{ion}	
	0.55318	-4.50861	0.44271	r_{loc}	c_1	c_2
	0.41164	7.79949	-2.61791	r_s	h^s_{11}	h^s_{12}
			4.54976			h^s_{22}
	0.49248	2.54097		r_p	h^p_{11}	
	0.39203	0.34755		r_{core}	c_{core}	

A.11 HGH-NLCC Pseudopotential Parameters of Light Elements (P-Ar) for PBE0 Functionals

P	15	5		Z_{nuc}	Z_{ion}	
	0.47303	-6.48603	0.62895	r_{loc}	c_1	c_2
	0.37405	16.21072	-6.35446	r_s	h^s_{11}	h^s_{12}
			7.18164			h^s_{22}
	0.43153	3.60745		r_p	h^p_{11}	
	0.34711	0.50000		r_{core}	c_{core}	
Cl	17	7		Z_{nuc}	Z_{ion}	
	0.33906	-1.85175	-0.95789	r_{loc}	c_1	c_2
	0.32631	12.32130	-3.74597	r_s	h^s_{11}	h^s_{12}
			6.91691			h^s_{22}
	0.36612	4.96384		r_p	h^p_{11}	
	0.35006	0.76321		r_{core}	c_{core}	
Ar	18	8		Z_{nuc}	Z_{ion}	
	0.44846	1.94757	-1.51143	r_{loc}	c_1	c_2
	0.35178	12.78083	-4.75350	r_s	h^s_{11}	h^s_{12}
			5.13584			h^s_{22}
	0.40466	2.54157		r_p	h^p_{11}	
	0.33980	0.90031		r_{core}	c_{core}	

B Structure of theoretically discovered $\{Si(NH)_{0.5}O_{1.5}\}_n$ Cages

The atomic coordinate of the theoretically discovered $\{Si(NH)_{0.5}O_{1.5}\}_n$ cages are given here in Å.

B.1 Atomic Coordinates of $\{Si(NH)_{0.5}O_{1.5}\}_{20}$

Atom	x	y	z
Si	1.712177	1.960749	2.811679
Si	-1.211984	2.230438	2.865836
Si	-2.374463	-0.466790	2.964968
Si	-0.168646	-2.406839	2.972358
Si	2.354748	-0.905778	2.879212
O	0.287061	2.359375	3.532043
O	-1.994024	0.994221	3.619639
O	-1.418147	-1.600920	3.676501
O	1.229791	-1.842497	3.631077
O	2.280523	0.599229	3.540719
Si	2.533745	2.889680	0.729153
Si	-1.929559	3.299223	0.813264
Si	-3.699686	-0.814714	0.966336
Si	-0.330876	-3.770952	0.976622
Si	3.518797	-1.480124	0.833179
O	1.733502	4.033100	-0.149667
O	-0.968827	4.281131	-0.098931
O	-3.298944	2.892531	-0.010804
O	-4.371377	0.400853	0.077031
O	-3.772179	-2.244883	0.148177
O	-1.733503	-4.033101	0.149668

Appendix B. Structure of theoretically discovered $\{\mathbf{Si(NH)_{0.5}O_{1.5}}\}_n$ Cages

Atom	x	y	z
O	0.968824	-4.281131	0.098928
O	3.298943	-2.892532	0.010806
O	4.371375	-0.400855	-0.077034
O	3.772178	2.244883	-0.148177
Si	0.330875	3.770953	-0.976623
Si	-3.518796	1.480124	-0.833179
Si	-2.533745	-2.889679	-0.729152
Si	1.929558	-3.299222	-0.813263
Si	3.699685	0.814714	-0.966336
Si	0.168647	2.406841	-2.972359
Si	-2.354747	0.905780	-2.879213
Si	-1.712176	-1.960748	-2.811677
Si	1.211985	-2.230437	-2.865836
Si	2.374463	0.466791	-2.964970
O	1.418145	1.600917	-3.676503
O	-1.229791	1.842499	-3.631079
O	-2.280523	-0.599229	-3.540719
O	-0.287061	-2.359375	-3.532042
O	1.994025	-0.994220	-3.619641
O	1.498889	1.711172	1.202429
O	-1.108539	1.950490	1.250545
O	-2.145453	-0.454029	1.338447
O	-0.175114	-2.181926	1.345107
O	2.072239	-0.841804	1.262422
N	2.830901	3.229744	2.411313
N	-2.093830	3.683747	2.503775
N	-4.045172	-0.847243	2.672930
N	-0.331349	-4.112985	2.684105
N	3.913028	-1.589869	2.525796
O	0.175112	2.181926	-1.345108
O	-2.072239	0.841802	-1.262422
O	-1.498889	-1.711172	-1.202428
O	1.108540	-1.950488	-1.250545
O	2.145452	0.454031	-1.338448
N	0.331351	4.112983	-2.684103
N	-3.913027	1.589870	-2.525795
N	-2.830899	-3.229742	-2.411312
N	2.093831	-3.683746	-2.503775
N	4.045173	0.847243	-2.672930
H	3.400602	3.883820	2.929227
H	-4.860067	-1.018297	3.245024

Atom	x	y	z
H	-0.406299	-4.941014	3.257992
H	-2.513731	4.429542	3.040538
H	4.702414	-1.912953	3.067045
H	-3.400606	-3.883816	-2.929227
H	4.860071	1.018282	-3.245023
H	2.513729	-4.429541	-3.040538
H	-4.702415	1.912954	-3.067042
H	0.406304	4.941016	-3.257992

B.2 Atomic Coordinates of $\{\mathbf{Si(NH)_{0.5}O_{1.5}}\}_{24}$

Atom	x	y	z
Si	-2.846656	1.541704	2.554402
Si	-2.844003	-1.437843	2.621024
Si	-2.844540	-2.981973	0.069257
Si	-2.849693	-1.548846	-2.545834
Si	-2.852380	1.431085	-2.612742
Si	-2.850059	2.975280	-0.060645
O	-3.532962	0.053014	2.665860
O	-3.529994	-2.273175	1.383645
O	-3.533207	-2.328830	-1.271691
O	-3.538431	-0.061162	-2.654195
O	-3.536562	2.265285	-1.373624
O	-3.534457	2.319740	1.281436
Si	-0.882977	2.289280	3.777534
Si	-0.878883	-2.126517	3.876851
Si	-0.881294	-4.416533	0.096054
Si	-0.888200	-2.291590	-3.775462
Si	-0.892374	2.123733	-3.874144
Si	-0.890770	4.414983	-0.093679
O	0.003315	1.408445	4.838340
O	0.007504	-1.199732	4.898165
O	0.009572	-3.483011	3.638265
O	0.007837	-4.835093	1.408032
O	0.002221	-4.894164	-1.199562
O	0.001119	-3.637546	-3.484967
O	-0.007016	-1.408566	-4.838649
O	-0.007599	1.198871	-4.898425
O	-0.006899	3.482622	-3.638325
O	-0.007019	4.834853	-1.408787
O	-0.005046	4.895681	1.199382
O	0.002476	3.637140	3.484211
Si	0.890316	0.095625	4.418179
Si	0.892966	-3.773053	2.288365
Si	0.887563	-3.872237	-2.126362
Si	0.879453	-0.094489	-4.420960
Si	0.879427	3.775186	-2.290859
Si	0.884698	3.875090	2.123531
Si	2.850353	0.069169	2.979174
Si	2.852763	-2.543377	1.541649
Si	2.849195	-2.610758	-1.438371

Atom	x	y	z
Si	2.843207	-0.061992	-2.986787
Si	2.844055	2.550223	-1.549027
Si	2.847391	2.618228	1.430850
O	3.534316	1.383568	2.269233
O	3.537659	-1.270991	2.323068
O	3.538625	-2.648323	0.052370
O	3.531797	-1.374235	-2.277574
O	3.529706	1.279940	-2.333286
O	3.533522	2.657192	-0.061457
O	-1.213021	1.448134	2.395109
O	-1.210563	-1.345540	2.460191
O	-1.210904	-2.798653	0.062135
O	-1.215742	-1.452320	-2.391351
O	-1.218230	1.342388	-2.456353
O	-1.215871	2.796263	-0.058104
N	-2.593413	2.438694	4.025815
N	-2.589206	-2.269098	4.130627
N	-2.591862	-4.705222	0.105008
N	-2.598933	-2.444395	-4.018758
N	-2.603454	2.261902	-4.123531
N	-2.601968	4.699190	-0.097412
O	1.216193	0.061243	2.799542
O	1.218592	-2.389377	1.447650
O	1.215318	-2.453784	-1.346961
O	1.209559	-0.058000	-2.803195
O	1.210595	2.392469	-1.450582
O	1.213672	2.457520	1.343063
N	2.601425	0.104371	4.702961
N	2.604011	-4.017314	2.435753
N	2.598462	-4.123256	-2.265658
N	2.590064	-0.099645	-4.710016
N	2.589657	4.023490	-2.442464
N	2.595219	4.130062	2.258767
H	-3.192385	-2.864127	-4.720264
H	-3.198073	2.654038	-4.840114
H	-3.186557	2.860246	4.726618
H	-3.181827	-2.661893	4.848305
H	-3.197342	5.515169	-0.112238
H	-3.185341	-5.522537	0.121378
H	3.198882	-4.715325	2.859311
H	3.196164	0.122703	5.519427

Appendix B. Structure of theoretically discovered $\{\mathbf{Si(NH)_{0.5}O_{1.5}}\}_n$ Cages

Atom	x	y	z
H	3.183347	-0.119537	-5.527365
H	3.192567	-4.838992	-2.659680
H	3.188288	4.848684	2.649201
H	3.182645	4.720547	-2.870279

Bibliography

[1] M. Born and R. Oppenheimer, "Zur quantentheorie der molekeln", Annalen der Physik **389**, 457 (1927).

[2] P. Hohenberg and W. Kohn, "Phys rev 136: b864", Kohn W, Sham LJ (1965) Phys Rev **140**, A1133 (1964).

[3] W. Kohn and L. J. Sham, "Self-consistent equations including exchange and correlation effects", Physical review **140**, A1133 (1965).

[4] J. P. Perdew, K. Schmidt, V. Van Doren, C. Van Alsenoy, and P. Geerlings, "Jacob's ladder of density functional approximations for the exchange-correlation energy", in Aip conference proceedings, Vol. 577 (AIP, 2001), pp. 1–20.

[5] C. Li, X. Zheng, A. J. Cohen, P. Mori-Sánchez, and W. Yang, "Local scaling correction for reducing delocalization error in density functional approximations", Phys. Rev. Lett. **114**, 053001 (2015).

[6] J. Sun, A. Ruzsinszky, and J. P. Perdew, "Strongly constrained and appropriately normed semilocal density functional", Phys. Rev. Lett. **115**, 036402 (2015).

[7] N. Q. Su and X. Xu, "Toward the construction of parameter-free doubly hybrid density functionals", International Journal of Quantum Chemistry **115**, 589 (2015).

[8] J. C. Slater, "A simplification of the hartree-fock method", Physical Review **81**, 385 (1951).

[9] S. H. Vosko, L. Wilk, and M. Nusair, "Accurate spin-dependent electron liquid correlation energies for local spin density calculations: a critical analysis", Canadian Journal of physics **58**, 1200 (1980).

[10] J. P. Perdew, K. Burke, and M. Ernzerhof, "Generalized gradient approximation made simple", Physical review letters **77**, 3865 (1996).

[11] A. D. Becke, "Density-functional exchange-energy approximation with correct asymptotic behavior", Physical review A **38**, 3098 (1988).

[12] C. Lee, W. Yang, and R. G. Parr, "Development of the colle-salvetti correlation-energy formula into a functional of the electron density", Physical review B **37**, 785 (1988).

[13] J. Tao, J. P. Perdew, V. N. Staroverov, and G. E. Scuseria, "Climbing the density functional ladder: nonempirical meta–generalized gradient approximation designed for molecules and solids", Physical Review Letters **91**, 146401 (2003).

[14] C. Adamo and V. Barone, "Toward reliable density functional methods without adjustable parameters: the pbe0 model", The Journal of chemical physics **110**, 6158 (1999).

[15] A. D. Becke, "Density-functional thermochemistry. iii. the role of exact exchange", The Journal of chemical physics **98**, 5648 (1993).

[16] P. Stephens, F. Devlin, C. Chabalowski, and M. J. Frisch, "Ab initio calculation of vibrational absorption and circular dichroism spectra using density functional force fields", The Journal of Physical Chemistry **98**, 11623 (1994).

[17] C. G. Broyden, "A class of methods for solving nonlinear simultaneous equations", Mathematics of computation **19**, 577 (1965).

[18] P. Pulay, "Convergence acceleration of iterative sequences. the case of scf iteration", Chemical Physics Letters **73**, 393 (1980).

[19] U. von Barth and L. Hedin, "A local exchange-correlation potential for the spin polarized case. i", Journal of Physics C: Solid State Physics **5**, 1629 (1972).

[20] *NIST Computational Chemistry Comparison and Benchmark Database, NIST Standard Reference Database Number 101, Editor: Russell D. Johnson III*, See http://cccbdb.nist.gov/, 2015.

[21] B. K. Alpert, G. Beylkin, D. Gines, and L. Vozovoi, "Adaptive Solution of Partial Differential Equations in Multiwavelet Bases", J. Comput. Phys. **182**, 149 (2002).

[22] B. K. Alpert, "A Class of Bases in L^2 for the Sparse Representation of Integral Operators", SIAM J. Math. Analysis **24**, 246 (1999).

[23] J. White and D. Bird, "Implementation of gradient-corrected exchange-correlation potentials in car-parrinello total-energy calculations", Physical Review B **50**, 4954 (1994).

[24] M. A. Marques, M. J. Oliveira, and T. Burnus, "Libxc: a library of exchange and correlation functionals for density functional theory", Computer Physics Communications **183**, 2272 (2012).

[25] A. Bergner, M. Dolg, W. Küchle, H. Stoll, and H. Preuß, "Ab initio energy-adjusted pseudopotentials for elements of groups 13–17", Molecular Physics **80**, 1431 (1993).

[26] W. J. Stevens, H. Basch, and M. Krauss, "Compact effective potentials and efficient shared-exponent basis sets for the first-and second-row atoms", The Journal of chemical physics **81**, 6026 (1984).

[27] P. J. Hay and W. R. Wadt, "Ab initio effective core potentials for molecular calculations. potentials for k to au including the outermost core orbitals", The Journal of Chemical Physics **82**, 299 (1985).

[28] M. Dolg and X. Cao, "Relativistic pseudopotentials: their development and scope of applications", Chemical reviews **112**, 403 (2011).

[29] C. Herring, "A new method for calculating wave functions in crystals", Physical Review **57**, 1169 (1940).

[30] J. C. Phillips and L. Kleinman, "New method for calculating wave functions in crystals and molecules", Physical Review **116**, 287 (1959).

[31] W. C. Topp and J. J. Hopfield, "Chemically motivated pseudopotential for sodium", Physical Review B **7**, 1295 (1973).

[32] G. Bachelet, D. Hamann, and M. Schlüter, "Pseudopotentials that work: from h to pu", Physical Review B **26**, 4199 (1982).

[33] L. Kleinman and D. Bylander, "Efficacious form for model pseudopotentials", Physical Review Letters **48**, 1425 (1982).

[34] A. Willand, Y. O. Kvashnin, L. Genovese, Á. Vázquez-Mayagoitia, A. K. Deb, A. Sadeghi, T. Deutsch, and S. Goedecker, "Norm-conserving pseudopotentials with chemical accuracy compared to all-electron calculations", The Journal of chemical physics **138**, 104109 (2013).

[35] A. Zunger, "Spin-dependent correlated atomic pseudopotentials", Physical Review B **22**, 649 (1980).

[36] S. Watson and E. Carter, "Spin-dependent pseudopotentials", Physical Review B **58**, R13309 (1998).

[37] S. G. Louie, S. Froyen, and M. L. Cohen, "Nonlinear ionic pseudopotentials in spin-density-functional calculations", Physical Review B **26**, 1738 (1982).

[38] G. B. Bachelet and M. Schlüter, "Relativistic norm-conserving pseudopotentials", Physical Review B **25**, 2103 (1982).

[39] D. Vanderbilt, "Soft self-consistent pseudopotentials in a generalized eigenvalue formalism", Physical Review B **41**, 7892 (1990).

[40] P. E. Blöchl, "Projector augmented-wave method", Physical review B **50**, 17953 (1994).

[41] G. Kresse and D. Joubert, "From ultrasoft pseudopotentials to the projector augmented-wave method", Physical Review B **59**, 1758 (1999).

[42] S. Goedecker, M. Teter, and J. Hutter, "Separable dual-space gaussian pseudopotentials", Physical Review B **54**, 1703 (1996).

[43] C. Hartwigsen, S. Gœdecker, and J. Hutter, "Relativistic separable dual-space gaussian pseudopotentials from h to rn", Physical Review B **58**, 3641 (1998).

[44] J. A. Nelder and R. Mead, "A simplex method for function minimization", The computer journal **7**, 308 (1965).

[45] M. Krack, "Pseudopotentials for h to kr optimized for gradient-corrected exchange-correlation functionals", Theoretical Chemistry Accounts: Theory, Computation, and Modeling (Theoretica Chimica Acta) **114**, 145 (2005).

[46] K. Lejaeghere, V. Van Speybroeck, G. Van Oost, and S. Cottenier, "Error estimates for solid-state density-functional theory predictions: an overview by means of the ground-state elemental crystals", Critical Reviews in Solid State and Materials Sciences **39**, 1 (2014).

[47] B. N. Papas and H. F. Schaefer, "Concerning the precision of standard density functional programs: gaussian, molpro, nwchem, q-chem and gamess", J. Mol. Struct.: THEOCHEM **768**, 175 (2006).

[48] J. Paier, R. Hirschl, M. Marsman, and G. Kresse, "The perdew–burke–ernzerhof exchange-correlation functional applied to the g2-1 test set using a plane-wave basis set", J. Chem. Phys. **122**, 234102 (2005).

[49] R. Peverati and D. G. Truhlar, "Quest for a universal density functional: the accuracy of density functionals across a broad spectrum of databases in chemistry and physics", Philos. Trans. R. Soc. London A: Math., Phys. and Eng. Sci. **372**, 20120476 (2014).

[50] D. Moncrieff and S. Wilson, "Computational linear dependence in molecular electronic structure calculations using universal basis sets", International journal of quantum chemistry **101**, 363 (2005).

[51] B. Delley, "An all-electron numerical method for solving the local density functional for polyatomic molecules", J. Chem. Phys. **92**, 508 (1990).

[52] R. J. Harrison, G. I. Fann, T. Yanai, and G. Beylkin, "Multiresolution quantum chemistry in multiwavelet bases", in International conference on computational science (Springer, 2003), pp. 103–110.

[53] R. J. Harrison, G. I. Fann, T. Yanai, Z. Gan, and G. Beylkin, "Multiresolution quantum chemistry: basic theory and initial applications", The Journal of chemical physics **121**, 11587 (2004).

[54] T. Yanai, G. I. Fann, Z. Gan, R. J. Harrison, and G. Beylkin, "Multiresolution quantum chemistry in multiwavelet bases: hartree–fock exchange", The Journal of chemical physics **121**, 6680 (2004).

[55] T. Yanai, G. I. Fann, Z. Gan, R. J. Harrison, and G. Beylkin, "Multiresolution quantum chemistry in multiwavelet bases: analytic derivatives for hartree–fock and density functional theory", The Journal of chemical physics **121**, 2866 (2004).

[56] L. A. Curtiss, K. Raghavachari, P. C. Redfern, and J. A. Pople, "Assessment of gaussian-2 and density functional theories for the computation of enthalpies of formation", J. Chem. Phys. **106**, 1063 (1997).

[57] H. L. Schmider and A. D. Becke, "Optimized density functionals from the extended g2 test set", J. Chem. Phys. **108**, 9624 (1998).

[58] S. R. Jensen, S. Saha, J. A. Flores-Livas, W. Huhn, V. Blum, S. Goedecker, and L. Frediani, *Gga-pbe and hybrid-pbe0 energies and dipole moments with mrchem, fhi-aims, nwchem and elk*, 2017.

[59] S. Kotochigova, Z. H. Levine, E. L. Shirley, M. D. Stiles, and C. W. Clark, *Atomic reference data for electronic structure calculations* (National Institute of Standards and Technology, Physics Laboratory, 1997).

[60] D. Feller, "The role of databases in support of computational chemistry calculations", J. Comput. Chem. **17**, 1571 (1996).

[61] K. L. Schuchardt, B. T. Didier, T. Elsethagen, L. Sun, V. Gurumoorthi, J. Chase, J. Li, and T. L. Windus, "Basis set exchange: a community database for computational sciences", J. Chem. Information and Modeling **47**, 1045 (2007).

[62] D. J. Singh and L. Nordstrom, *Planewaves, pseudopotentials, and the lapw method* (Springer Science & Business Media, 2006).

[63] M. Valiev, E. Bylaska, N. Govind, K. Kowalski, T. Straatsma, H. van Dam, D. Wang, J. Nieplocha, E. Apra, T. Windus, and W. de Jong, "NWChem: A Comprehensive and Scalable Open-source Solution for Large Scale Molecular Simulations", Comput. Phys. Comm. **181**, 1477 (2010).

[64] V. Blum, R. Gehrke, F. Hanke, P. Havu, V. Havu, X. Ren, K. Reuter, and M. Scheffler, "Ab initio Molecular Simulations with Numeric Atom-centered Orbitals", Comput. Phys. Comm. **180**, 2175 (2009).

[65] *Multiresolution chemistry (mrchem) program package*. See http://mrchemdoc.readthedocs.org/en/latest 2016.

[66] *An all-electron full-potential linearised augmented-plane wave (fp-lapw) code*. See http://http://elk.sourceforge.net/, 2015.

[67] U. Ekström, L. Visscher, R. Bast, A. J. Thorvaldsen, and K. Ruud, "Arbitrary-order density functional response theory from automatic differentiation", Journal of chemical theory and computation **6**, 1971 (2010).

[68] S. H. Vosko, L. Wilk, and M. Nusair, "Accurate Spin-Dependent Electron Liquid Correlation Energies for Local Spin Density Calculations: A Critical Analysis", Can. J. Phys. **58**, 1200 (1980).

[69] M. G. Medvedev, I. S. Bushmarinov, J. Sun, J. P. Perdew, and K. A. Lyssenko, "Density functional theory is straying from the path toward the exact functional", Science **355**, 49 (2017).

[70] K. L. Bak, J. Gauss, T. Helgaker, P. Jørgensen, and J. Olsen, "The accuracy of molecular dipole moments in standard electronic structure calculations", Chem. Phys. Lett. **319**, 563 (2000).

[71] P. Blaha, K. Schwarz, G. Madsen, D. Kvasnicka, and J. Luitz, "Wien2k", An augmented plane wave+ local orbitals program for calculating crystal properties (2001).

[72] L. Genovese, A. Neelov, S. Goedecker, T. Deutsch, S. A. Ghasemi, A. Willand, D. Caliste, O. Zilberberg, M. Rayson, A. Bergman, et al., "Daubechies wavelets as a basis set for density functional pseudopotential calculations", The Journal of chemical physics **129**, 014109 (2008).

[73] P. Giannozzi, S. Baroni, N. Bonini, M. Calandra, R. Car, C. Cavazzoni, D. Ceresoli, G. L. Chiarotti, M. Cococcioni, I. Dabo, et al., "Quantum espresso: a modular and open-source software project for quantum simulations of materials", Journal of physics: Condensed matter **21**, 395502 (2009).

[74] K. Lejaeghere, G. Bihlmayer, T. Björkman, P. Blaha, S. Blügel, V. Blum, D. Caliste, I. E. Castelli, S. J. Clark, A. Dal Corso, et al., "Reproducibility in density functional theory calculations of solids", Science **351**, aad3000 (2016).

[75] S. Goedecker, "Minima hopping: an efficient search method for the global minimum of the potential energy surface of complex molecular systems", The Journal of chemical physics **120**, 9911 (2004).

[76] S. Goedecker, W. Hellmann, and T. Lenosky, "Global minimum determination of the born-oppenheimer surface within density functional theory", Physical review letters **95**, 055501 (2005).

[77] S. Roy, S. Goedecker, and V. Hellmann, "Bell-evans-polanyi principle for molecular dynamics trajectories and its implications for global optimization", Physical Review E **77**, 056707 (2008).

[78] S. E. Schönborn, S. Goedecker, S. Roy, and A. R. Oganov, "The performance of minima hopping and evolutionary algorithms for cluster structure prediction", The Journal of chemical physics **130**, 144108 (2009).

[79] B. Schaefer, S. A. Ghasemi, S. Roy, and S. Goedecker, "Stabilized quasi-newton optimization of noisy potential energy surfaces", The Journal of chemical physics **142**, 034112 (2015).

[80] V. Tozzini, F. Buda, and A. Fasolino, "Spontaneous formation and stability of small gap fullerenes", physical review letters **85**, 4554 (2000).

[81] H.-S. Wu, X.-Y. Cui, X.-F. Qin, D. L. Strout, and H. Jiao, "Boron nitride cages from b12n12 to b36n36: square–hexagon alternants vs boron nitride tubes", Journal of molecular modeling **12**, 537 (2006).

[82] S. Bromley, "Thermodynamic stability of discrete fully coordinated sio2 spherical and elongated nanocages", Nano Letters **4**, 1427 (2004).

[83] S. Mohr, P. Pochet, M. Amsler, B. Schaefer, A. Sadeghi, L. Genovese, and S. Goedecker, "Boron aggregation in the ground states of boron-carbon fullerenes", Physical Review B **89**, 041404 (2014).

[84] P. Ayala, R. Arenal, M. Rümmeli, A. Rubio, and T. Pichler, "The doping of carbon nanotubes with nitrogen and their potential applications", Carbon **48**, 575 (2010).

[85] Y. Chai, T. Guo, C. Jin, R. E. Haufler, L. F. Chibante, J. Fure, L. Wang, J. M. Alford, and R. h. E. Smalley, "Fullerenes with metals inside", The Journal of Physical Chemistry **95**, 7564 (1991).

[86] H.-J. Muhr, R. Nesper, B. Schnyder, and R. Kötz, "The boron heterofullerenes c 59 b and c 69 b: generation, extraction, mass spectrometric and xps characterization", Chemical physics letters **249**, 399 (1996).

[87] J. Averdung, H. Luftmann, I. Schlachter, and J. Mattay, "Aza-dihydro [60] fullerene in the gas phase. a mass-spectrometric and quantumchemical study", Tetrahedron **51**, 6977 (1995).

[88] I. Lamparth, B. Nuber, G. Schick, A. Skiebe, T. Grösser, and A. Hirsch, "C59n+ and c69n+: isoelectronic heteroanalogues of c60 and c70", Angewandte Chemie International Edition in English **34**, 2257 (1995).

[89] J. F. Christian, Z. Wan, and S. L. Anderson, "O++ c60ů c60o+ production and decomposition, charge transfer, and formation of c59o+. dopeyball or [co@ c58+", Chemical physics letters **199**, 373 (1992).

[90] T. Ohtsuki, K. Ohno, K. Shiga, Y. Kawazoe, Y. Maruyama, and K. Masumoto, "Formation of as-and ge-doped heterofullerenes", Physical Review B **60**, 1531 (1999).

[91] M. Pellarin, C. Ray, J. Lermé, J. Vialle, M. Broyer, X. Blase, P. Kéghélian, P. Mélinon, A. Perez, et al., "Photolysis experiments on sic mixed clusters: from silicon carbide clusters to silicon-doped fullerenes", Journal of Chemical Physics **110** (1999).

[92] N. Xin, H. Huang, J. Zhang, Z. Dai, and L. Gan, "Fullerene doping: preparation of aza-fullerene c59nh and oxafulleroids c59o3 and c60o4", Angewandte Chemie International Edition **51**, 6163 (2012).

[93] U. Zimmermann, N. Malinowski, A. Burkhardt, and T. Martin, "Metal-coated fullerenes", Carbon **33**, 995 (1995).

[94] R. Tenne and M. Redlich, "Recent progress in the research of inorganic fullerene-like nanoparticles and inorganic nanotubes", Chemical Society Reviews **39**, 1423 (2010).

[95] A. Willand, M. Gramzow, S. A. Ghasemi, L. Genovese, T. Deutsch, K. Reuter, and S. Goedecker, "Structural metastability of endohedral silicon fullerenes", Physical Review B **81**, 201405 (2010).

[96] N. G. Szwacki, A. Sadrzadeh, and B. I. Yakobson, "B 80 fullerene: an ab initio prediction of geometry, stability, and electronic structure", Physical review letters **98**, 166804 (2007).

[97] S. De, A. Willand, M. Amsler, P. Pochet, L. Genovese, and S. Goedecker, "Energy landscape of fullerene materials: a comparison of boron to boron nitride and carbon", Physical review letters **106**, 225502 (2011).

[98] J. Zhao, L. Wang, F. Li, and Z. Chen, "B80 and other medium-sized boron clusters: core- shell structures, not hollow cages", The Journal of Physical Chemistry A **114**, 9969 (2010).

[99] Y.-J. Wang, Y.-F. Zhao, W.-L. Li, T. Jian, Q. Chen, X.-R. You, T. Ou, X.-Y. Zhao, H.-J. Zhai, S.-D. a. Li, et al., "Observation and characterization of the smallest borospherene, b28- and b28", The Journal of chemical physics **144**, 064307 (2016).

[100] J. Zhao, X. Huang, R. Shi, H. Liu, Y. Su, and R. B. King, "B 28: the smallest all-boron cage from an ab initio global search", Nanoscale **7**, 15086 (2015).

[101] J. Lv, Y. Wang, L. Zhu, and Y. Ma, "B38: an all-boron fullerene analogue", Nanoscale **6**, 11692 (2014).

[102] H.-J. Zhai, Y.-F. Zhao, W.-L. Li, Q. Chen, H. Bai, H.-S. Hu, Z. A. Piazza, W.-J. Tian, H.-G. Lu, Y. B. Wu, et al., Nature chemistry **6**, 727 (2014).

[103] P. Boulanger, M. Morinière, L. Genovese, and P. Pochet, "Selecting boron fullerenes by cage-doping mechanisms", The Journal of chemical physics **138**, 184302 (2013).

[104] H. Bai, Q. Chen, H.-J. Zhai, and S.-D. Li, "Endohedral and exohedral metalloborospherenes: m@ b40 (m= ca, sr) and m&b40 (m= be, mg)", Angewandte Chemie International Edition **54**, 941 (2015).

[105] W. Fa, S. Chen, S. Pande, and X. C. Zeng, "Stability of metal-encapsulating boron fullerene b40", The Journal of Physical Chemistry A **119**, 11208 (2015).

[106] P. Jin, Q. Hou, C. Tang, and Z. Chen, "Computational investigation on the endohedral borofullerenes m@ b40 (m= sc, y, la)", Theoretical Chemistry Accounts **134**, 1 (2015).

[107] H. Bai, B. Bai, L. Zhang, W. Huang, Y.-W. Mu, H.-J. Zhai, and S.-D. Li, "Lithium-decorated borospherene b40: a promising hydrogen storage medium", Scientific Reports **6** (2016).

[108] C.-s. Liu, X.-J. Ye, X.-f. Wang, and X. Yan, "Metalized b 40 fullerene as a novel material for storage and optical detection of hydrogen: a first-principles study", RSC Advances (2016).

[109] C. Tang and X. Zhang, "The hydrogen storage capacity of sc atoms decorated porous boron fullerene b 40: a dft study", International Journal of Hydrogen Energy **41**, 16992 (2016).

[110] H. Dong, T. Hou, S.-T. Lee, and Y. Li, "New ti-decorated b40 fullerene as a promising hydrogen storage material", Scientific reports **5** (2015).

[111] A. Sadeghi, S. A. Ghasemi, B. Schaefer, S. Mohr, M. A. Lill, and S. Goedecker, "Metrics for measuring distances in configuration spaces", The Journal of chemical physics **139**, 184118 (2013).

[112] X. Ren, P. Rinke, V. Blum, J. Wieferink, A. Tkatchenko, A. Sanfilippo, K. Reuter, and M. Scheffler, "Resolution-of-identity approach to hartree–fock, hybrid density functionals, rpa, mp2 and gw with numeric atom-centered orbital basis functions", New Journal of Physics **14**, 053020 (2012).

[113] A. Marek, V. Blum, R. Johanni, V. Havu, B. Lang, T. Auckenthaler, A. Heinecke, H.-J. Bungartz, and H. Lederer, "The elpa library: scalable parallel eigenvalue solutions for electronic structure theory and computational science", Journal of Physics: Condensed Matter **26**, 213201 (2014).

[114] V. Havu, V. Blum, P. Havu, and M. Scheffler, "Efficient o (n) integration for all-electron electronic structure calculation using numeric basis functions", Journal of Computational Physics **228**, 8367 (2009).

[115] A. C. Ihrig, J. Wieferink, I. Y. Zhang, M. Ropo, X. Ren, P. Rinke, M. Scheffler, and V. Blum, "Accurate localized resolution of identity approach for linear-scaling hybrid density functionals and for many-body perturbation theory", New Journal of Physics **17**, 093020 (2015).

[116] C. Hsing, C. Wei, N. Drummond, and R. Needs, "Quantum monte carlo studies of covalent and metallic clusters: accuracy of density functional approximations", Physical Review B **79**, 245401 (2009).

[117] H. W. Kroto, J. R. Heath, S. C. O'Brien, R. F. Curl, R. E. Smalley, et al., "C60: buckminsterfullerene", Nature **318**, 162 (1985).

[118] S. Iijima and T. Ichihashi, "Single-shell carbon nanotubes of 1-nm diameter", (1993).

[119] S. Bromley, M. Zwijnenburg, and T. Maschmeyer, "Fully coordinated silica nanoclusters:(s i o 2) n molecular rings", Physical review letters **90**, 035502 (2003).

[120] S. K. Nayak, B. Rao, S. Khanna, and P. Jena, "Atomic and electronic structure of neutral and charged sinom clusters", The Journal of chemical physics **109**, 1245 (1998).

[121] J. K. West, B. F. Zhu, Y. C. Cheng, and L. L. Hench, "Quantum chemistry of sol-gel silica clusters", Journal of Non-Crystalline Solids **121**, 51 (1990).

[122] Z. L. Wang, R. P. Gao, J. L. Gole, and J. D. Stout, "Silica nanotubes and nanofiber arrays", Advanced Materials **12**, 1938 (2000).

[123] H.-P. Lin, C.-Y. Mou, S.-B. Liu, et al., "Formation of mesoporous silica nanotubes", Advanced Materials **12**, 103 (2000).

[124] D. Zhang, J. Wu, R. Zhang, and C. Liu, "A family of stable silica fullerenes with fully coordinated structures", The Journal of Physical Chemistry B **110**, 17757 (2006).

[125] N. Ning, F. Calvo, A. Van Duin, D. Wales, and H. Vach, "Spontaneous self-assembly of silica nanocages into inorganic framework materials", The Journal of Physical Chemistry C **113**, 518 (2008).

[126] A. Fujishima, "Electrochemical photolysis of water at a semiconductor electrode", nature **238**, 37 (1972).

[127] B. O'Regan and M. Grätzel, "A low-cost, high-efficiency solar cell based on dye-sensitized colloidal tio2 films", Nature **353**, 737 (1991).

[128] M. Grätzel, "Photoelectrochemical cells", Nature **414**, 338 (2001).

[129] A. Nozik, "Photoelectrolysis of water using semiconducting tio2 crystals", Nature **257**, 383 (1975).

[130] G. Zhao, H. Kozuka, H. Lin, and T. Yoko, "Sol-gel preparation of ti 1- x v x o 2 solid solution film electrodes with conspicuous photoresponse in the visible region", Thin Solid Films **339**, 123 (1999).

[131] R. Asahi, T. Morikawa, T. Ohwaki, K. Aoki, and Y. Taga, "Visible-light photocatalysis in nitrogen-doped titanium oxides", science **293**, 269 (2001).

[132] W.-J. Yin, S.-H. Wei, M. M. Al-Jassim, and Y. Yan, "Double-hole-mediated coupling of dopants and its impact on band gap engineering in tio 2", Physical review letters **106**, 066801 (2011).

[133] X. Chen and S. S. Mao, "Titanium dioxide nanomaterials: synthesis, properties, modifications, and applications", Chemical reviews **107**, 2891 (2007).

[134] S. M. Gupta and M. Tripathi, "A review of tio2 nanoparticles", Chinese Science Bulletin **56**, 1639 (2011).

[135] M. Niederberger, M. H. Bartl, and G. D. Stucky, "Benzyl alcohol and transition metal chlorides as a versatile reaction system for the nonaqueous and low-temperature synthesis of crystalline nano-objects with controlled dimensionality", Journal of the American Chemical Society **124**, 13642 (2002).

[136] Y. Bessekhouad, D. Robert, and J. V. Weber, "Synthesis of photocatalytic tio 2 nanoparticles: optimization of the preparation conditions", Journal of Photochemistry and Photobiology A: Chemistry **157**, 47 (2003).

[137] A. A. Gribb and J. F. Banfield, "Particle size effects on transformation kinetics and phase stability in nanocrystalline tio2", American Mineralogist **82**, 717 (1997).

[138] A. Barnard and L. Curtiss, "Prediction of tio2 nanoparticle phase and shape transitions controlled by surface chemistry", Nano letters **5**, 1261 (2005).

[139] L. X. Chen, T. Rajh, Z. Wang, and M. C. Thurnauer, "Xafs studies of surface structures of tio2 nanoparticles and photocatalytic reduction of metal ions", The Journal of Physical Chemistry B **101**, 10688 (1997).

[140] H. C. Choi, Y. M. Jung, and S. B. Kim, "Size effects in the raman spectra of tio 2 nanoparticles", Vibrational Spectroscopy **37**, 33 (2005).

[141] T. Rajh, L. Chen, K. Lukas, T. Liu, M. Thurnauer, and D. Tiede, "Surface restructuring of nanoparticles: an efficient route for ligand- metal oxide crosstalk", The Journal of Physical Chemistry B **106**, 10543 (2002).

[142] K. L. Yeung, A. J. Maira, J. Stolz, E. Hung, N. Ka-Chun Ho, A. C. Wei, J. Soria, K.-J. Chao, and P. L. Yue, "Ensemble effects in nanostructured tio2 used in the gas-phase photooxidation of trichloroethylene", The Journal of Physical Chemistry B **106**, 4608 (2002).

[143] S. Hamad, C. Catlow, S. Woodley, S. Lago, and J. Mejias, "Structure and stability of small tio2 nanoparticles", The Journal of Physical Chemistry B **109**, 15741 (2005).

[144] Z.-w. Qu and G.-J. Kroes, "Theoretical study of the electronic structure and stability of titanium dioxide clusters (tio2) n with n= 1- 9", The Journal of Physical Chemistry B **110**, 8998 (2006).

[145] M. Chen and D. A. Dixon, "Tree growth hybrid genetic algorithm for predicting the structure of small (tio2) n, n= 2–13, nanoclusters", Journal of Chemical Theory and Computation **9**, 3189 (2013).

[146] M. Ranade, A. Navrotsky, H. Zhang, J. Banfield, S. Elder, A. Zaban, P. Borse, S. Kulkarni, G. Doran, and H. Whitfield, "Energetics of nanocrystalline tio2", Proceedings of the National Academy of Sciences **99**, 6476 (2002).

[147] X. Chen, L. Liu, Z. Liu, M. A. Marcus, W.-C. Wang, N. A. Oyler, M. E. Grass, B. Mao, P.-A. Glans, Y. Y. Peter, et al., "Properties of disorder-engineered black titanium dioxide nanoparticles through hydrogenation", Scientific reports **3**, 1510 (2013).

[148] X. Chen, L. Liu, Y. Y. Peter, and S. S. Mao, "Increasing solar absorption for photocatalysis with black hydrogenated titanium dioxide nanocrystals", Science **331**, 746 (2011).

[149] H. Zhang and J. F. Banfield, "Structural characteristics and mechanical and thermodynamic properties of nanocrystalline tio2", Chemical reviews **114**, 9613 (2014).

[150] V. Blagojevic, Y.-R. Chen, M. Steigerwald, L. Brus, and R. A. Friesner, "Quantum chemical investigation of cluster models for tio2 nanoparticles with water-derived ligand passivation: studies of excess electron states and implications for charge transport in the gratzel cell", The Journal of Physical Chemistry C **113**, 19806 (2009).

Santanu Saha

Curriculum Vitae

Work address University of Basel
Department of Physics
Klingelbergstrasse 82
CH-4056 Basel
Switzerland

Phone +41 61 267 3910
E-Mail santanu.saha@unibas.ch

Date of birth November 27, 1987
Place of birth Coochbehar, India
Nationality Indian

Education

- **Ph.D. Student (Physics)** — Basel, Switzerland
  University of Basel — *May. 2013 – April. 2017*
  - Generation and benchmarking of pseudopotentials for hybrid functionals

- **M.Sc. Physics** — Kanpur, India
  Indian Institute of Technology,Kanpue — *August. 2010 – May. 2012*
  - Thesis title: Preparation, structural and magnetic studies on doped ferrite multiferroics.

- **B.Sc. Physics** — Kolkata, India
  St. Xaviers College,University of Calcutta — *July, 2007 – July. 2010*

Work Experience

- **Research Associate** — Kanpur, India
  IIT Kanpur — *May. 2012 – March. 2013*
  - Dye Sensitized Hybrid Solar Cells with Up-conversion Nanostructures for enhanced efficiency

Publications

1. *Preparation, structural and magnetic studies on $BiFe_{1-x}Cr_xO_3$ (x= 0.0, 0.05 and 0.1) multiferroic nanoparticles*
   Samar Layek, **Santanu Saha**, HC Verma
   AIP Advances 3 (3), 032140 (2013)

2. *Interatomic potentials for ionic systems with density functional accuracy based on charge densities obtained by a neural network*
   S Alireza Ghasemi, Albert Hofstetter, **Santanu Saha**, Stefan Goedecker
   Phys. Rev. B 92 (4), 045131 (2015)

3. *Characterization of individual molecular adsorption geometries by atomic force microscopy: Cu-TCPP on rutile TiO2 (110)*
   Res Jöhr, Antoine Hinaut, Rémy Pawlak, Ali Sadei, **Santanu Saha**, Stefan Goedecker, Bartosz Such, Marek Szymonski, Ernst Meyer, Thilo Glatzel
   J. Chem. Phys. 143 (9), 094202 (2015)

4. *Reproducibility in density functional theory calculations of solids*
   Kurt Lejaeghere, Gustav Bihlmayer, Torbjörn Björkman, Peter Blaha, Stefan Blügel, Volker Blum, Damien Caliste, Ivano E Castelli, Stewart J Clark, Andrea Dal Corso, Stefano de Gironcoli, Thierry Deutsch, John Kay Dewhurst, Igor Di Marco, Claudia Draxl, Marcin Dulak, Olle Eriksson, José A Flores-Livas, Kevin F Garrity, Luigi Genovese, Paolo Giannozzi, Matteo Giantomassi, Stefan Goedecker, Xavier Gonze, Oscar Granäs, EKU Gross, Andris Gulans, Francois Gygi, DR Hamann, Phil J Hasnip, NAW Holzwarth, Diana Iusan, Dominik B Jochym, Francois Jollet, Daniel Jones, Georg Kresse, Klaus Koepernik, Emine Kücükbenli, Yaroslav O Kvashnin, Inka LM Locht, Sven Lubeck, Martijn Marsman, Nicola Marzari, Ulrike Nitzsche, Lars Nordström, Taisuke Ozaki, Lorenzo Paulatto, Chris J Pickard, Ward Poelmans, Matt IJ Probert, Keith Refson, Manuel Richter, Gian-Marco Rignanese, **Santanu Saha**, Matthias Scheffler, Martin Schlipf, Karlheinz Schwarz, Sangeeta Sharma, Francesca Tavazza, Patrik Thunström, Alexandre Tkatchenko, Marc Torrent, David Vanderbilt, Michiel J van Setten, Veronique Van Speybroeck, John M Wills, Jonathan R Yates, Guo-Xu Zhang, Stefaan Cottenier
   Science 351 (6280), aad3000 (2016)

5. *Structure and optical properties of small $(TiO_2)_n$ nanoparticles, n=21-24.*
   Richard Baochang Wang, Sabine korbel, **Santanu Saha**, Silvana Botti, Natalia Skorodumova
   (Submitted to J. Chem. Phys. under review)

6. *Metastable exohedrally decorated borospherene B_{40}*
   Santanu Saha, Luigi Genovese, Stefan Goedecker
   (Submitted to Scientifc Reports, under review)

7. *Eliminating core electrons: Pseudopotentials and PAW Potentials*
   Stefan Goedecker and **Santanu Saha**

to appear as Book Chapter in Vol 5, Handbook of Solid State Chemistry

8. *GGA-PBE and hybrid-PBE0 energies and dipole moments with MRChem, FHI-aims, NWChem and ELK*
Stig Rune Jensen, **Santanu Saha**, José A Flores-Livas, William Huhn, Volker Blum, Stefan Goedecker, Luca Frediani
Uit Open Research Dataverse,V1 doi:10.18710/0EM0EL

9. *The Elephant in the Room of Density Functional Theory Calculations*
Stig Rune Jensen, **Santanu Saha**, José A Flores-Livas, William Huhn, Volker Blum, Stefan Goedecker, Luca Frediani
(Submitted to J. Phy. Chem. Lett. under review) arXiv:1702.00957

10. *Theoretical discovery of* $\{Si(NH)_{0.5}O_{1.5}\}_n$ *(n=20,24) cages* (in preparation)

11. *Pseudopotentials for hybrid functionals* (in preparation)

Presentations

- **Soft and accurate norm conserving pseudopotentials**
  PASC (Poster) – Lausanne, Switzerland *April. 2016*
  Total Energy and Force Methods 2016 (Poster) – Luxembourg,Luxembourg *Jan. 2016*
  Psi-K Conference (Poster) – San Sebastian, Spain *Sep. 2015*

Teaching Experience

- **Computational Physics** University of Basel
  - Tutorial Assistant
  - Graded Assignments
- **Statistical Mechanics for Nanosciences** University of Basel
  - Tutorial Assistant
  - Graded Assignments and exam sheets